Polycrystalline Silicon Thin Films for Photovoltaics

Thesis by

Claudine M. Chen

In Partial Fulfillment of the Requirements

for the Degree of

Doctor of Philosophy

California Institute of Technology

Pasadena, California

2001

(submitted June 1, 2001)

Acknowledgments

There are many people during my 6 years at Caltech that have contributed to my experience here, both academically and socially.

I thank Harry Atwater, my advisor, for taking me into his group and for his guidance and encouragement. I admire his enthusiasm and breadth of knowledge, and appreciate his ability to see the positive aspects in any experimental result.

Funding was provided by the United States Department of Energy, Office of Basic Energy Sciences, Lawrence Livermore National Laboratory, and the National Renewable Energy Laboratory. X-ray fluorescence microprobe was performed at the Advanced Light Source at Lawrence Berkeley Laboratories, with help from Scott McHugo and Al Thompson. The positron annihilation spectroscopy was performed in the laboratory of Kelvin Lynn at Washington State University; special thanks to Stefano Rassiga, Mihail Petkov, and Marc Weber. The work on the patterned silicon islands was in collaboration with Hiroshi Tanabe and Rosaria Puglisi, and the work on patterned germanium was in collaboration with Hiroshi Tanabe, and the work on the tin on silicon was in collaboration with Satoshi Okada.

Carol Garland has offered priceless wisdom concerning TEM sample preparation and TEM operation. Her efficient management of the TEM facility

and her courage in life has been inspirational. Thanks to Rosalie Rowe for her efficiency in travel reimbursements, conference arrangements, purchase orders, and everything else that she does that is behind the scenes.

All past and present group members have been a great source of knowledge and friendship. I am lucky to have been part of such a nurturing group. I thank all elder group members, especially Jimmy Yang, Maggie Taylor, and Kyu Min, for their time spent teaching us little ones how to use equipment and make TEM samples. Special thanks to Joseph Christopherson, Geri Nogaki, John Hartman, Mark Brongersma, Elizabeth Boer, Regina Ragan, Maribeth Swiatek, Jason Holt, Rhett Brewer, Julie Casperson, Jimmy Zahler, Aditi Risbud, and Pieter Kik.

In addition, thanks to all my friends at Caltech for making my time here so enjoyable. I particularly thank for the special times, Jim Kempf, Xenia Amashukeli, Demir Coker, Penny Kneebone, Chuck Witham, Gordon Squires, Catherine Baker, Tina Pavlin, Marco Casari, Ravinder Bhatia, Jennie Stephens, Deanna Zubris, Lila Guterman, Claude Seywert, Adrian Hightower, Stephen Glade, and Sven Bossuyt.

My life was also enriched by old friends. Escapes to San Francisco to visit Jennifer Whangbo kept me sane. Thanks to Darcee Killpack, for her care and understanding through my times of crisis.

And finally, thanks to my parents for their support and love. Mom has kept my head high through so many difficult situations.

Abstract

Selective nucleation and solid phase epitaxy offers a low temperature method to fabricate large grain, polycrystalline silicon on foreign substrates. Undoped and highly doped silicon films were nucleated with nickel or indium and annealed at 600 °C. Indium nucleated crystallization proceeded by conventional solid phase epitaxy. Undoped silicon had grain sizes of 1-2 μm. With doping, although there was enhancement of the growth rate, the grain size did not increase, since the incubation time correspondingly decreased. The exception was the phosphorus-doped silicon that had a maximum grain size of 10 μm.

In nickel-nucleated samples, the amorphous silicon layer fully crystallized before the onset of random nucleation, achieving grain sizes on order of tens of microns. Within each grain, however, were many low angle, sub-grain boundaries that came from the needle-like crystal growth. Epitaxy on these layers resulted in strained columnar crystals with dislocations.

Positron annihilation spectroscopy (PAS) was used to study vacancies in solid phase crystallized silicon in four doping cases: undoped, B-doped, P-doped, and P&B-doped. Oxygen-vacancy complexes were seen in all samples and phosphorus-vacancy complexes in the P- and P&B-doped samples. Progressive etchback of a subset of the samples was achieved, and a defect concentration on order of 10^{15} cm^{-3} was estimated for all samples.

List of Figures and Tables

Table of Contents

Chapter 1 Introduction

1.1 Why photovoltaics?

There are many benefits of energy alternatives to fossil fuels, especially now with increasing CO_2 levels and poor air quality resulting from fossil fuel combustion, particularly in developing countries. One alternative is photovoltaics (or solar cells), devices that convert solar radiation to electricity. Besides their appeal as a zero emissions power source, photovoltaics are modular, which make them an ideal source of energy for rural areas that are too difficult to access by a power grid, or do not have the population density to warrant power lines. In developed areas with grid power, however, photovoltaics must compete very strongly with inexpensive fuel sources to be commercially viable, balancing cost of manufacture with power conversion.

1.2 What is a photovoltaic?

Photovoltaics are conceptually very simple devices. Light incident on the device is absorbed and the energy excites electrons to the conduction band, creating electron-hole pairs. The carriers would diffuse through the device until they recombine in the semiconductor bulk, but with a charge separation

structure like a p-n junction or Schottky barrier, a current is collected. Current collection in a solar cell is limited by the rate of carrier recombination, which in turn depends on the minority carrier population. The minority carriers must diffuse to the depletion region where they are swept by the internal field to the other side, at which point they become majority carriers. Since electron mobility is larger than hole mobility, solar cells are often designed such that the majority of carriers are created in a p-type layer, where the minority carriers are electrons. A typical structure is a thin n^+-type layer on top of a p-type layer. For an introduction to the device physics of photovoltaics, see Appendix A.

1.3 Material considerations

The objective of a photovoltaic device is to yield the most power for a given illumination. The solar spectrum is that of a blackbody at 6000 K with some strong absorption peaks for water and CO_2 (see Figure 1.1(a)). A larger band gap material provides a higher voltage than a smaller band gap material, but converts fewer of the incident photons resulting in a lower current. A smaller band gap material absorbs most of the radiation but converts much of it to heat. Considering just the solar spectrum and band gap energy, the best efficiency is found with band gaps of 1-2 eV [1] (see Figure 1.1(b)).

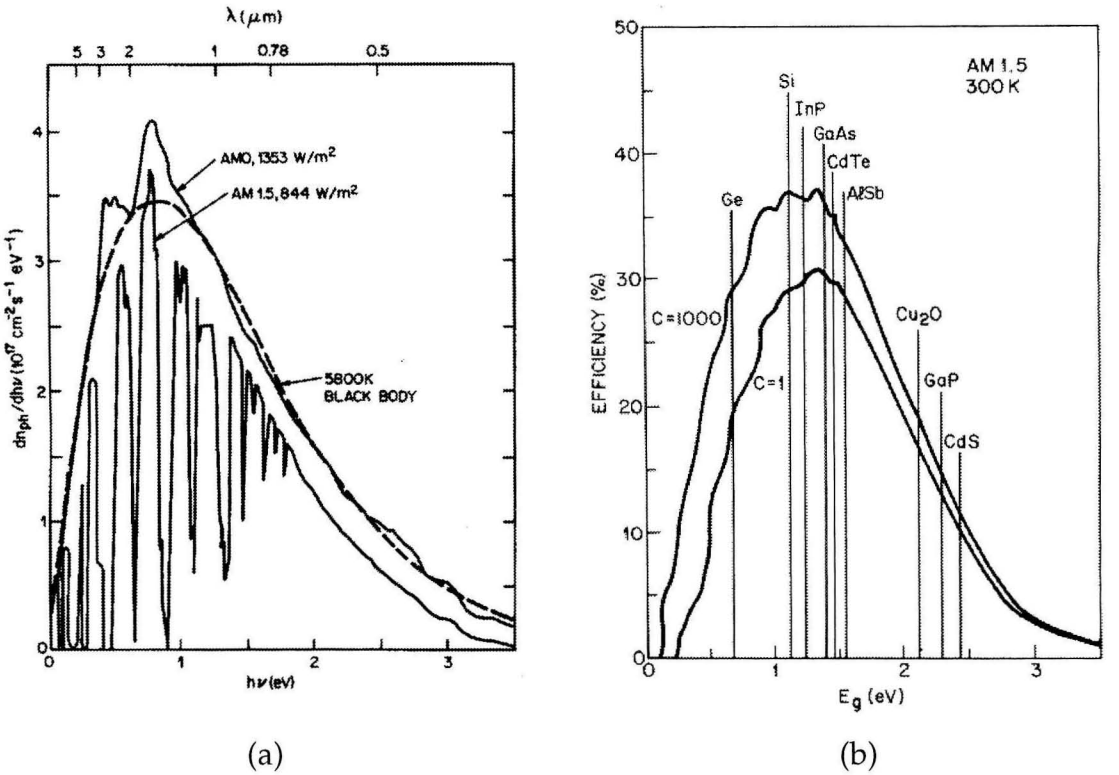

Figure 1.1. (a) Energy spectrum of solar radiation, with large absorption peaks from mainly water and CO_2 in the atmosphere. (b) Cell efficiency as a function of band gap energy, assuming no losses. The band gap of many common semiconductors are labeled. [1]

Both indirect and direct bandgap materials have been explored for application in solar cells, including silicon (monocrystalline, polycrystalline, microcrystalline, and amorphous), and the compound semiconductors GaAs, InP, CdTe, and CIS (copper indium diselenide). Obviously, direct bandgap materials have higher conversion, but silicon is more abundant than the compound semiconductors listed above and has a well established technology and infrastructure for processing, present from the integrated circuit industry.

Amorphous silicon solar cells suffer from the Stabler-Wronski effect [2], a degradation of the efficiency from the creation of dangling bonds under illumination, which puts a cap on the maximum efficiency that can be achieved at ~12%. So, instead, we turn to crystalline silicon. Crystalline silicon has achieved high efficiencies (>20%) in monocrystalline cells made with high quality material and processing techniques, but there is potential for such high efficiencies with less expensive fabrication methods.

1.4 Crystalline silicon technology

Monocrystalline Si cells made from c-Si wafers with state of the art device geometries, have attained efficiencies of 24.7% [3], but also at a high price of fabrication. To reach these world record efficiencies, high quality float zone wafers are processed through many steps, including photolithography and high temperature dopant diffusion, and are passivated with high quality thermally grown oxides [4]. In addition, other measures are needed to improve the efficiency, such as light trapping, back surface fields, and anti-reflection coatings.

Front surface texturing, also known as geometric light trapping, deflects light to angles greater than the critical angle for total internal reflection, which lengthens the light path in the material. It also improves absorption without adding thickness and material costs. Back surface fields, formed by a p+ layer on the backside of a n+/p cell, help drive electrons away from recombination at the

back metal contact/Si interface, as well as improving the contact resistance. Antireflection coatings increase the flux of light that enters into the device.

Approximately one third of the total cost of a crystalline Si solar cell is raw material including the c-Si wafer for mechanical support, one third from processing costs, and another third from assembling the cells into a module. By adopting a monolithic process that uses low cost substrates, material and module assembly costs could be cut drastically. The drive for high cell efficiency at lower cost has stimulated research into thin-film silicon technology coupled with low-cost substrates, such as soda-lime or borosilicate glass. The low thermal stability (<650 °C) of these glasses has motivated low temperature approaches for making crystalline Si thin films. This temperature requirement is likely to exclude crystallization techniques based on melting and solidification, such as zone-melting recrystallization. Innovative designs for thin film silicon photovoltaic cells on glass have been proposed with projected efficiencies of 10% [5] and 15% [6], and a cell fabricated by low temperature solid-phase crystallization on a metal substrate has been made that exhibits an efficiency of 9.2% [7].

The optimization processing done for monocrystalline cells, such as surface texturing, can be applied to and is necessary for polycrystalline cells. For monocrystalline silicon cells, the thickness is maximized for increased absorption, which the material can afford since single crystal silicon has a long minority carrier diffusion length. By implementing efficient light trapping on a

thin layer that is tens of microns thick, the light path is lengthened but the carrier path remains small. This results in better performance from polycrystalline cells, which are made from electrically poorer material with lower diffusion lengths from the crystallographic defects. Impurities segregating at grain boundaries also make leakage currents a problem in polycrystalline silicon. So that the device is not dominated by recombination at grain boundaries, the ratio of the lateral size to the layer thickness should be maximized, with grain sizes at least on order of the layer thickness (see Figure 1.2). A possible method to engineer large grains in polycrystalline silicon with low temperature processing is to selectively nucleate crystals in a-Si, and enlarge the crystals with solid-phase crystallization.

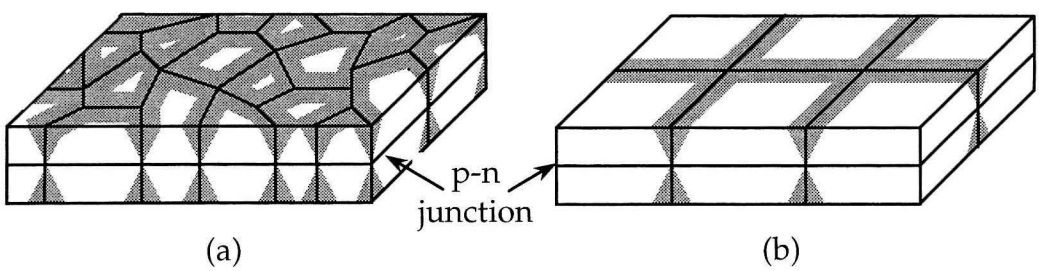

Figure 1.2. (a) Schematic of small grain polycrystalline silicon with grain sizes on order of the film thickness. A large percent of the carriers generated will be lost to grain boundaries; these regions are shaded in gray. (b) Schematic of polycrystalline silicon engineered with larger grains, with a lower percentage of carriers lost at grain boundaries than (a).

1.5 Outline of the thesis

We have explored a procedure for making polycrystalline silicon, dubbed selective nucleation and solid-phase epitaxy (SNSPE). In SNSPE, nucleation sites seed solid-phase crystallization of an a-Si layer. Two systems were explored: nucleation by indium, a metal that forms a eutectic alloy with silicon (Chapter 3), and nickel, a metal that forms a silicide (Chapter 4). Positron annihilation spectroscopy experiments were performed to explore the nature of the open volume defects in solid-phase epitaxy (Chapter 5).

Chapter 2 Solid-phase Epitaxy

2.1 Introduction

Selective nucleation and solid-phase epitaxy (SNSPE) is a crystal growth process to engineer large grain sizes in polycrystalline silicon crystallized from a-Si at low temperatures of 600 °C and below. This chapter reviews aspects regarding solid-phase epitaxy, including nucleation and dopant effects that are important in understanding experimental observations regarding SNSPE in chapters 3 and 4.

2.2 Solid-phase epitaxy

Solid-phase epitaxy (SPE) is a crystal growth process where a metastable amorphous layer in contact with a crystalline layer converts to the lower energy crystalline phase by reordering of the atoms at the interface. Unlike liquid phase epitaxy and vapor phase epitaxy where the atoms are highly mobile, atom movement in SPE is usually limited to within a few bond lengths of the interface [8].

Silicon forms strong covalent bonds that are highly directional in a tetrahedral pattern. Atoms in the crystalline phase are arranged in a diamond

lattice with unstrained, tetrahedrally oriented bonds. Atoms in the amorphous phase are also thought to be tetrahedrally bonded but with no long range order, which results in strained bonds. Therefore, silicon is at a lower free energy in the crystalline phase.

The velocity of the interface exhibits an Arrhenius temperature dependence, $v = v_0 e^{-E_a/kT}$, where E_a is the activation energy. The most accurate values for the pre-exponential factor and activation energy are v_0= 4.64×10^8 cm/s, and E_a = 2.7±0.02 eV, deduced from regrowth of a 2.2 μm thick a-Si layer formed by MeV ion implantation [9]. SPE of vacuum deposited a-Si has also been studied, which has the same activation energy, but absolute rates are half of those found in ion implanted samples [10]. The reduction in the growth rate may be due to H incorporation into the a-Si that has been shown to reduce the intrinsic growth rate by half.

Other factors observed to affect the crystallization rate of silicon are crystal orientation and impurity type and concentration. In the definitive experimental data set on orientation dependence, the growth rate was measured for orientations every 5° from <100> to <111>, and from <111> to <110> [11]. <100> oriented interfaces exhibit the fastest growth rate and <111> exhibit the smallest. Twinning is also observed for <111> oriented samples with a sharp decrease in growth rate after ~100 nm.

E - enhancement, NE - no effect, R - retardation

B E 40 (0.6at%)	**C** NE,R	**N** R	**O** R	**F** R
Al E 66 (1at%)	**Si** NE	**P** E 8 (0.8at%)	**S**	**Cl** R
Ga E 5 (0.4at%)	**Ge** NE,R	**As** E 5 (0.6at%)	**Se**	**Br**
In E 2.5 (0.6at%)	**Sn** NE,R	**Sb** E 2.5 (0.8at%)	**Te** E 2.5 (0.08at%) R (>0.14at%)	**I**

Figure 2.1. Electrically active impurities enhance growth rate, and suppress random nucleation [8].

Impurities strongly effect the growth rate of SPE. A summary of enhancements and retardations is found in Figure 2.1 [8]. One conclusion that can be made is that electronic dopants enhance the growth rate while other impurities that are not known to be shallow donors and acceptors retard the growth rate, suggesting the enhancement is an electronic effect. A detailed study of the growth enhancement with varying concentrations of As and varying anneal temperatures [12] found that the enhancement decreased with increasing temperature, which can explained by the temperature dependence of the intrinsic carrier density. As the temperature increases, the intrinsic carrier contribution increases and overtakes the extrinsic carrier contribution. Further evidence that it is an electronic effect comes from studies that show that P and B compensation results in a growth rate equal to that of intrinsic Si [13].

The compensation effect is explained by a Fermi level shifting model in which the dopants shift the Fermi level, thus changing the population of certain charged defects responsible for the dopant enhancement. In particular, a Fermi level shifting model by Williams and Elliman [14] and revised by Aziz *et al.* [15] matches the experimental data well. In epitaxy, the interface can be described as having a series of ledges that grow by atoms adding to kinks in the ledges. The kinks can alternately be thought of as point defects that move down the edge of the ledge as the crystal grows. A certain number of these point defects are charged, and their population is controlled by the location of the Fermi level. The charged defects could be vacancies or dangling bonds. Suni *et al.* [16] suggested that the defect could be charged vacancies, while Williams and Elliman addressed the dangling bond case. These models and others that have been proposed to explain the electronic dopant enhancement are summarized and discussed in Aziz *et al.* [15].

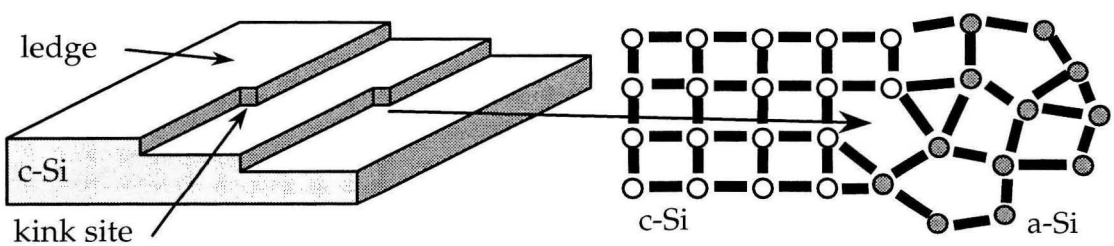

Figure 2.2. Schematic of the crystalline growth interface with ledges and kink sites that could be vacancies or dangling bonds.

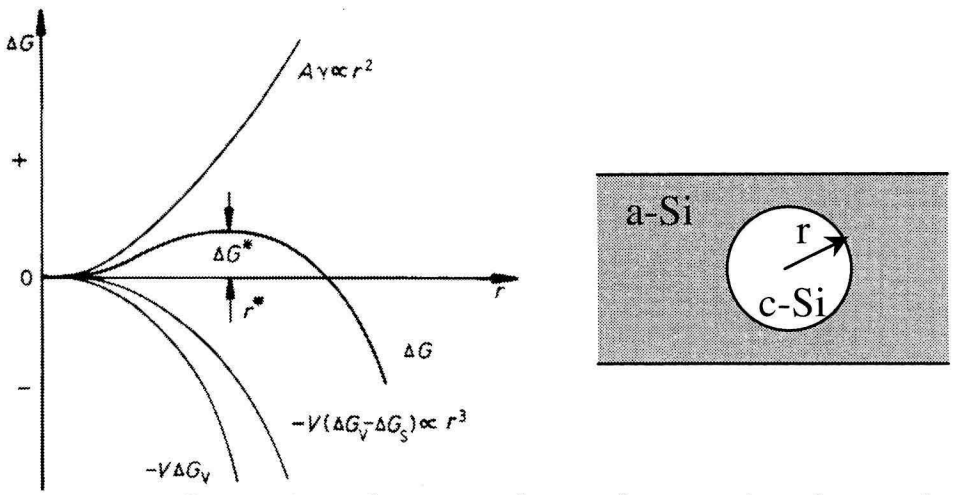

Figure 2.3. Competition between the surface tension that scales with r^2 and the volume free energy reduction that scales with r^3 results in an activation energy, ΔG^*, to grain growth in homogeneous nucleation. The critical size for stability is r^* [17].

2.3 Nucleation

Classical nucleation theory offers satisfactory insight into the different characteristics observed in crystal nucleation of a-Si, such as a thermal activation energy barrier and incubation time (the transient time period at the start of an anneal when no nucleation is observed).

As the new crystalline phase nucleates out of the amorphous matrix, the Gibbs free energy change is determined by the volume free energy reduction, $V\Delta G_V$, due to the reduction in energy from the volume substitution of lower energy c-Si for a-Si, and an increase in interfacial energy, $A\gamma$, between the a-Si matrix and c-Si nucleus. The total free energy change is

$$\Delta G = -V\Delta G_V + A\gamma .$$

The change in free energy versus nucleus size exhibits a barrier to nucleation, ΔG^* (see Figure 2.3). The peak of the barrier correlates with a critical radius, r^*, that a nucleus must achieve for stability. Otherwise, it may dissolve into the matrix.

When an anneal starts, many small nuclei form, most of which redissolve. As time progresses, the crystallite distribution includes larger and larger but still subcritical grain sizes. In a finite time, thermal fluctuations in atomic arrangement eventually form a crystal with the critical size for stability. This time is the incubation time. Eventually the system reaches a steady state distribution until the amorphous silicon is fully crystallized.

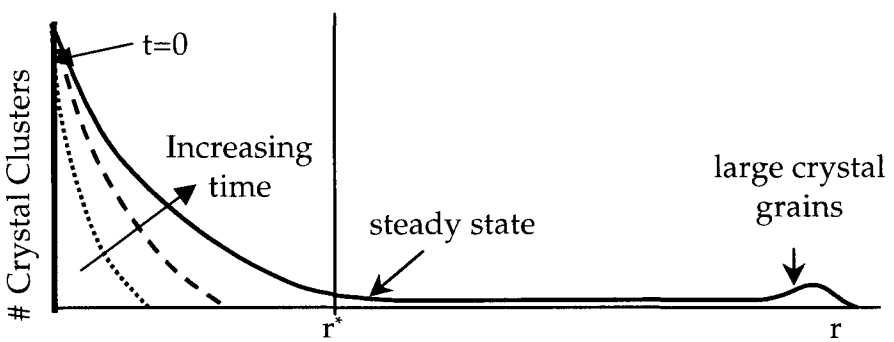

Figure 2.4. Schematic of the crystallite size distribution as a function of time.

In a-Si, the nuclei form by random fluctuations in the matrix. If the homogeneity is broken by defects or impurities, the nucleation occurs much faster. Heterogeneous nucleation between the a-Si and a metal interface can be shown to lower the barrier to nucleation, resulting in a shorter incubation time.

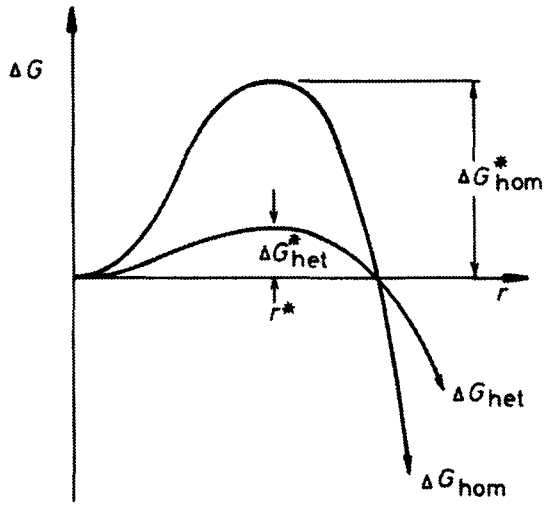

Figure 2.5. Heterogeneous nucleation decreases the activation energy to crystal growth, relative to homogeneous nucleation [17].

2.3.1 Random nucleation in undoped and doped a-Si thin films

The process of random nucleation competes with crystal growth when engineering large grains in polycrystalline silicon. Therefore it is important to characterize the incubation time for random nucleation and the nucleation rate. Crystallization by random nucleation was investigated in 100 nm thick a-Si films on SiO_2, fabricated by implantation of polycrystalline silicon [18]. The random nucleation rate increased with increasing temperature, and was found to have an activation energy of 5.1 eV for the temperature range 540-660 °C. The incubation time decreased with increasing temperature, and had an activation energy of 2.7 eV. At 600 °C, the nucleation rate was 6×10^{7} $cm^{-3}\cdot s^{-1}$ and the incubation time was 10 hours.

In doped films, the nucleation rate was found to decrease with increasing concentration of dopants phosphorus, boron, and arsenic, over the concentration range of 0.1-1 at. % at 690 °C [10]. The concentration range studied was on the threshold of the solubility limit at the anneal temperature. The lowest concentration in which a decrease is seen is likely determined by the intrinsic carrier concentration, while the upper limit is determined by the solubility limit.

2.3.2 Metal induced nucleation

Metal induced crystallization of a-Si has been shown to occur with an assortment of metals: Au, Ag, Al [19], In [20], Cu, Ni [21,22] and Pd [23]. All of these metals crystallize Si below 600 °C, which make metal-induced crystallization a good method to selectively nucleate crystals at the low temperatures required for processing polycrystalline silicon on soda-lime glass. These metals can be grouped into two categories: (i) those that form simple eutectic phases with Si, with low eutectic temperatures (Au, Ag, Al, In), and (ii) those that form silicides (Cu, Ni, Pd).

While a complete understanding of the interface reactions that occur is not yet possible, plausible mechanisms have been advanced for growth (rather than nucleation) in which an alloy or silicide [24] front can move through the a-Si, leaving c-Si in its path. For both eutectic and silicide forming metals,

heterogeneous nucleation of c-Si occurs without a measurable incubation period, so the mechanisms for nucleation and growth may be related.

Chapter 3 Polycrystalline Si Films by Indium Induced Nucleation

3.1 Introduction

Selective nucleation and solid-phase epitaxy (SNSPE) is a crystal growth technique that exploits the transient incubation time in crystallization processes to engineer larger grain sizes and controlled polycrystalline microstructures. Selective nucleation occurs by an interface reaction between an amorphous silicon layer and metal nucleation sites, which can be fabricated by deposition onto the surface or ion implantation. Crystal growth proceeds by lateral solid-phase epitaxy from the nucleation sites, during the incubation time for random nucleation. The largest achievable grain size by SNSPE is thus approximately the product of the incubation time and the solid-phase epitaxy rate. Electronic dopants, such as boron, phosphorus, and aluminum, enhance the solid-phase epitaxy rate and affect the nucleation rate.

In this chapter, selective nucleation and solid-phase epitaxy (SNSPE) was applied to 100 nm thick a-Si using deposited indium as a nucleation seed. Indium was deposited through a mechanical mask. Photolithography was

avoided since it is an expensive process, and development of a low-cost method is the goal of this work.

Indium has been shown to nucleate silicon in indium-implanted samples [20]. An amorphous to polycrystalline transition occurred within minutes at a critical temperature that varied with indium concentration. Indium droplets were proposed to move through the a-Si, leaving a c-Si trail. A different crystallization mechanism is expected in the work in this chapter, since the deposited indium forms an interface with the silicon at the surface not internally, and is not likely to enter the silicon at the concentrations introduced by implantation. Indium forms a eutectic alloy with silicon at 156.6 °C, and is a benign impurity that forms a p-type semiconductor in Si.

3.2 Procedure

The overall process (see Figure 3.1) is to fabricate a large-grained, poly-Si thin-film template, upon which a thicker device layer can be grown by an epitaxy technique, the final material having large grains with vertical grain boundaries. To maximize the extent of grain growth during the incubation time for random nucleation, crystals are nucleated at specified locations in a periodic array using metal induced nucleation. Metal induced nucleation enables crystal nucleation at these specified sites with a shorter incubation period than for random nucleation [25]. Once random nucleation starts, further growth of the seeded crystals will be

inhibited by impingement of randomly nucleated grains, thus limiting the grain size to that which is achievable before random nucleation occurs. The thin film, fully crystallized by further annealing, can then be used as a template upon which a thicker silicon layer is grown, either by a vapor phase epitaxy process by CVD or sputtering, or by vertical solid-phase epitaxy of deposited a-Si layer grown on the template.

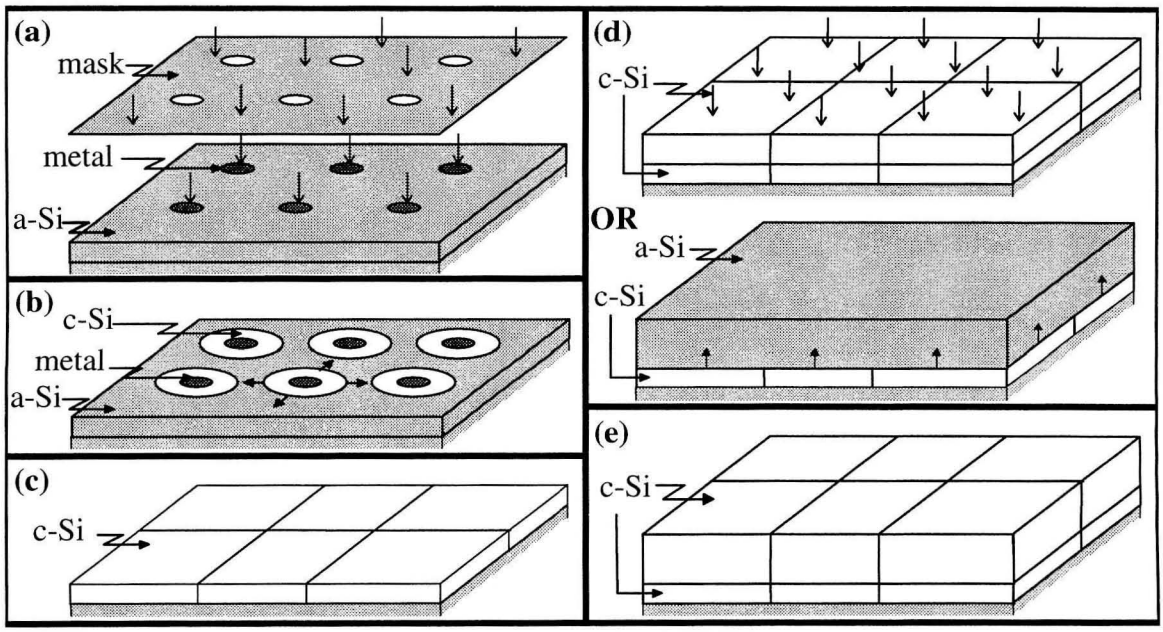

Figure 3.1. SNSPE process: (a) metal dots are deposited on a-Si layer, (b) sample is annealed to nucleate and grow c-Si, (c) seeded grains impinge on each other; film is completely crystallized, (d) additional layer is grown on thin film template, either by epitaxial vapor deposition or by vertical SPE, and (e) the top layer has similar grain size as template.

3.3 Experiment

Experiments were performed to assess the use of SNSPE for crystallization of 100 nm a-Si films, deposited by electron beam evaporation at 100°C onto thermally grown SiO_2 films on silicon substrates in ultrahigh vacuum. Films were doped by implantation with 13 keV $^{10}B^+$, 37 keV $^{31}P^+$, or 30 keV $^{27}Al^+$. The energies of the ions were chosen such that the peak of concentration was at half the thickness of the layer. For the boron implants, samples with the following doses, with peak concentrations in parentheses, were made: 1×10^{14} cm^{-2} (2.0×10^{19} cm^{-3}), 3×10^{14} cm^{-2} (6×10^{19} cm^{-3}), 1×10^{15} cm^{-2} (2.0×10^{20} cm^{-3}), 5×10^{15} cm^{-2} (9.8×10^{20} cm^{-3}), and 1×10^{16} cm^{-2} (2.0×10^{21} cm^{-3}). For the phosphorus implants, samples with the following doses, with peak concentrations in parentheses, were made: 3×10^{14} cm^{-2} (6.1×10^{19} cm^{-3}), 1×10^{15} cm^{-2} (2.1×10^{20} cm^{-3}), 5×10^{15} cm^{-2} (1.1×10^{21} cm^{-3}), and 1×10^{16} cm^{-2} (2.1×10^{21} cm^{-3}), 5×10^{16} cm^{-2} (1.1×10^{22} cm^{-3}). For the aluminum implants, samples with the following doses, with peak concentrations in parentheses, were made: 3.3×10^{13} cm^{-2} (6.6×10^{18} cm^{-3}), 5×10^{13} cm^{-2} (1.0×10^{19} cm^{-3}), 1×10^{14} cm^{-2} (1.9×10^{19} cm^{-3}), and 5×10^{14} cm^{-2} (1.0×10^{20} cm^{-3}).

Indium dots, deposited to a 20 nm thickness by thermal evaporation in a high vacuum evaporation chamber, were used to nucleate the silicon crystals. The silicon layer was cleaned in a RCA solution (5:1:1 H_2O:H_2O_2:NH_4OH, at 80 °C for 20 minutes), and then dipped in buffered HF to etch the oxide before deposition. The indium was thermally evaporated through a mechanical mask with a square

grid of 5 μm diameter circles with two sets of periodic spacings, 20 μm and 25 μm, at a base pressure of 4×10^{-6} torr. Anneals were performed in a vacuum furnace with a pressure of 5×10^{-7} torr. The samples were first annealed at 450 °C for 20 minutes to induce selective nucleation without substantial reduction in the incubation time. The samples were then annealed at 598 °C, 620 °C, and 650 °C for crystal growth, at which temperatures the indium evaporates off of the samples. Anneals were halted periodically to take optical images of the samples, and the images were analyzed to extract growth and nucleation data. Samples were also studied with TEM using a Philips EM420 operating at 120 kV.

3.4 Results

After the short 450 °C anneal, the indium dot separated into many indium islands, as seen by transmission electron microscopy (TEM) in Figure 3.2(a). The discontinuous film seeded several silicon crystals per indium dot with a preferred <111> orientation, as seen in Figure 3.2(b). The multiply seeded crystals reduce the maximum possible grain size. Indium nucleated silicon crystals before the onset of random nucleation. The indium nucleated and randomly nucleated crystals were dendritic with twin boundaries. Auger spectroscopy of the samples showed that the indium incorporation 3 nm into the silicon surface layer was limited to the areas onto which indium was initially deposited.

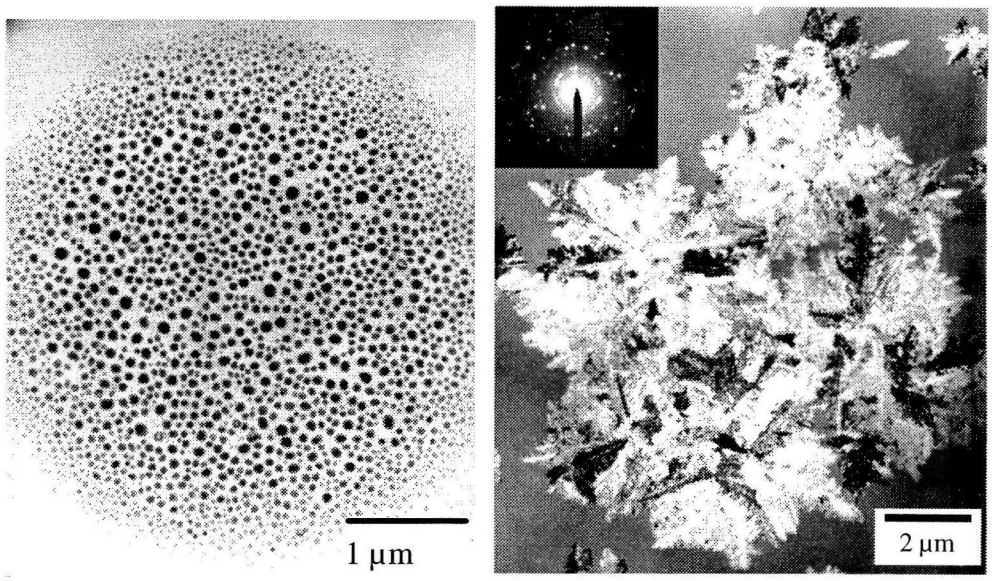

Figure 3.2. TEM image of (a) 20 nm thick In dot after a 450°C anneal, and (b) a cluster of crystals nucleated by In and annealed at 600°C. The inset shows a <111> polycrystalline diffraction pattern.

The SPE rate (see Figure 3.3) was determined by measuring the movement of growth fronts at successive anneals. The incubation time was estimated from counting the random nuclei that occurred between the indium-seeded crystals as a function of time. Though the nucleation rate that is calculated from this data is not corrected for the decreasing a-Si fraction, which would result in a higher nucleation rate than observed, it still gives a good estimate of the incubation time and relative nucleation rates. From the nucleation data, an estimate of the incubation time was made by using the first few nonzero data points and linear extrapolation to where the nucleation density equals zero. With these methods, the error in the incubation time was estimated to be 10%, and for the growth rate,

10^{-5} μm/s. These errors were taken from the standard deviation of the measurements. Further errors can arise from uncertainty in the temperature of the furnace, which was calibrated with a thermocouple wafer. Since the crystallization parameters are sensitive to temperature, the absolute values may be offset, but the trends should be present.

The growth rate of the undoped silicon coincided with the dependence found in the literature for randomly nucleated crystals in thin films [18], which are limited in growth by crystallization fronts with <111> orientation. This suggests that the indium had little influence on the growth kinetics. The incubation time was 2 hours at 620 °C, which is less than the incubation time of 5 hours seen in the literature [18]. In this case, the benefits of nucleating crystals before random nucleation occurs are small. When single nuclei are seeded at the indium spots, they are nucleated before random nucleation, but after 10 hours, the size of the randomly nucleated crystals are of the same order as the seeded crystals (see Figure 3.4).

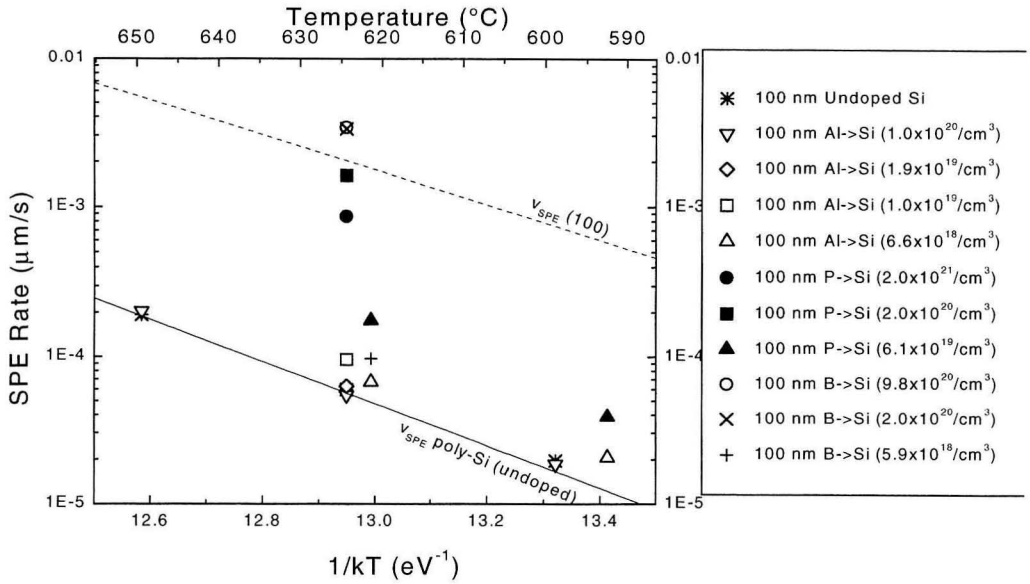

Figure 3.3. Solid-phase epitaxy rate for undoped and doped samples at various temperatures. The data points are compared to dependencies found for <100> oriented interfaces [10] (dotted line) and for randomly nucleated crystals [18], which are limited by <111> growth interfaces (solid line).

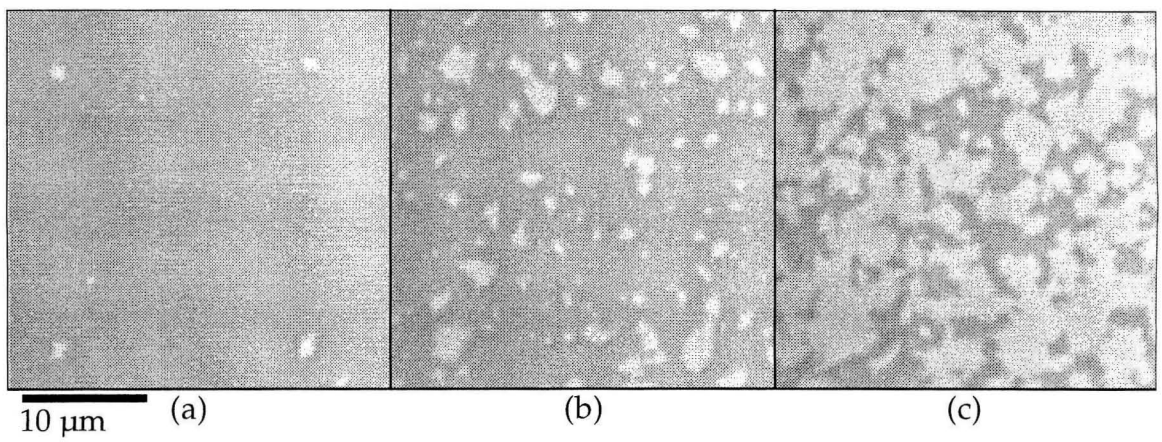

Figure 3.4. Optical micrographs of undoped silicon after various anneal times. The white areas are crystalline silicon, and the gray areas are amorphous silicon. Indium nucleated crystals are obvious after (a) 3.5 hours with few randomly nucleated crystals, (b) 7 hours, and (c) 10.5 hours, the indium nucleated crystals are indistinguishable from the random nucleation.

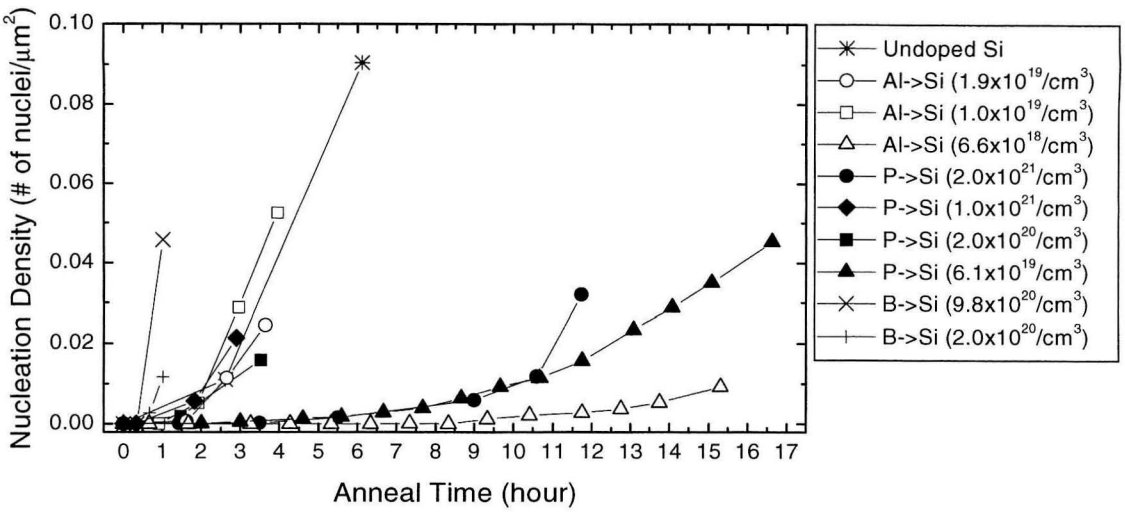

Figure 3.5. Nucleation density versus time for undoped and doped samples.

The B-doped samples exhibited a very fast growth rate and nucleation rate, and the lowest incubation time. The incubation time for the sample with a peak concentration of 2.0×10^{20} cm^{-3} was 35 minutes, and for the sample with peak concentration of 9.8×10^{20} cm^{-3}, it was 20 minutes, rather than the two hours for undoped Si. The reduced incubation time relative to undoped silicon was probably a result of the peak concentrations in these samples being higher than the solid solubility of boron in silicon at 600 °C, which can be extrapolated to be 6×10^{18} atoms cm^{-3} [26]. Precipitates could have formed and seeded crystals. The growth rate for both samples was basically the same at 3×10^{-3} μm/s, which is 50 times the growth rate observed for undoped silicon. A possible scenario is that both samples precipitated boron, with the higher concentration sample precipitating more, which resulted in a higher nucleation rate. The higher concentration sample also depletes more boron during precipitation, resulting in

the same concentration of dissolved boron in the matrix, and therefore similar growth rates.

The full range of B-doped samples was studied using a different configuration (see Figure 3.6). The amorphous silicon layers described above were patterned into rectangular islands by photolithography (see Figure 3.7). A 2 μm wide strip at one end was implanted with 8×10^{15} cm^{-2} of indium. The geometry of the structures is different from the deposited indium, since many crystallites can be nucleated in a row at the edge of the implanted indium region, which constricts the growth direction for each crystal. This may lead to different growth rates, but the trends should be universal. Though the fastest growth rate was seen for peak concentrations on the order of 10^{20} cm^{-3}, these concentrations also exhibited lower incubation times, so the estimated grain size for all boron concentrations investigated and undoped silicon were comparable at 1-2 μm.

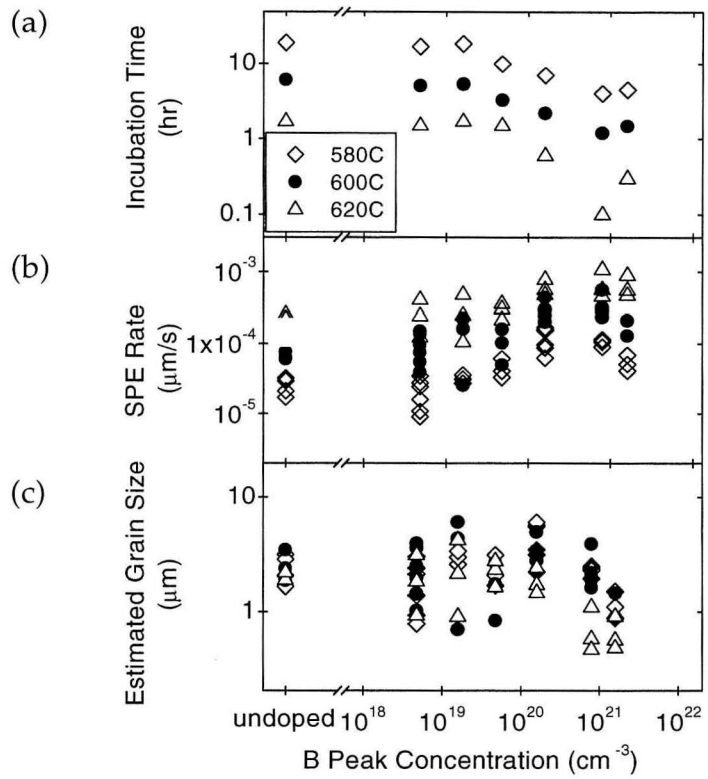

Figure 3.6. Comparison of experimental (a) incubation time, (b) growth rate, and (c) estimated grain size for undoped and B doped silicon with various concentrations and annealing temperatures, for patterned silicon islands with implanted indium seed regions.

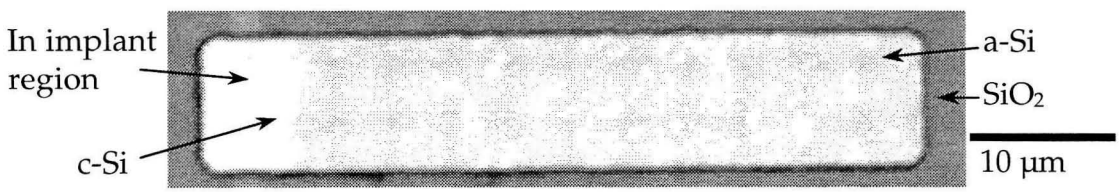

Figure 3.7. Optical micrograph of a 100 nm thick, patterned silicon island on SiO_2. The amorphous silicon was P-doped with a dose of 1×10^{15} cm^{-2}. The light gray strip at left is the indium-implanted region (dose 8×10^{15} cm^{-2}). Within the rectangle, the white regions are crystalline silicon, the gray regions are amorphous silicon.

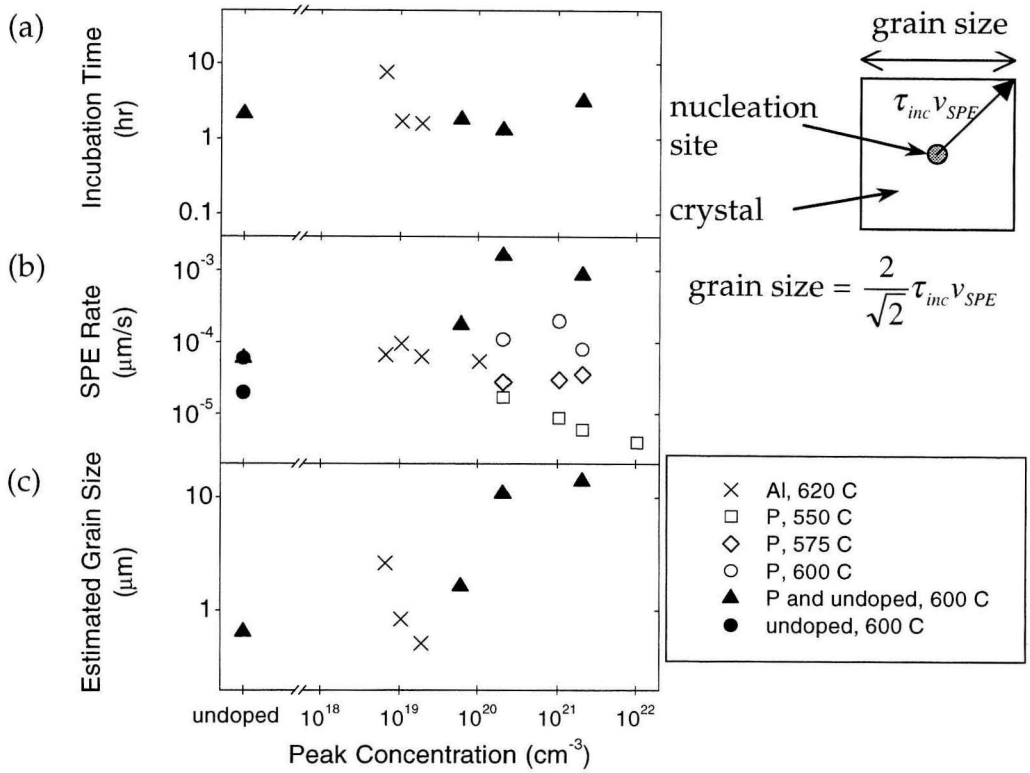

Figure 3.8. Comparison of experimental incubation time (a), growth rate (b), and estimated grain size (c) for undoped, P-doped and Al-doped silicon with various concentrations and annealing temperatures. The undoped, aluminum, and phosphorus (□) data was taken from samples nucleated from deposited indium dots. All open symbols were patterned silicon islands with implanted indium seed regions.

For P-doped silicon, the incubation times were roughly the same as the undoped case, but all concentrations exhibited enhancements in the growth rate (see Figure 3.8). The largest enhancement occurred for a peak concentration of 2.1×10^{20} cm^{-3}, with a growth rate of 1.6×10^{-3} μm/s, which is 27 times greater than the rate for undoped silicon.

Patterned silicon samples with indium implantation, described for B-doped samples above, were made on P-doped layers as well. The *growth rate was*

monitored for 550 °C, 575 °C, 600 °C, and 620 °C anneals (see Figure 3.8). The solid solubility of phosphorus in crystalline silicon at 600 °C is extrapolated to be 6×10^{19} atoms cm^{-3} [26], with the solubility in amorphous silicon expected to be higher than that of crystalline silicon [27]. At 550 °C, there was a retardation of the growth rate with increasing phosphorus concentration, which may be from precipitates that originate from the supersaturation of phosphorus in the amorphous silicon at this anneal temperature. As the anneal temperature increased, the growth rate behavior changed such that peak concentrations of 10^{20} cm^{-3} gave a larger growth rate and estimated grain size than the undoped case. This may reflect a transition from supersaturation at the lower temperatures to solubility in the amorphous phase at higher temperatures. In samples where the phosphorus peak concentration is above the phosphorus solubility in c-Si but lower than the phosphorus solubility in a-Si, phosphorus may segregate to the a-Si as the crystal grows.

The aluminum doped sample showed little change from the undoped case. Both the growth rate and incubation time were within 10% of the undoped case. At 620 °C, Al has a solid solubility of 7×10^{18} atoms cm^{-3} [26].

In general, the excess of impurity atoms above the solubility limit may have driven the impurity atoms to precipitate or segregate at the growth interface. The impurity clusters could then pin the growth interface and result in a lower

effective growth rate with increasing dopant concentration. The precipitates could also increase the nucleation rate and decrease the incubation time.

Ultimately, the important value to extract is the grain size. Grain size was very difficult to determine from TEM images, because of the complicated growth fronts and twin boundaries from the dendritic grain growth, and the bend contours in the TEM images due to deformation of the thin layer after TEM sample preparation. It was estimated from TEM images that grains roughly 10 microns in size were achieved in for P-doped Si with a peak concentration of 1.1×10^{21} cm^{-3}. This correlates well with the grain size estimated from the product of the incubation time and growth rate, times a geometric factor of $2/\sqrt{2}$, (see Figure 3.8(c)).

3.5 Conclusions

Selective nucleation and solid-phase epitaxy was demonstrated for undoped, B-doped, P-doped, and Al-doped silicon samples. The deposited indium dots, however, did not lead to a single crystal per nucleation site, which limits the maximum size of the crystals. Dopant enhancement was observed at these high concentrations, with phosphorus and boron showing the most promise. The anneal times for this technique, >10 hours, is too long to be feasible for large-scale production. The indium nucleated crystals before the onset of random nucleation, but did not appear to affect the crystallization process. Dendritic

growth resulted in numerous twin boundaries. The layers exhibited random orientations, with random nucleation occurring after 2 hours of anneal at 600 °C for undoped silicon.

Chapter 4 Ni-induced Crystallization of Thin-film Si

4.1 Introduction

Metal induced crystallization of amorphous Si with Ni has been shown to occur below 600 °C [21,22], making it compatible with the use of conventional low cost soda-lime glass substrates, and with growth rates much faster than the metal-induced crystallization with indium or unseeded growth seen in Chapter 3. In addition to the fast growth rate, Ni-mediated polycrystalline Si has a preferred <110> texture, which has been noted to have very good electrical characteristics. Most atoms along grain boundaries between <110> oriented grains are fully coordinated, though strained, so that there is a lower dangling bond density than high angle grain boundaries. Ni has a high diffusivity and solubility in Si at the anneal temperature of 600 °C, however, so as the sample cools to room temperature, the solubility drops, and Ni precipitates can form along grain boundaries that act as shorts or recombination centers. There are methods to remove, or getter, Ni already incorporated in the silicon out of the active region and into inactive, sacrificial getter layers. Two techniques that rely on the higher solubility of the impurity in the getter layer are Al gettering [28-

30], in which an Al layer is deposited on the Si layer, or P gettering [31,32], with a highly P-doped layer in the silicon.

In this work, nickel was applied as a nucleation seed in selective nucleation and solid-phase epitaxy (see Figure 4.1). Instead of vapor deposition through a mask, a different non-lithographic method was tried for applying discrete metal nucleation seeds to avoid the multiply nucleated crystals per metal dot seen in the vapor deposited indium. Nanoparticles of nickel were suspended in isopropanol and applied to the Si in a spinner.

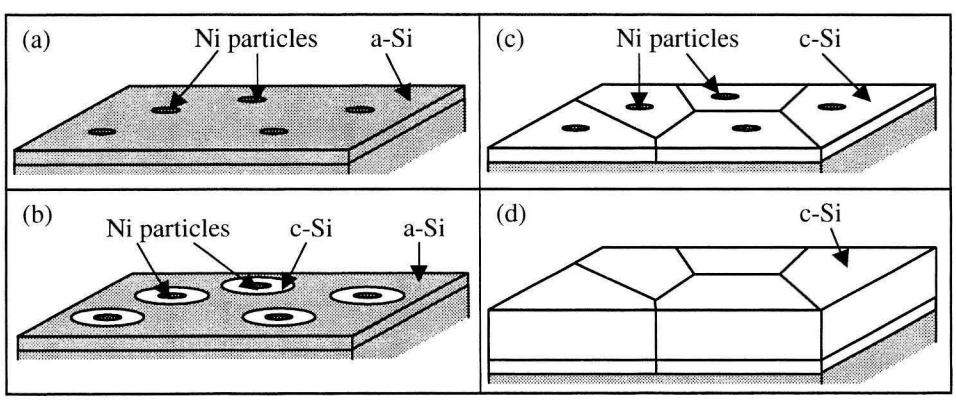

Figure 4.1. SNSPE process with Ni nanoparticles. (a) Nucleation sites are formed by random distribution of Ni particles on a-Si layer. (b) Layer is annealed ~600°C to nucleate and crystallize silicon. (c) Seeded grains impinge on each other to form completely crystallized film. (d) Silicon layer can be thickened by epitaxial deposition on the template with similar grain size as template layer.

4.2 Previously in the literature

Solid-phase crystallization of a-Si has been studied for an assortment of silicide forming metals, including Ni [21,22] and Pd [23]. In these cases, very fast nucleation and crystallization occurs at high metal concentrations. Ni forms several different silicides, Ni_2Si, NiSi, and $NiSi_2$, of which the $NiSi_2$ is thought to be dominant in the large-scale crystallization of Si [33]. $NiSi_2$, which has a cubic CaF_2 structure, is closely lattice-matched with c-Si with a misfit of only 0.4% [34].

In an in-situ transmission electron microscopy (TEM) annealing experiment of uniformly Ni-implanted a-Si layers [22], crystallization of the a-Si at 500 °C by the growth of single crystal needles was observed in real time. Ni was implanted with doses of 1×10^{15} cm^{-2} and 5×10^{15} cm^{-2} into 95 nm thick low-pressure chemical vapor deposited a-Si films. Under high resolution TEM, after the sample had cooled, a 5 nm thick silicide was seen at the a-c interface, suggesting that the silicide particles migrate through the a-Si matrix, leaving fine c-Si needles in its wake. For long range crystal growth, <111> crystal fronts should be parallel to the layer, which leads to preferential <110> texturing of the thin Ni-crystallized layer.

In films without uniform metal concentration, however, long-range crystallization appeared to depend on the concentration of dissolved metal in either the amorphous or crystalline silicon. In a study with 4 nm thick Pd deposited on 150 nm thick a-Si grown by low pressure chemical vapor

deposition at 480 °C [23], the a-Si directly below the Pd pads exhibited fast crystallization with 10-20 nm sized grains. In regions not covered by Pd, crystallization occurred along the edge of the metal. Long range crystallization, however, occurred where the Pd concentration would be higher in the a-Si due to diffusion, as in the case with two nearby Pd pads, or a Pd pad near the edge of the a-Si layer. No Pd was detected in the a-Si in these special cases with energy-dispersive x-ray analysis with TEM, suggesting that the concentration of Pd necessary for crystallization enhancement is below the detection limit.

4.3 Si crystallization by Ni particles

4.3.1 Ni ink

To reduce processing costs associated with implantation and photolithography, a method for applying nickel with potential for non-vacuum processing was used. Ni delivery by colloidal "inks" can eliminate the need for masks to form selective nucleation sites. Individual particles eliminate the problem seen in the indium deposited dots, which separated into tiny droplets that seeded different crystal orientations. The ink can also be applied to the substrate by an ink jet, which can print patterns without the use of lithography.

Ni nanoparticles (purchased from Nanophase) with particle sizes of 20-200 nm, were mixed with isopropanol to a nanoparticle concentration of 20 μg/ml.

The Ni particles formed aggregates in the solvent that settled at the bottom when undisturbed. It is unknown if the particles aggregate during the mixing process, or if the chemistry of the solvent induces aggregation. The ink was subject to ultrasonic treatment to break up the aggregates as much as possible.

4.3.2 Experiment

Samples were made by spinning the Ni ink onto substrates. The substrates were 100 nm thick, undoped a-Si, grown by electron beam evaporation on 100 nm thick, thermally grown oxides. Before application of the Ni particles, samples were prepared with an RCA cleaning solution (5:1:1 H_2O:H_2O_2:NH_4OH at 80 °C), and dipped in a diluted 5% solution of 48% HF and 18 MΩ water to remove the native oxide. A sample implanted with 37 keV $^{31}P^+$, with a fluence of 1×10^{15} cm^{-2} and peak concentration of 6.1×10^{19} cm^{-3} at half of the thickness was also studied.

The Ni ink was dropped onto the substrates and the samples spun on a spinner for 20 seconds at 1500 RPM. The isopropanol had evaporated completely by the end of the spin. The samples were then annealed in a vacuum furnace at 600 °C, and the growth analyzed with an optical microscope.

Full strength and well mixed ink formed a dense distribution of Ni particles of varying size. Large particles formed a ring of silicide around it. When the samples with large Ni aggregates were etched with a nitric acid solution, the large patches of Ni were removed and the Si below it, but the silicides that

formed on the edges remained, and were detected with x-ray fluorescence (XRF) microscopy (section 4.6). To avoid these large particles, the ink was left undisturbed until the large particles settled at the bottom and the top third of the bottle was clear. The ink was taken from the top layer.

The Ni particle distribution was random, with a mean nearest neighbor distance between particles of ~36 μm, with standard deviation of ~20 μm. The mean size of the particles was 3 μm and the surface coverage was 0.19%, as determined from the image analysis program, Scion Image. The crystals grew radially from the nucleation site. Needle-like crystal growth was observed by TEM (see Figure 4.2, Figure 4.7 and Figure 4.8). Undoped samples (see Figure 4.3) fully crystallized in ~20 hours (18 hours in more Ni dense regions), with no random nucleation observed. The P-doped samples (see Figure 4.4) showed a faster growth rate, and fully crystallized in ~13 hours, with 99% crystal fraction in 10 hours. The higher nickel solubility in the P-doped layer may have enhanced the crystallization rate.

The distance of the crystallization front from the nickel seed was monitored for each time step for both undoped and P-doped samples (see Figure 4.5). The range of distances at a particular anneal time can vary by 70 μm for the undoped silicon, and 100 μm for the P-doped. This could depend on the amount of Ni available or the Ni surface area. Velocities were compared to the radius of the crystal (see Figure 4.6). The growth rates in the undoped sample did not depend

on the nickel seed, but there was clear dependence for the P-doped sample. In colonies of Ni particles, the crystallization front appeared to reach for nearby crystals, which also suggested a concentration influence on growth.

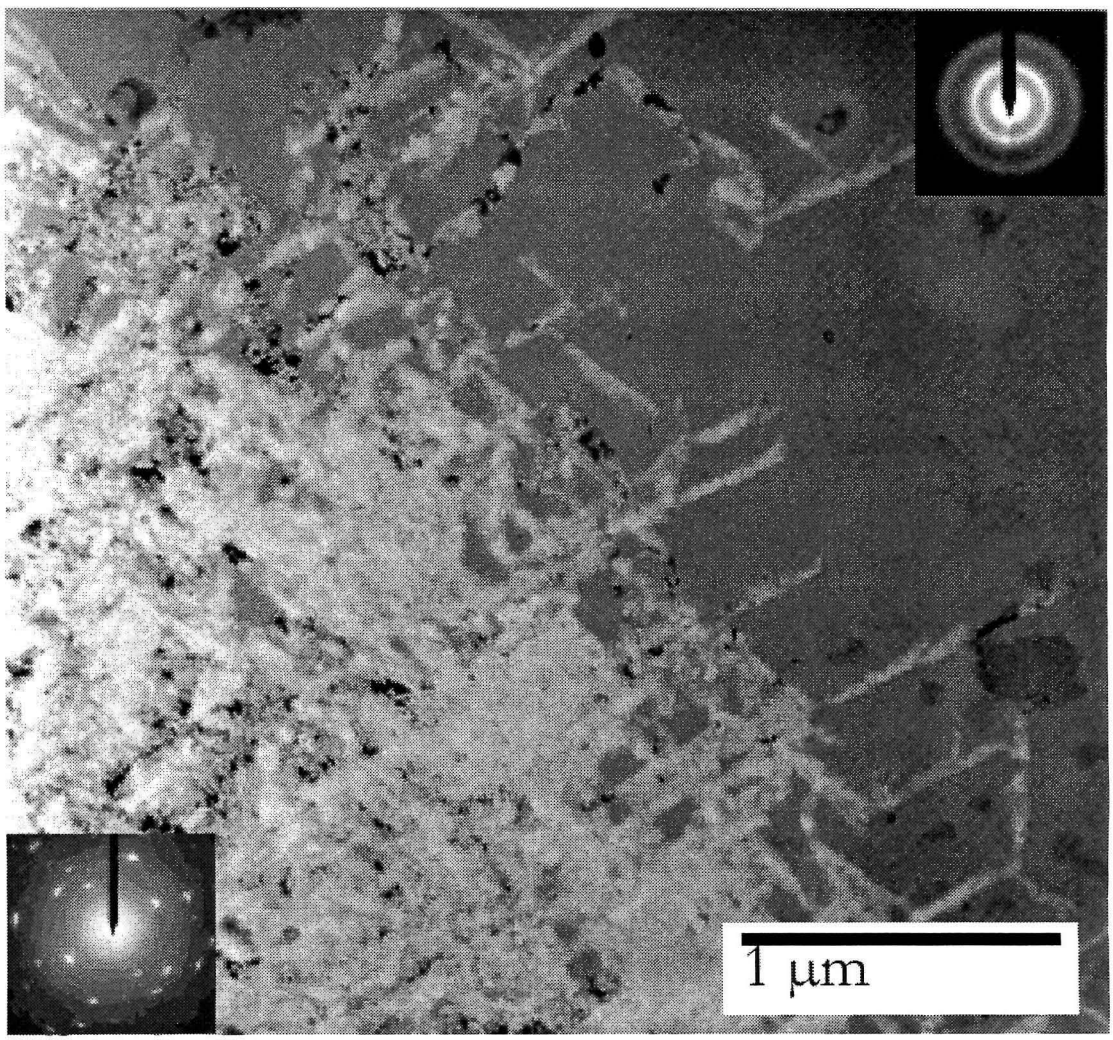

Figure 4.2. Bright field TEM image of a crystal-amorphous growth interface exhibiting the needlelike growth structure.

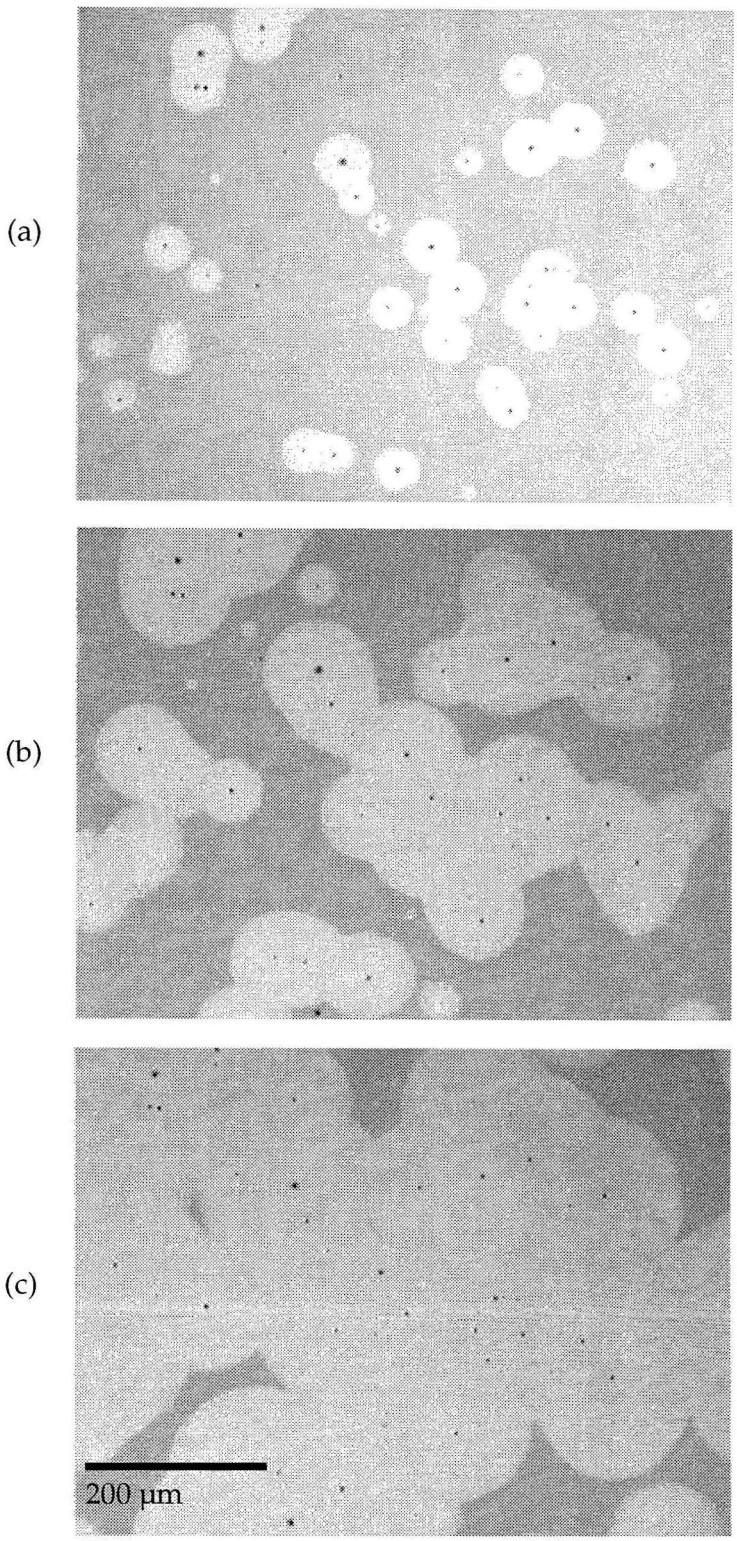

Figure 4.3. Optical micrographs of undoped amorphous silicon nucleated by randomly distributed nickel particles. The sample was annealed at 600 °C for (a) 4 hours, (b) 8 hours, and (c) 12 hours.

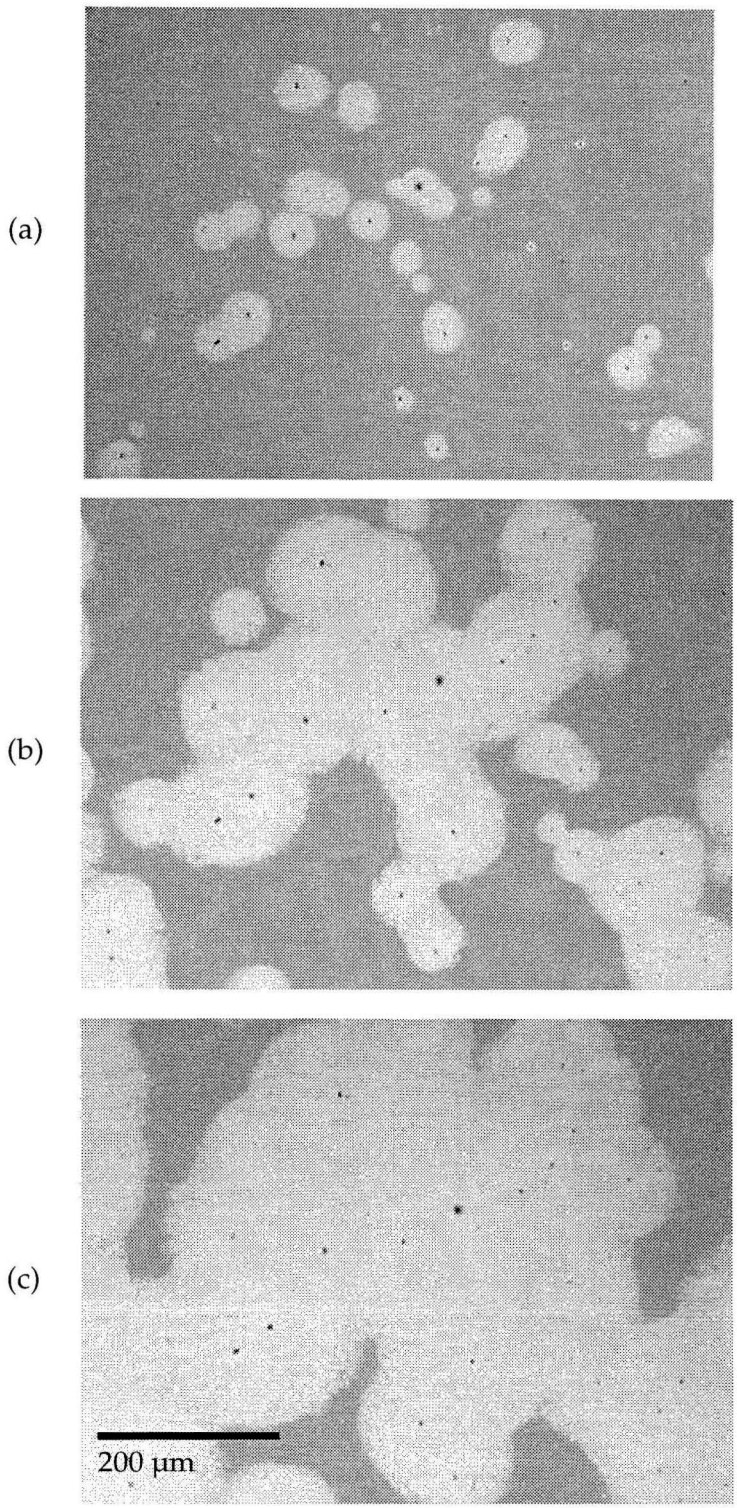

Figure 4.4. Optical micrographs of P-doped amorphous silicon nucleated by randomly distributed nickel particles. The sample was annealed at 600 °C for (a) 2 hours, (b) 4 hours, and (c) 6 hours.

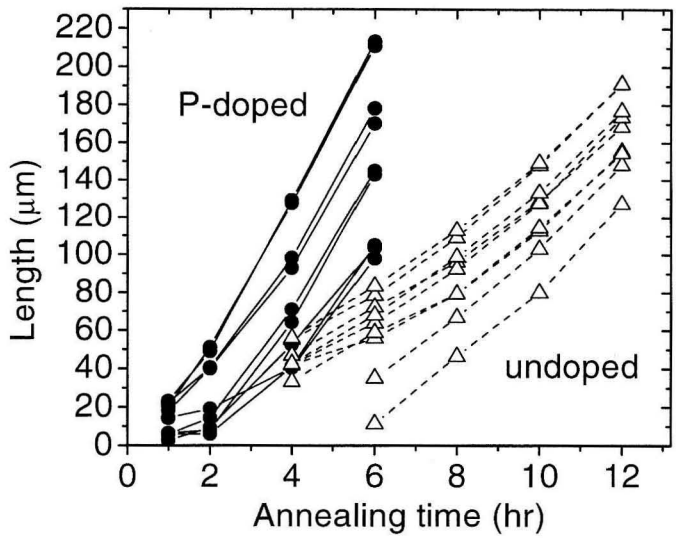

Figure 4.5. Distance of crystallization front from nickel nucleation seed versus annealing time for undoped and P-doped silicon layers. The samples were annealed at 600 °C.

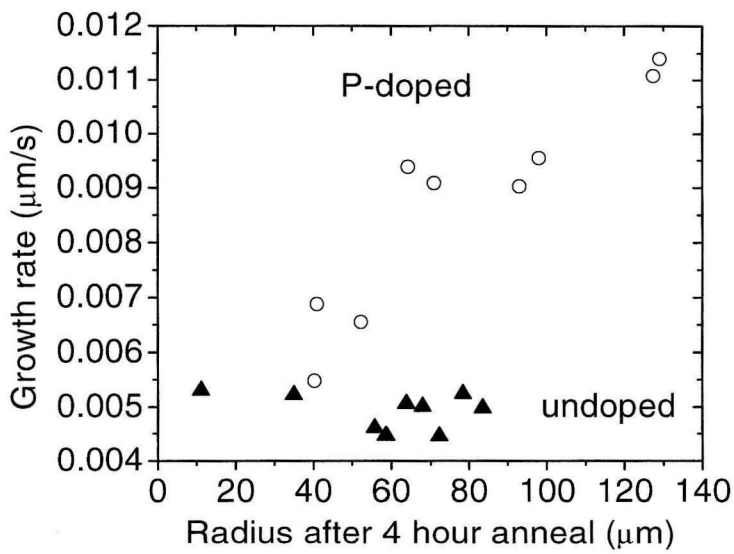

Figure 4.6. Growth rate of individual crystals annealed at 600 °C versus the crystal radius at the anneal time of 4 hours.

From TEM, different crystallization morphologies could be seen, depending on proximity to and size of the nucleation seed. Closer to the seeds, the

crystallization needles were wider, and the crystallization was dense. The "thickness" of the crystallization front, the length between the boundary of complete crystalline fraction and the farthest reaching needle, was also thinner. For cases where the Ni concentration is expected to be smaller, like crystals seeded by very small Ni particles or microns away from the larger nucleation seeds, very thin crystal needles would form a lacy pattern. For a given growth distance from the Ni particles, the P-doped sample had a less dense growth front than the undoped sample (see Figure 4.3 and Figure 4.4). Though crystallization by these needles result in many internal boundaries, selected area diffraction showed that they were low angle boundaries (see Figure 4.7).

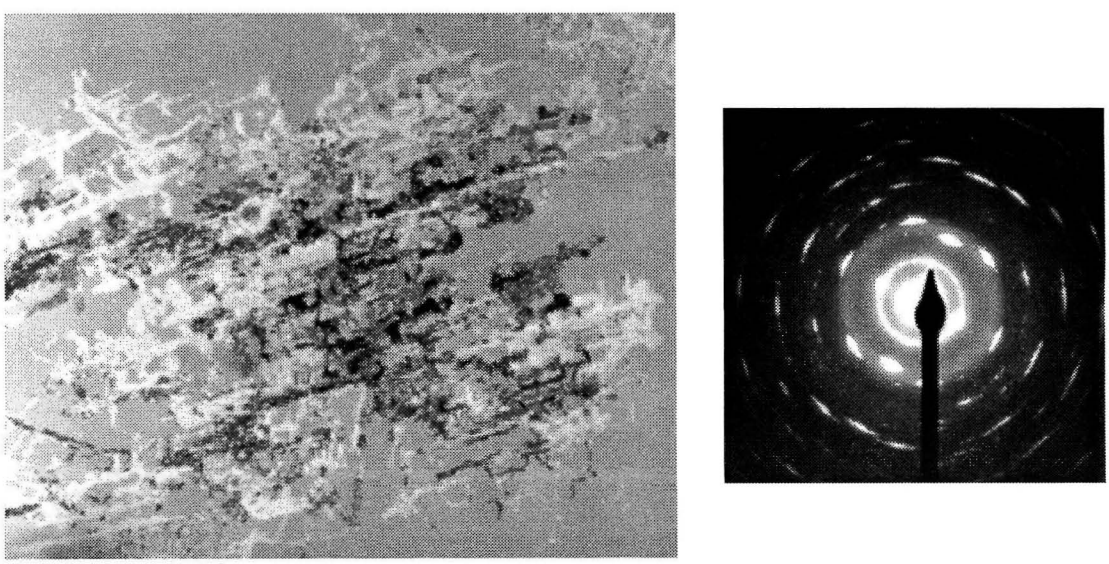

Figure 4.7. (a) TEM of a crystal nucleated by nickel and the (b) selected area diffraction pattern showing a 17° range in rotation.

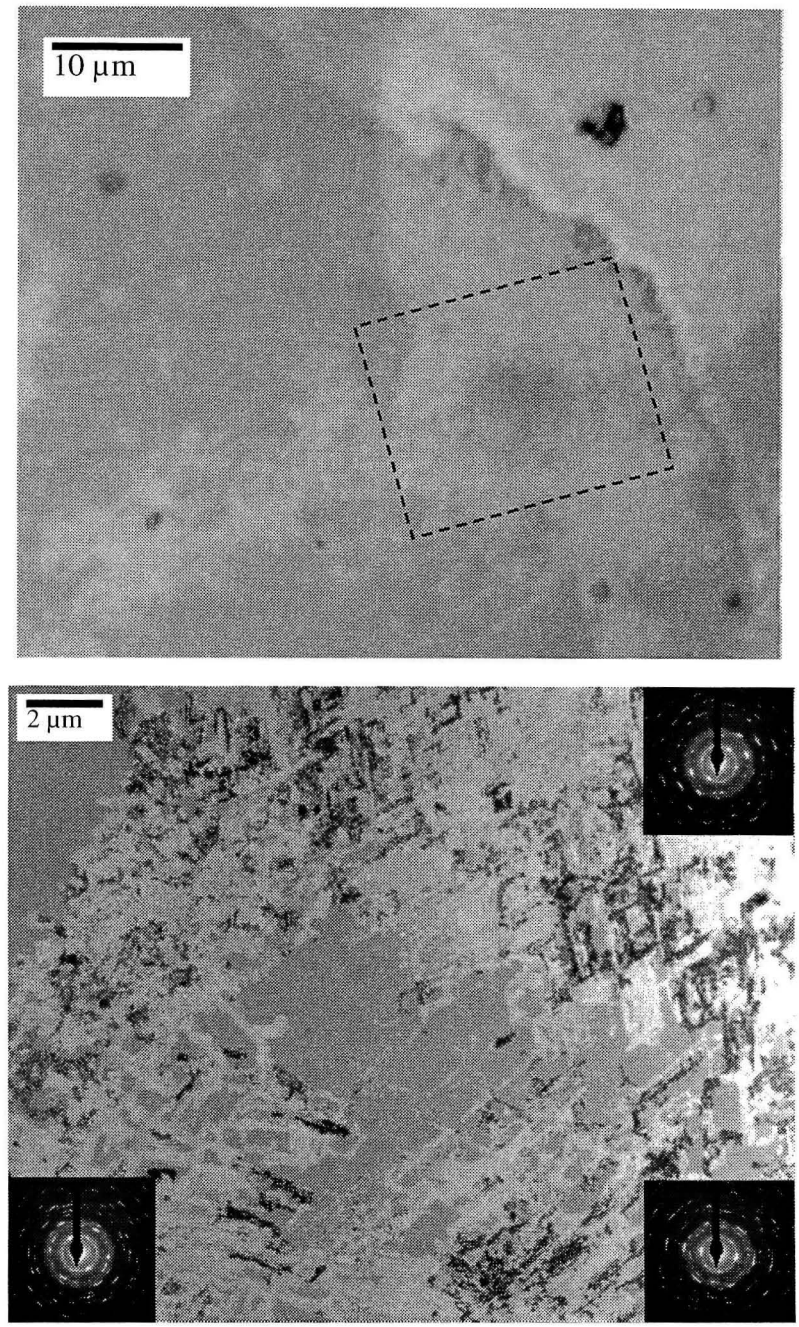

Figure 4.8. Optical micrograph and TEM image of Ni mediated crystallization in an undoped sample. In the TEM image, broad needles and very thin lacy needles can be seen.

4.3.3 Epitaxial layer growth

Microns thick silicon layers were grown by molecular beam epitaxy on the polycrystalline templates formed by Ni-mediated crystallization. The layers were deposited at 0.2-0.3 nm/s, with the substrate temperature held at 600 °C. The fully crystallized samples were first etched with a 3:7 HNO_3:H_2O solution at room temperature for 1 minute to remove excess Ni. Dark particles remained at the nucleation sites after the etch, and are thought to be silicides. The samples were then cleaned with an RCA clean and dipped in HF to remove the oxide. Once in the chamber, the substrates were heated to 200 °C for about 1 hour to desorb hydrocarbons, and then the temperature was raised to 600 °C for growth.

Three epitaxial films were grown. A 3 μm thick layer was grown on an undoped template, on which cross-sectional and plan view TEM was done. A 4 μm layer was grown on both undoped and P-doped substrates crystallized with an intentionally higher density of Ni to study the effect of a phosphorus gettering layer in the template, and a ~10 μm layer was grown on a P-doped template with a less dense distribution of Ni particles. Both of the thicker layers were analyzed with SIMS.

TEM on the 3 μm thick epitaxial layer showed that there were columnar grains with what appeared to be submicron boundaries. Plan view images of the 3 μm layer also looked different from the template, with few boundaries reminiscent of the growth needles. Some large 3 μm regions exhibited a single

orientation, but most grains were polycrystalline with ~0.5 μm size. Cross-sections showed columnar grains streaked with dislocations and strain contrast, with a modulating top surface, presumably from strain. Selected area diffraction patterns also showed dislocations streaks and twins spots. Comparing diffraction patterns taken from just the template (with the SiO_2 layer also probed), the template and some of the MBE grown layer, and just the MBE grown layer, it appeared that epitaxy on the template layer could have occurred at some locations, but not uniformly. In the areas with possible epitaxy on the template layer, the preferred orientation of the 3 μm layer was <111> in cross-section, with dislocations and some polycrystalline spots in the diffraction pattern. In a region with many twins and a strong polycrystalline contribution to the diffraction pattern of the 3 μm layer, the diffraction pattern showed polycrystalline grains at the interface between the template and MBE grown layer. Polycrystalline silicon grown at 600 to 650 °C on an amorphous substrate will exhibit columnar grains with sizes of 0.03-0.3 μm, depending on the film thickness, and shows a <110> preferred orientation [35]. Therefore, that epitaxial growth from the polycrystalline template did not occur for most of the layer where there were submicron sized grains, and only in select regions that had 3 μm large grains.

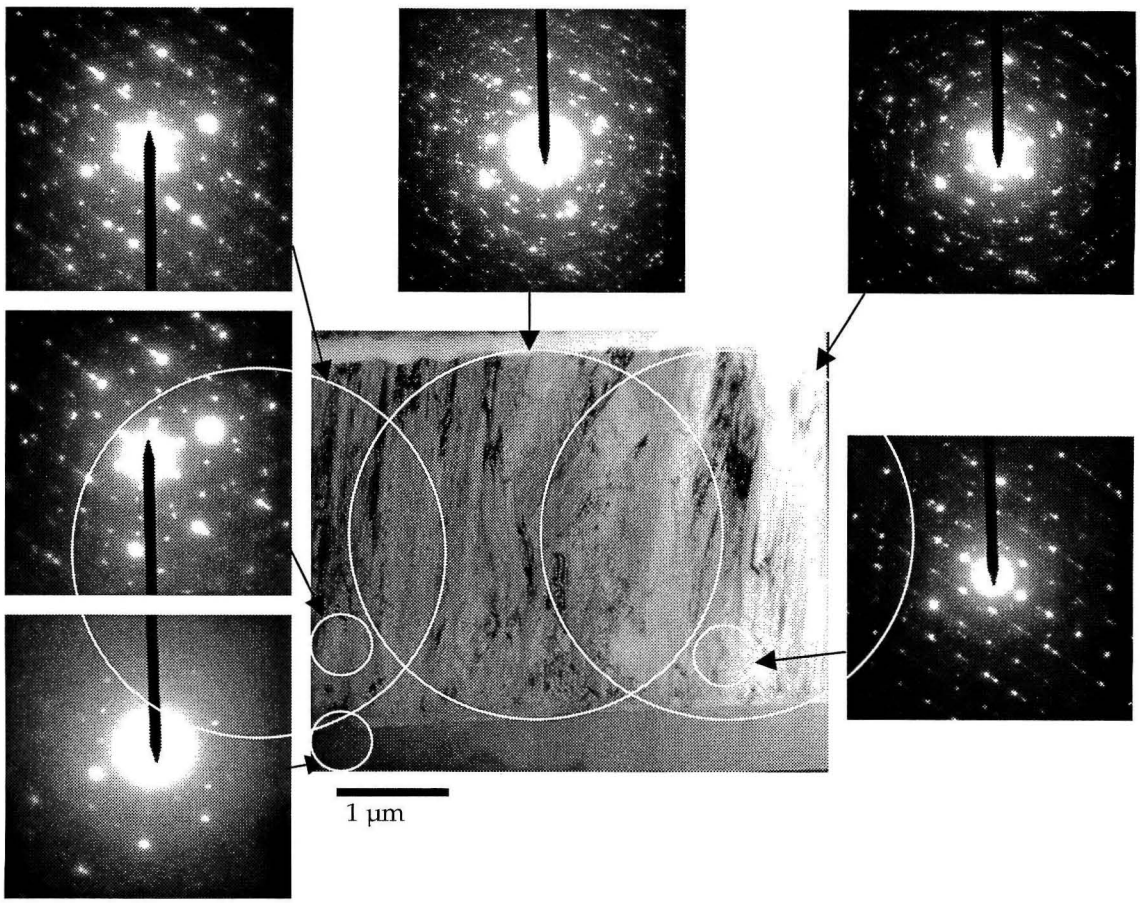

Figure 4.9. Cross sectional TEM image of the 3 micron thick silicon layer grown by MBE. Selected area diffraction patterns taken from the regions denoted by the white circles show both strongly polycrystalline regions and more single crystal regions. Dislocation streaks and twin spots are also apparent in the diffraction patterns.

Though the "epitaxial" layer in this case was not seeded uniformly by the template layer and would probably have benefited from better surface preparation, the regions of true epitaxial growth show that the resulting epitaxial layer is strained from the low angle grain boundaries. Any treatments to repair the low angle grain boundaries in the template layer before the epitaxial growth could result in a better quality, thick epitaxial layer.

Though the interface is not clean between the template and the thick MBE layer, it probably does not affect the diffusion of the Ni, which was probed in the other epitaxial layers grown. Using an XRF microprobe, which has sensitivity of 10^{15} cm^{-2} with a depth penetration of 70 μm, the Ni distribution was scanned in the x-y direction. SIMS has a detection limit of 10^{15} cm^{-3}, and probed the Ni distribution in the z direction.

With XRF, no segregation of nickel was detected at the a-c interface or at grain boundaries. The detection limit is 10^{20} cm^{-3} for a 2×2 μm^2 spot size, which can detect a precipitate with 4×10^7 nickel atoms. From SIMS, the nickel diffused into the epitaxial layer with concentrations between 10^{16}-10^{17} cm^{-3}, which is higher than the solid solubility of nickel in c-Si. This suggests that the nickel resides in precipitates in the bulk or in crystallographic defects like grain boundaries. Besides nickel from the template layer, another source of the Ni is the macroscopic nickel silicide regions that remain after the nitric acid etch.

A simple calculation of diffusion length $L=\sqrt{Dt}$ shows that in 10 seconds, the Ni can migrate 100 μm in c-Si, and if we estimate the diffusion coefficient in a-Si to be ~5×10^{-9}, then the Ni will diffuse 2 μm in a-Si. This suggests that the anneals made in the vacuum tube furnace are unquenched and the Ni has time to migrate to a more favorable position as the solubility decreases during the cool down time. As it migrates, the Ni can get trapped in grain boundaries or other

crystallographic defects, or existing silicide particles. Therefore, the cooled sample cannot be taken to be an accurate reflection of the sample during growth.

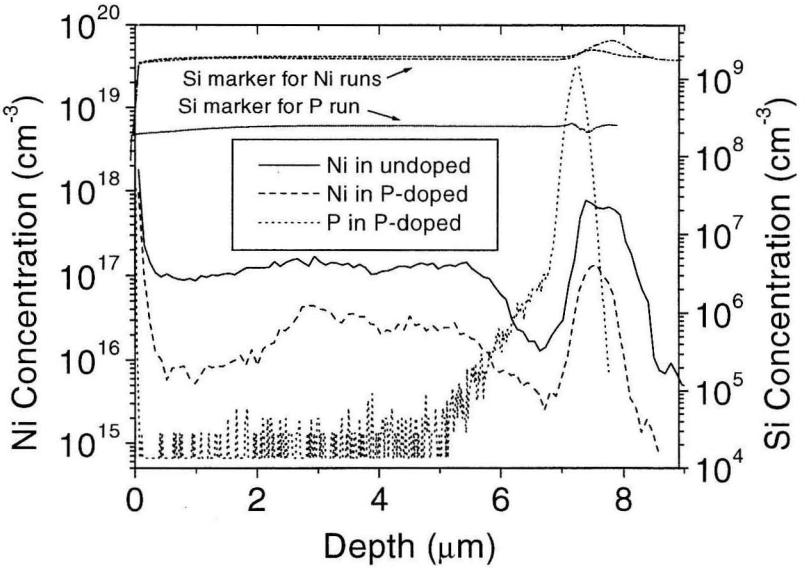

Figure 4.10. Nickel concentration probed by SIMS of a 6 μm thick epitaxial silicon layer grown on undoped and P-doped templates. The bump in the silicon marker denotes the SiO_2 layer below the template layer.

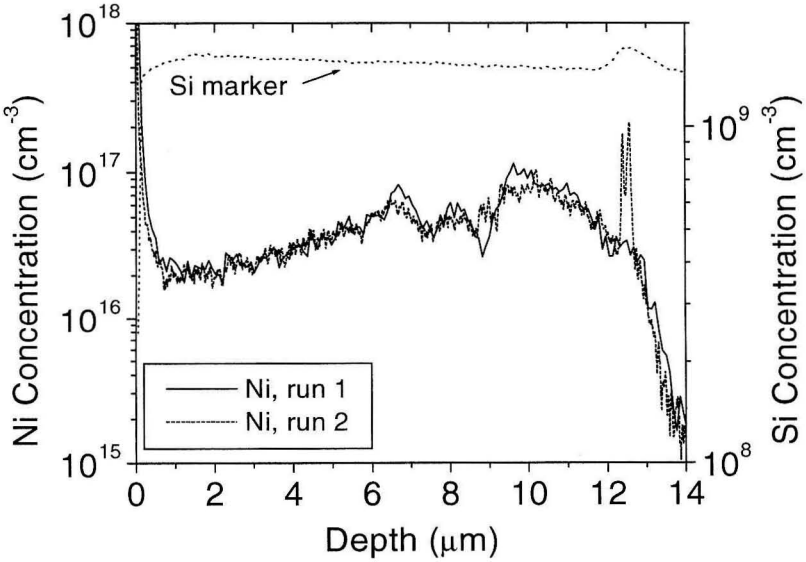

Figure 4.11. Nickel concentration probed by SIMS of a 12 μm thick epitaxial silicon layer grown on a P-doped template. The bump in the silicon marker denotes the SiO_2 layer below the template layer.

4.4 Ni patterns

Patterned silicon islands on silicon oxide were used as test structures to characterize the crystallization process, as seen in Figure 4.12. 75 nm thick amorphous silicon was deposited by plasma-enhanced chemical vapor deposition on a 1000 nm thick thermal oxide on a silicon wafer. Photolithography and wet etching with a 1:20:40 HF, HNO_3 and H_2O solution defined a-Si islands on the SiO_2. Nucleation seed regions were formed by ion-implantation of 40 keV Ni into photolithographically defined seed regions. Three doses were used: 5×10^{14} cm^{-2}, 5×10^{15} cm^{-2}, and 5×10^{16} cm^{-2}, with an average concentration of 6.7×10^{19} cm^{-3}, 6.7×10^{20} cm^{-3}, 6.7×10^{21} cm^{-3}, respectively.

The crystallization rate was determined from bar-shaped silicon islands with a 2 μm wide strip of Ni implantation. The results are plotted in Figure 4.13. For each temperature, the growth rate of the lowest dose was about a half of the growth rate for the other two doses. The two highest doses, despite having an order of magnitude difference in nickel concentration, had the same growth rate, which suggests that the nickel content in the seed regions had saturated, and that the growth rate was not dependent on nickel availability.

In a separate experiment, these structures were annealed for 30 minutes, 1 hour, and 2 hours at 600 °C. The crystallization rate and the morphology of the growth front depended on the implant dose and the area of the silicon island. As seen in Figure 4.14, for a given implant dose of 5×10^{16} cm^{-2} and anneal time, the

crystallized area depends on the total area. This dependence results from the difference in the nickel distribution for different sized island. At a given distance from the nucleation seed, smaller structures have a higher concentration in the a-Si than larger structures. For a large enough structure (the 25×25 μm^2 island in Figure 4.14), some critical concentration is not achieved and no long range crystal growth occurs. In Figure 4.15, for a given structure and anneal time and temperature, the difference due to implant dose are highlighted. The sample with the highest dose of 5×10^{16} cm^{-2} was almost fully crystallized. The sample with the dose of 5×10^{15} cm^{-2} was densely crystallized, but at a slower rate than the highest dose. The 5×10^{14} cm^{-2} dose appeared to have a similar crystal fraction as the previous dose but has many amorphous pockets that will presumably crystallized much slower by conventional SPE.

A schematic of a model that may explain the observations is shown in Figure 4.16. Ni distribution is plotted against distance at different stages of crystal growth. Initially, Ni diffuses from the seed region into the a-Si, until the Ni concentration reaches a critical concentration that enhances Si diffusion. The Si atoms that diffuse from the a-Si can grow epitaxially on the Ni silicide to form c-Si. Steady state growth occurs if the Ni concentration is maintained above the critical value; then crystal growth limited by Si diffusion. If the Ni concentration cannot be maintained above the critical value, then crystal growth is limited by Ni diffusion into a-Si, which may be the case for patterns with larger areas.

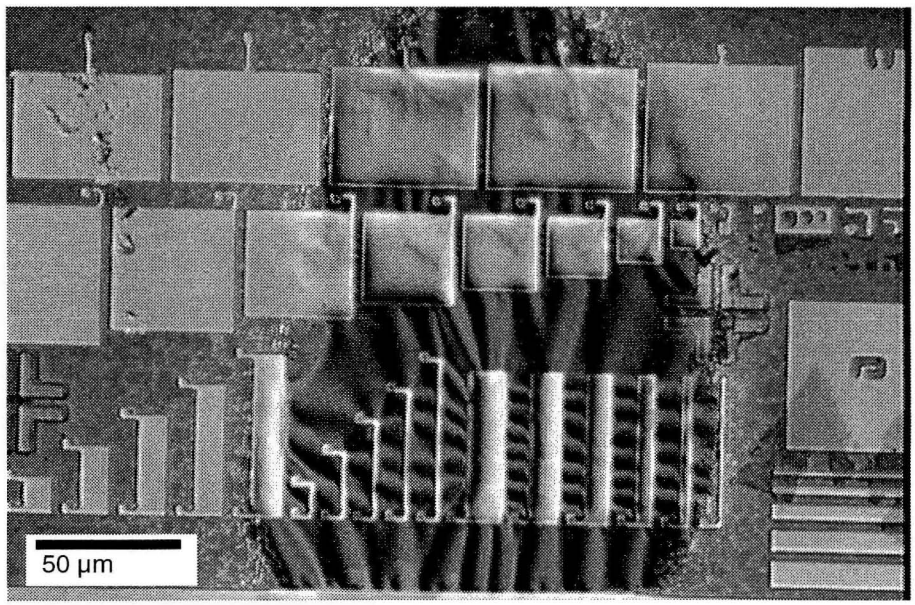

Figure 4.12. Optical image of photolithographically defined silicon islands on SiO_2 layer. Nickel was implanted into the ends of the protrusions from some of the structures.

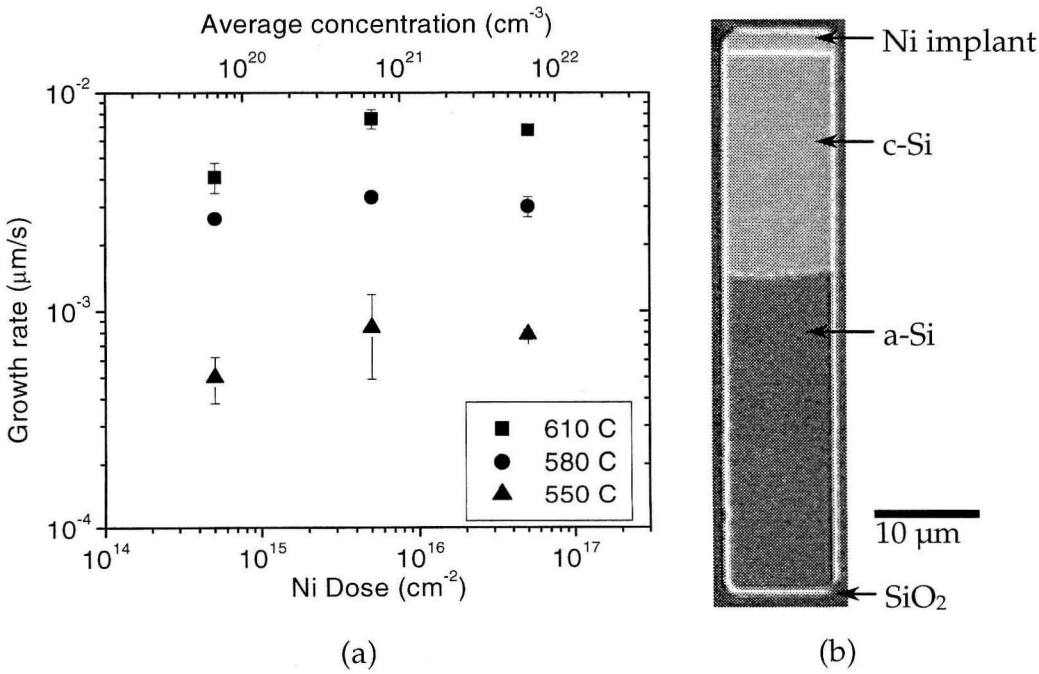

Figure 4.13. (a) Growth rate of Ni-mediated crystallization for (b) a rectangular silicon island on SiO_2. The growth rate is compared to Ni implantation dose and annealing temperature.

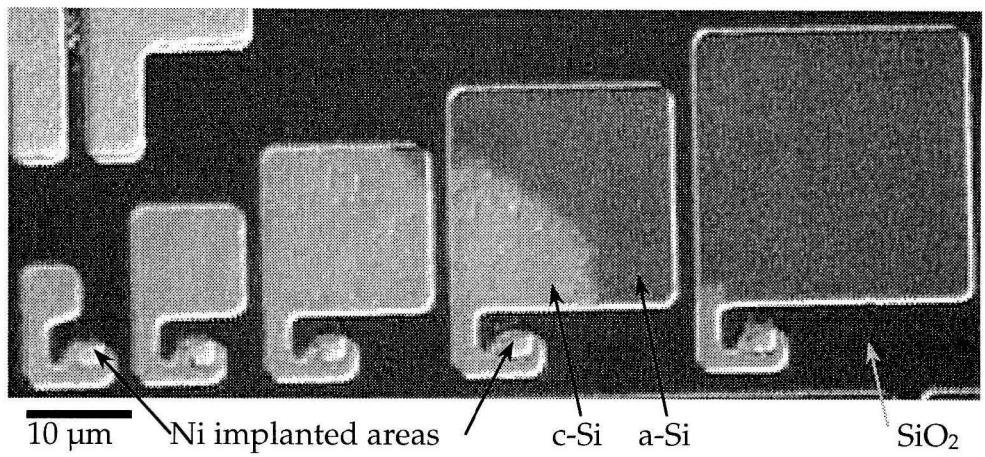

Figure 4.14. Patterned silicon on oxide with Ni dots (dose of 5×10^{16} cm^{-2}) were anneal for 2 hours. The crystallized area depends on the total area of the silicon pattern.

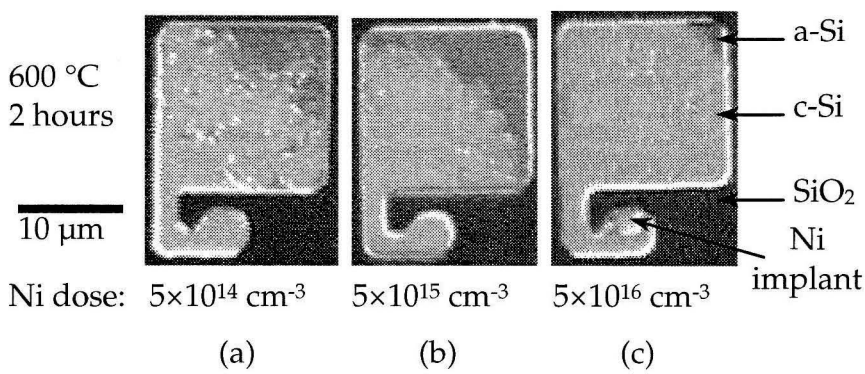

Figure 4.15. Optical images of patterned silicon on oxide with nickel implanted seeds with doses of (a) 5×10^{14} cm^{-3}, (b) 5×10^{15} cm^{-3}, and (c) 5×10^{16} cm^{-3}. Only the implanted region in the 5×10^{16} cm^{-3} case is visible. These samples were annealed at 600 °C for 2 hours. Notice the difference in the crystallization front.

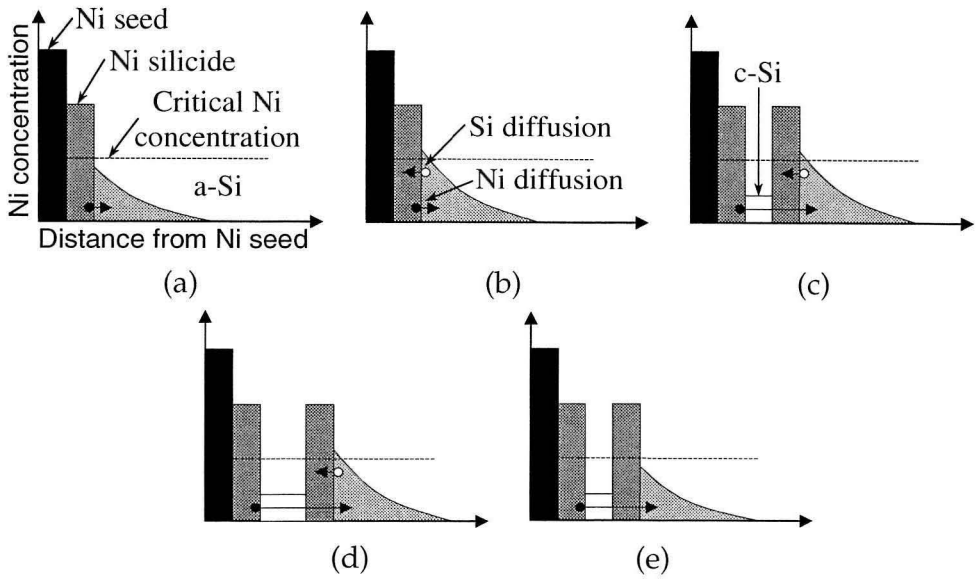

Figure 4.16. Schematic of proposed Ni distribution at different stages of crystal growth. (a) Initially, Ni diffuses from the seed region into the a-Si, until (b) the Ni concentration reaches a critical concentration that enhances Si diffusion. (c) The Si atoms form c-Si, with (d) steady state growth occurring if the Ni concentration is maintained above the critical value, with crystal growth limited by Si diffusion. (e) If the Ni concentration cannot be maintained above the critical value, then crystal growth is limited by Ni diffusion into a-Si.

4.5 Ni diffusion coefficient and solubility in silicon

Ni is a fast interstitial diffuser in c-Si, whose diffusion and solubility in c-Si has been characterized. The low temperature extension of the diffusion coefficient is 1×10^{-5} cm^2/s and the solubility of Ni is 3×10^{14} cm^{-3} in c-Si at 600 °C [36], the approximate temperature of most of our anneals. However, no

determination of the Ni diffusion coefficient or solubility in a-Si has been found in the literature. Estimates made on these values were extrapolated from what is known of other fast diffusers in a-Si.

The presence of defects in a-Si decreases the diffusion coefficient orders of magnitude from that of c-Si for fast diffusers in Si like Au, Ag, Cu, and Pd [27]. For example, Cu, which is an interstitial diffuser like Ni, has extrapolated diffusion coefficients of 2×10^{-5} cm^2/s in c-Si [36], and 6×10^{-9} cm^2/s in a-Si [37] at 600 °C. This factor of 3×10^{-4} was used to estimate the diffusion constant of Ni in a-Si to be 3×10^{-9} cm^2/s. An attempt at studying the diffusion of Ni in a-Si was made by Coffa *et al.* [37], but at the peak concentration of 0.02 at. % (1×10^{19} cm^{-3}) needed for detection by Rutherford backscattering spectroscopy, Ni was not observed to have diffused after the one hour, 500 °C anneal. They concluded that the lack of Ni diffusion does not suggest that Ni is not a fast diffuser in a-Si, but since the Ni solubility in c-Si is lower than Cu by an order of magnitude at 500 °C, that the Ni possibly precipitated. Though the study does not give information on the diffusion coefficient of Ni in a-Si, it does suggest that the nickel concentration used in the experiment, 1×10^{19} cm^{-3}, is an upper bound for the solubility of Ni in a-Si at 500 °C.

The solubility of fast diffusers in a-Si is estimated to be at least 6 orders of magnitude larger than in c-Si, and has been established for some fast diffusers, but not Ni directly [27]. The Ni solubility in c-Si is ~1.5×10^{13} cm^{-3} at 500 °C, which

is approximately is a six orders of magnitude less than the concentration used by Coffa *et al.*, which is consistent with the above assertion. All estimates of the solubility of Ni in a-Si will be extrapolated as 10^6 times the value in c-Si.

Using the one-dimensional, time dependent diffusion equation, $\frac{dC}{dt} = D\frac{d^2C}{dx^2}$, Ni distributions were calculated in Matlab for various times and lengths for a-Si and c-Si (see Figure 4.17). This calculation confirmed that for a given length from the nickel, the concentration will be higher in smaller structures. Also, while it takes over 2 hours for the nickel concentration to approach 100% in a 50 μm a-Si feature, the nickel reaches a uniform concentration in crystalline silicon within 10 seconds.

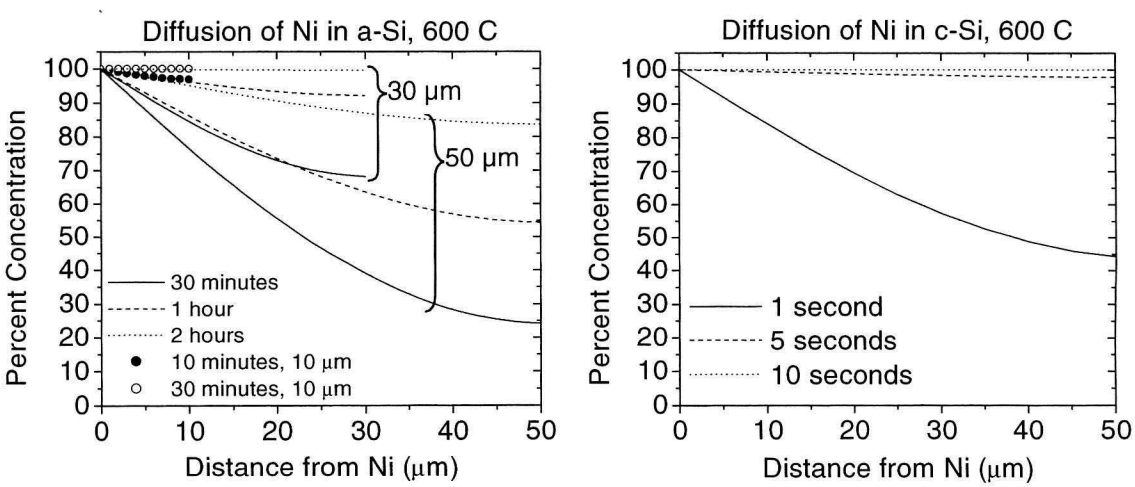

Figure 4.17. Calculated nickel distribution after 600 °C anneals over 50 μm for (a) amorphous silicon (diffusion coefficient of 3×10^{-9} cm^2/s) and (b) crystalline silicon, (diffusion coefficient of 10^{-5} cm^2/s. The one-dimensional, time-dependent diffusion equation was used.

4.6 X-ray fluorescence microprobe

The x-ray fluorescence (XRF) microprobe at Lawrence Berkeley National Laboratory (see Appendix D for more details) offers the unique ability to detect Ni at levels below the detection limits of common analysis techniques. By determining where the Ni resides in the samples, as well as concentration, we can learn more about the crystallization process and whether using Ni-induced crystallization is feasible for photovoltaic applications.

The detection limit of Fe in the XRF is ~1×10^{15} cm^{-2}. Since the atomic number of Ni and Fe are similar, nickel will have a similar sensitivity. The structure of the sample determines the minimum concentration that can be detected. Assuming a detection limit of 1×10^{15} cm^{-2} and a uniform Ni concentration down to the penetration depth of 70 μm, the absolute minimum concentration that can be detected is 1.4×10^{17} cm^{-3}. Since the solubility of Ni in c-Si [36] at 600 °C is 3×10^{14} cm^{-3}, dissolved Ni in the crystallized region will not be detected. However, with a estimated solubility limit of 3×10^{20} cm^{-3} in a-Si at 600 °C, it may be possible to see dissolved Ni in a-Si. Also, if the Ni is trapped in local hotspots, like silicides or grain boundaries, the local concentration may be high enough to be detectable.

4.6.1 Experiment

In samples nucleated by Ni particles, XRF was used to look at the possibility of Ni segregation at the crystallization front and of Ni at the grain boundary between two crystals with different Ni nuclei. Ni was also studied in a sample with a 12 μm thick epitaxial layer grown on a P-doped silicon template. Cross sections were probed to see if there were any lateral spatial inhomogeneities, a sign that there was metal precipitation at grain boundaries, or that the silicides that aided crystallization were locked inside the crystals. Also, photolithographically patterned films with Ni nucleation areas implanted with a dose of 5×10^{16} cm^{-2} and annealed at 600 °C were studied.

What concentrations can we expect to see in these samples with the XRF microprobe? Recall that the detection limit for Ni for the x-ray fluorescence microprobe is approximately 1×10^{15} cm^{-2}, and we already determined that Ni dissolved in c-Si cannot be seen. The minimum concentration that can be detected in a 75 nm thick layer (e.g., patterned Si sample) is 1.3×10^{20} cm^{-3}, while in a 100 nm thick layer (e.g., Ni particle nucleated template) it is 1×10^{20} cm^{-3}, and as was stated before, in a 70 μm layer (e.g., cross-sectional samples) it is 1.4×10^{17} cm^{-3}. Ni will be detected from the nucleation sites, and could be detected from silicide particles if they are big enough. A minimum dose of 1×10^{15} cm^{-2} times a 2×2 μm^2 spot size results in a minimum detectable number of Ni atoms of 4×10^{7} atoms. With a Ni density in $NiSi_2$ of 2.5×10^{22} cm^{-3}, this becomes a volume

of 1.6×10^{-15} cm^3. With a silicide thickness of 5 nm [22], and assuming the silicide spans the full thickness of a 100 nm thick film, a silicide at the end of a needle with a width of 3 μm could be detected. So, Ni collected at the grain boundaries or at the amorphous-crystalline growth interface may be seen.

In the thin film template layers nucleated by nickel particles, nickel was detected in the silicides, but the density of nickel around the particles was below the detection limit. Cross-sectional samples also did not show any lateral inhomogeneity, and instead, a uniform 1×10^{15} cm^{-3} concentration was observed. Either the sample tilt blurred the resolution, or over a 70 μm lateral spacing, the precipitates had a uniform distribution that was below the spatial resolution of the beam spot.

For the patterned Si samples, small structures that maximize the Ni concentration were studied. A 10×10 μm^2 square with two, 2 μm diameter implanted areas, and a 10×50 μm^2 bar with a 2×10 μm^2 implanted area at one end were analyzed. Both detected Ni outside of the implanted areas, but it was a homogeneous signal, even in the regions with just the oxide layer. In a sample annealed at 600 °C for an hour, a strong signal of 1×10^{16} cm^{-2} was seen in the implanted regions, and the background Ni dose was 4×10^{15} cm^{-2}. The dose is above that of the maximum dissolved Ni concentration, which suggests that the signal comes from a uniform distribution of Ni precipitates.

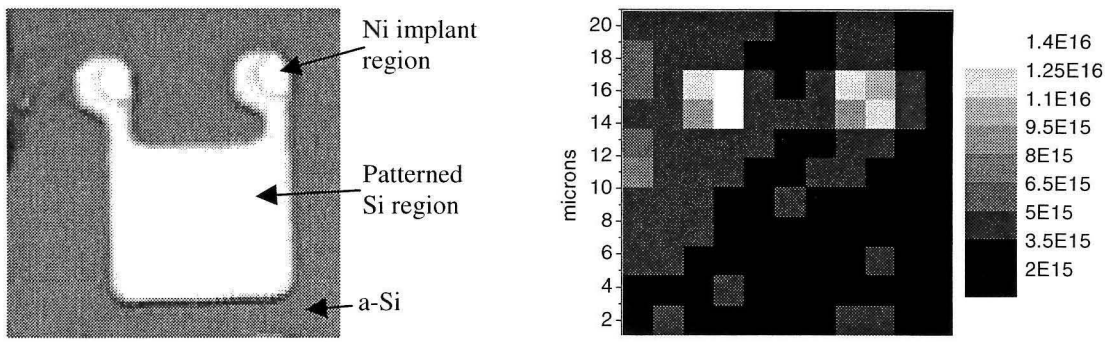

(a) (b)

Figure 4.18. (a) Optical image, and (b) x-ray fluorescence map of Ni dose, of a patterned Si structure with Ni implanted in 2 μm diameter seed regions with dose of 5×10^{16} cm^{-2}. This sample was annealed at 600 °C for an hour, and the Si region is fully recrystallized.

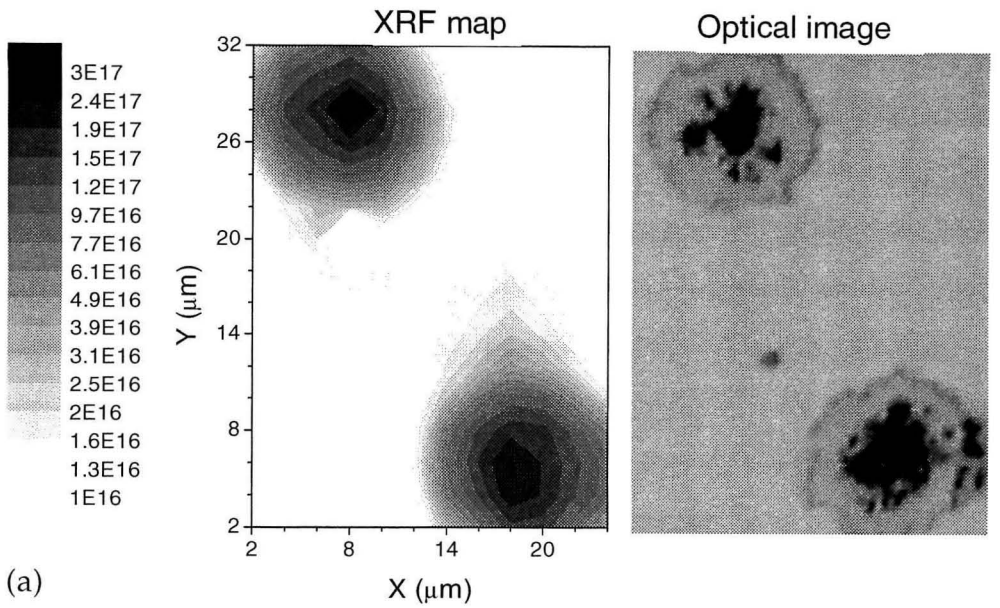

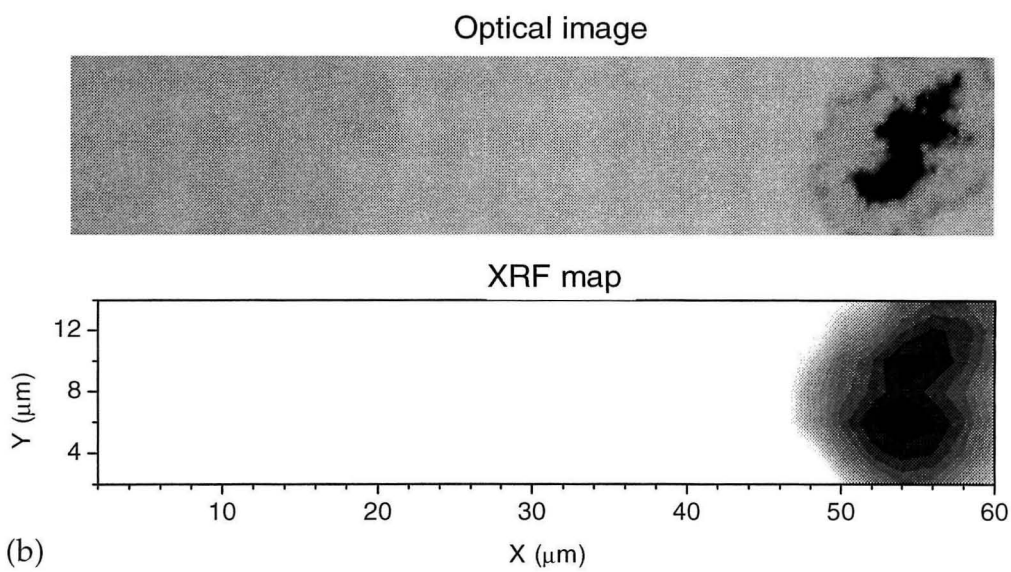

Figure 4.19. X-ray fluorescence microprobe results compared to optical microscope. There was no nickel that was detected at the amorphous-crystal interface, or at the boundary of two grains.

4.7 Conclusions

Nickel-nucleated lateral solid-phase epitaxy was achieved by nickel particles applied by a nickel colloidal "ink." The amorphous silicon layer fully crystallized before the onset of random nucleation, which each nickel particle seeding one grain, achieving grain sizes on order of tens of microns. Within each grain, however, were many low angle sub-grain boundaries that came from the needle-like crystal growth. Phosphorus doping increased the growth rate almost by a factor of two, and holds promise as a getter for nickel. In the template, the nickel was not observed to segregate at the crystallization front above the detection limit of XRF for a 100 nm thick layer, 10^{20} cm^{-3}.

Epitaxy on these layers resulted in strained columnar crystals with dislocations. Analysis of the nickel distribution in the epitaxial layers showed that nickel diffused into the microns thick layer to a concentration of 10^{16}-10^{17} cm^{-3}. This is above the solid solubility of nickel in c-Si, and suggests that nickel precipitated at grain boundaries.

Electrical characterization must be done before the feasibility of this technique can be decided, but the large grain sizes and shorter anneal times have great promise.

Chapter 5 Vacancies in solid-phase epitaxially grown Si

5.1 Introduction

Understanding the mechanisms of dopant-enhanced solid-phase Si crystallization is important in developing an optimum process for low-temperature solid-phase growth of large-grained polycrystalline silicon (poly-Si) thin films. It is well known that dopants like phosphorus and boron strongly influence the solid-phase crystallization [8], but despite extensive study, the mechanism for dopant-enhanced solid-phase epitaxy (SPE) at high doping concentrations ($\geq 10^{18}/cm^3$) is not well understood.

Kinetic models for the dopant enhancement of solid-phase crystallization have been proposed [15], and one Fermi level shifting model was discussed in Chapter 2. In this model, both neutral and charged defects (e.g., dangling bonds and vacancies) contribute to the amorphous-to-crystalline silicon conversion. The role of dopants is related to the Fermi level - with the addition of dopants, the Fermi level shifts, increasing the population of a certain, but as yet unspecified, charged defect, and thereby enhancing the growth rate. There is no discussion, however, on how the dopants interact directly with the defects. *Stable impurity-*

vacancy complexes could increase the vacancy population and affect the growth rate. The SPE rate, however, has not been correlated with direct measurements of the concentration of any point defects that could enhance the SPE rate.

The goal of this work is to compare doping effects on SPE with information about vacancies taken from positron annihilation spectroscopy (PAS) [38]. PAS is an analysis technique that is sensitive to open volume defects. Undoped and doped amorphous silicon (a-Si) on Si (001) samples were vacuum annealed. The amorphous-crystal interface was stopped at various depths, providing snapshots of the SPE process. These samples were studied with PAS to investigate the vacancy population and to identify the impurity-defect complexes.

5.2 Experiment

Samples were designed to have an amorphous silicon (a-Si) layer atop a crystalline silicon (c-Si) substrate, so that the amorphous layer recrystallized by vertical solid-phase epitaxy. The cases studied were undoped, B-doped, P-doped, and P&B-doped. The samples were processed by ion implantation, since it produces amorphous material with lower oxygen content than deposition methods, and keeps the a-Si and c-Si interface clean. The doping profile was graded to probe a range of doping concentrations, which was easily accomplished by a single energy implantation of dopant atoms.

5.2.1 Ion implantation

Float-zone (FZ) Si wafers (<100>, p-type, 200-300 Ω-cm) were amorphized by ion implantation of ^{29}Si at L-N_2 temperatures. ^{29}Si was used to prevent CO and N_2 contamination generated by m/e=28 implantation. Two implant energies, 70 keV (fluence of 2×10^{15} at/cm^2, current of 5 μA) and 200 keV (fluence of 6×10^{15} at/cm^2, current of 12-14 μA), were necessary to amorphize a 300 nm surface layer. The doses were determined from the damage profile for each energy given by the Monte Carlo simulation Transport of Ions in Matter (TRIM), such that the damage was above the amorphization threshold of 2×10^{15} vacancies/angstrom for the surface layer. The dopants were implanted at room temperature, with boron implanted at 72 keV to a fluence of 1.2×10^{14} at/cm^2 with a current of 50 μA, and phosphorus implanted at 200 keV to a fluence of 1.3×10^{14} at/cm^2 with a current of 165 μA. All implantations were done by IICO. The native oxide was not removed from the Si wafers prior to the implantations.

5.2.2 Growth rate measurements

The samples were vacuum annealed (~10^{-6} torr) to recrystallize the a-Si layer by SPE. Growth was monitored by time-resolved reflectivity (TRR) (see Figure 5.1). A 670 nm diode laser is reflected from the surface of the sample and the reflectivity collected by a photodiode. As the growth front moved from deep in the layer toward the Si surface, the interference from the reflections from the

surface and the amorphous-crystalline interface fluctuated between constructive and destructive, resulting in an oscillating signal. This oscillating signal is coupled with the Si absorption envelope, resulting in a curve that starts at the reflectivity value for a-Si, then oscillates with larger and larger amplitude, until the interface reaches the surface and the reflectivity is that of c-Si. In general, the growth distance z that the interface has moved in a cycle of oscillation is $\lambda / 2n_{a-Si}$; in this case, where λ = 670 nm and n_{a-Si} = 4.83, the cycle corresponded to 69 nm. Anneals were stopped at depths that correspond to the extrema of the TRR signal, in particular, at 35 nm, 69 nm, 138 nm, and 207 nm from the surface.

The samples were annealed at 600 °C on a hot stage consisting of a carbon platen set above a carbon heater. Temperature was calibrated using a thermocouple wafer. Final temperature was reached in 5 minutes, and was stable to a degree, as measured by the thermocouple wafer placed at the center of the platen. The anneals were stopped by turning off the power to the carbon heater and letting the sample cool with the heater. The heater cooled to 300 °C in approximately 7 min.

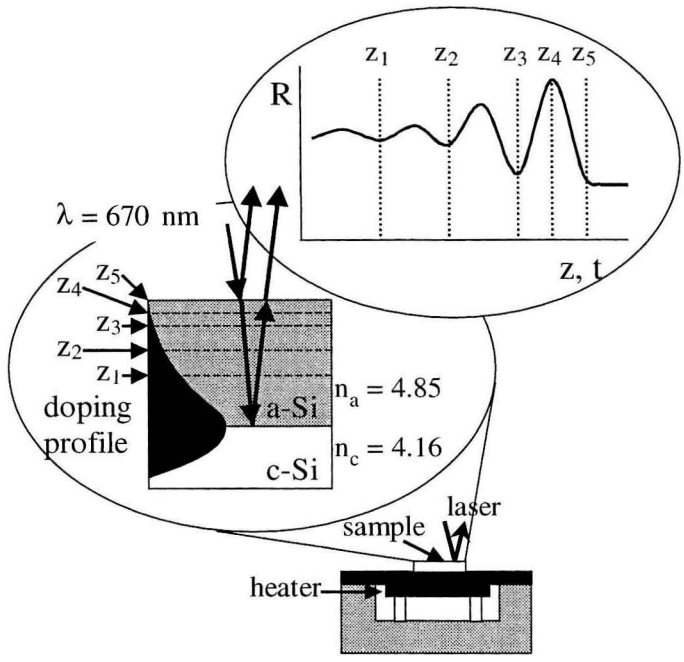

Figure 5.1. The experimental set-up of the anneal. Samples were vacuum annealed on a hot stage at 600 °C, with a 670 nm diode laser incident to monitor the growth rate with TRR. The interface was halted at depths corresponding to extrema in the reflectivity data (z_1, z_2, ,z_3, z_4, z_5).

5.3 Sample characterization by TRR, SIMS and spreading resistance

From the TRR data from fully recrystallized samples, the velocity versus interface depth information was calculated. A gradual retardation of the growth rate was observed in all the samples, as well as a sudden drop in velocity at the surface. For the doped samples, a drop in the velocity as the a-c interface moves through the decreasing dopant concentration is expected, but since the undoped sample exhibited the same decrease in velocity, these retardations are attributed

to hydrogen and oxygen contamination which have been observed to retard SPE, and not from the dopant depth profile. The source of the impurities could be recoil implantation [39].

The P-doped sample had the fastest growth rate, and was the only sample to show a growth enhancement throughout the layer. Small enhancements in the B-doped and P&B-doped samples were observed only around the lower surface of the a-Si layer, where the dopant concentration is close to 10^{19} cm^{-3} and it is more removed from impurities from the surface. To make sure that the doping concentrations were high enough to shift the Fermi level at the anneal temperature, carrier concentrations were calculated for 600 °C, using the law of mass action and considering the temperature dependence of the band gap and density of states [1]. The carrier concentration was found to be extrinsic throughout the sample, and the intrinsic carrier concentration was 1.7×10^{17} cm^{-3}. According to the Fermi level shifting model, an enhancement is expected.

Samples were later annealed in a vacuum tube furnace, a more isotropic heat source, to see if the hot plate introduced unanticipated temperature nonuniformity. Samples were held vertically with a slotted Mycor boat, and the diode laser light shone through an optical flat into the furnace. The growth rate dependence on depth was similar (see Figure 5.2), but the absolute rate was different. Given a larger confidence in the temperature calibration for the furnace, the temperature of the hot plate was estimated to be 568 °C, assuming

an activation energy of 2.7 eV for the Arrhenius behavior of the growth rate (see Section 2.2).

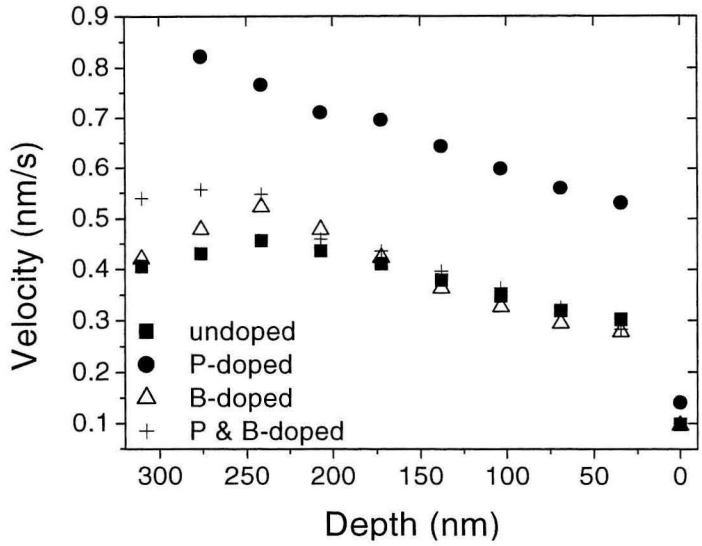

Figure 5.2. Solid-phase epitaxy rate of undoped, B-doped, P-doped, and P&B-doped Si, annealed at 600 °C in a vacuum furnace.

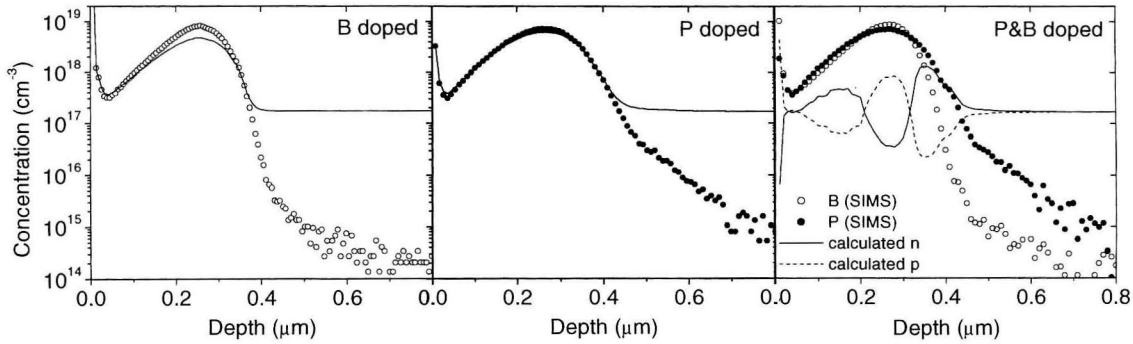

Figure 5.3. Carrier concentrations at 600 °C for B-doped, P-doped, and P&B-doped Si, calculated from dopant concentrations obtained from SIMS. The law of mass action and the temperature dependence of the band gap and density of states were considered [1].

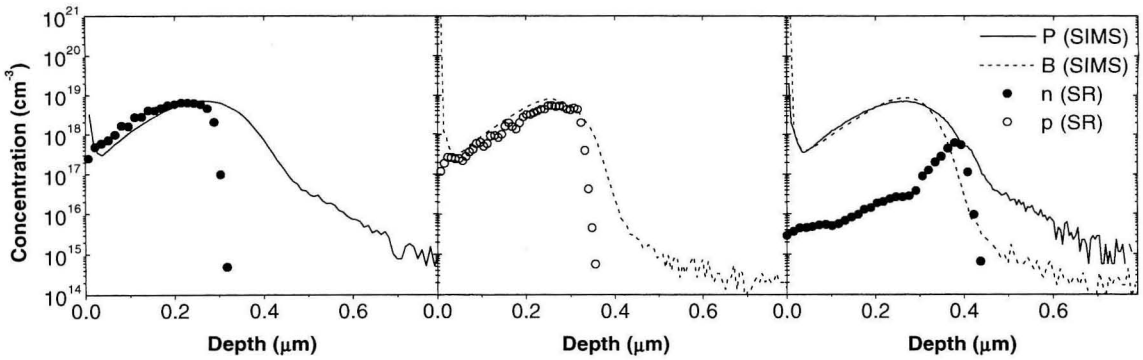

Figure 5.4. Spreading resistance and SIMS data for the fully crystallized (a) P-doped sample (P dose, 1.3×10^{14} at/cm^2; peak concentration, 7×10^{18} at/cm^3), (b) B-doped sample, (B dose, 1.2×10^{14} at/cm^2; peak concentration, 7×10^{18} at/cm^3), and (c) P&B-doped sample, (P and B specifications same as above), annealed at 600°C.

The fully recrystallized Si samples were analyzed by secondary ion mass spectroscopy (SIMS) by Charles Evans and Associates, and spreading resistance by Solecon. SIMS gives the impurity concentration, and spreading resistance gives the carrier concentration. The elements probed with SIMS were carbon, oxygen, and relevant dopants.

Figure 5.4 shows the SIMS and SR measurements made on fully recrystallized P-doped and P&B-doped samples. The peak concentrations of phosphorus and n-type carriers coincide in the P-doped Si case. The uncertainty in the phosphorus concentration is ±15%, and the uncertainty in the n-type carrier concentration is ±20%, so the phosphorus implant was activated within an error of 15-20%. The shift in the peak with depth between these two measurement techniques is attributed to measurement error, though quoted errors in depth calibration for both techniques is ±3%. In the B-doped Si case, the concentration

of p-type carriers is 65% the concentration of boron. The uncertainty in the boron concentration is ±6%, and the uncertainty in the p-type carrier concentration is ±20%. In the P&B-doped sample, the carrier concentration has features that result from nonidentical implant profiles and is 2 orders of magnitude less than the dopant profiles but not to intrinsic levels, which is explained by the partial activation of the boron. End of range damage from ion implantation can be seen as a drop off of the carrier concentration.

From SIMS, the oxygen concentration is ~10^{18} cm^{-3} near the surface and decreases with depth, with a low bump suggestive of the amorphizing implantation [39]. Since the samples had a native oxide during implantation, it is possible that the oxygen was recoil implanted. TRIM simulations established that oxygen is recoil implanted from a 20 nm thick native oxide layer into the sample, when treated with the implant schedule we used. The little oxygen peak seen in the undoped and B-doped samples around 350 nm is attributed to oxygen diffusion to the high-defect EOR region, during sample storage, since these samples were analyzed six months after the P-doped and P&B-doped samples.

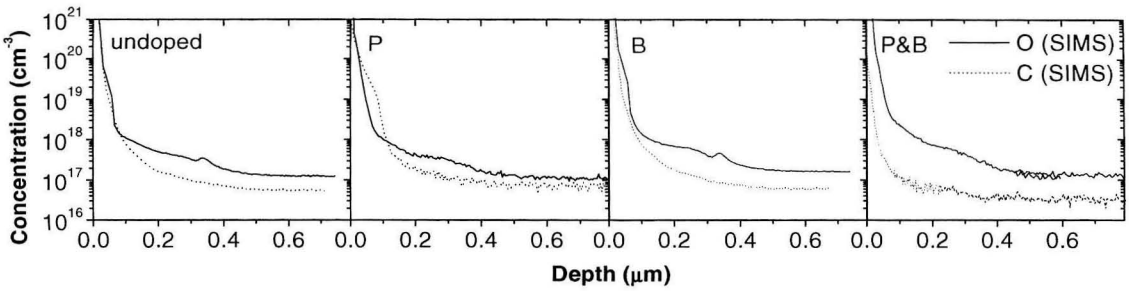

Figure 5.5. Oxygen and carbon depth profiles in (a) undoped, (b) P-doped, (c) B-doped, and (d) P&B-doped samples by SIMS.

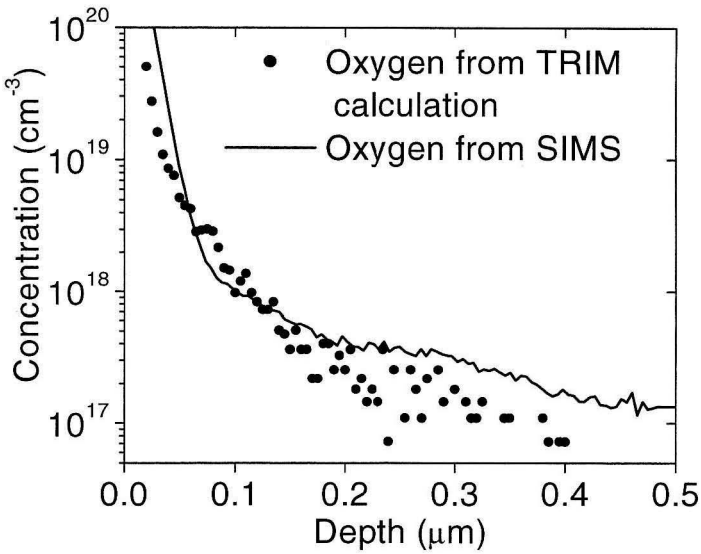

Figure 5.6. Oxygen concentration from SIMS analysis (line) compared to the calculated distribution of recoil implanted oxygen from a TRIM simulation (•) of our amorphization process, assuming a 5 nm thick surface oxide.

Cross-sectional TEM analysis showed that the amorphized layer had a thickness of 346 nm, as seen in Figure 5.7(a). Partially regrown undoped (Figure 5.7(b)) exhibited dislocations that originated from the rough as-implanted a-c interface. A 450 °C preanneal for 30 minutes would have smoothed the interface and prevented the formation of dislocations. The effect of the dislocations on the positron data is studied in Appendix I.

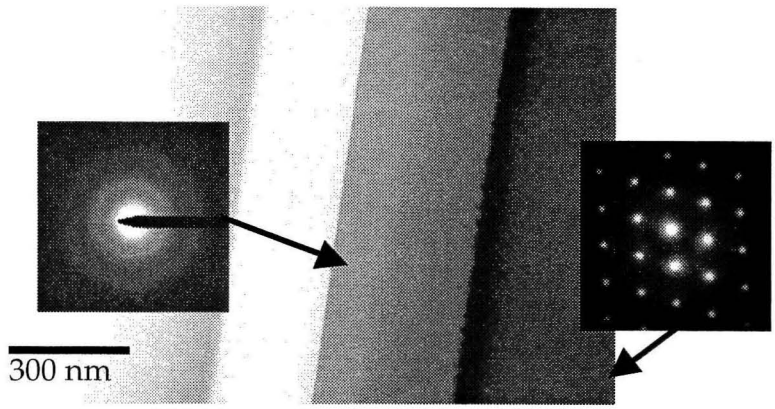

(a)

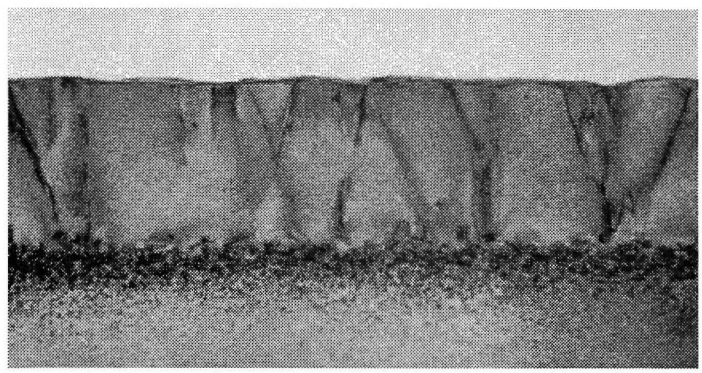

(b)

Figure 5.7. Cross-sectional TEM micrographs of (a) as implanted undoped Si, with selected area diffraction patterns inset, and (b) partially recrystallized undoped Si. Note the dislocations arising from the rough a-c interface.

5.4 Positron Annihilation Spectroscopy

Positron annihilation spectroscopy is the spectroscopy of the gamma rays that result from the annihilation of positrons introduced by a positron beam and electrons in the material of interest. Through the characterization of the statistical

distribution of energies of the gamma radiation, information can be determined about the state of annihilating electrons, and the defects in the material in turn.

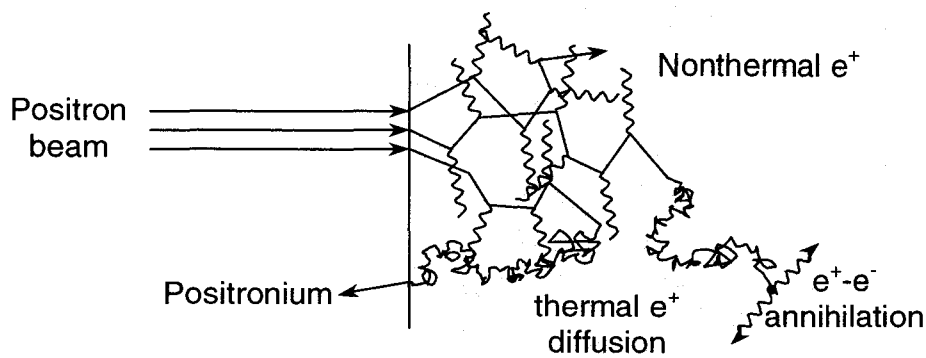

Figure 5.8. Schematic of the processes that occur between an incident positron beam and a solid.

An energetic incident positron thermalizes quickly within the target material (within 1-10 ps) and then diffuses through the sample, possibly getting trapped at a defect site, until it annihilates with electrons in the sample to produce two gamma rays with energies near the rest energy of an electron, 511 keV. The thermalized positron will interact electrostatically with the material, experiencing a strong repulsive force to ion cores and an attraction to open volume defects, which are local energy minima that can trap positrons. The spectra from positrons trapped at open volume defects differs from the spectra from positrons that annihilate while diffusing in the bulk, which makes this technique uniquely powerful in probing the population of open volume defects.

5.4.1 Interpretation of the annihilation peak and analysis techniques

The sum over all annihilations will result in an annihilation peak centered on the rest energy of an electron, 511 keV. Any deviation from 511 keV for a single photon is from a Doppler shift caused by the nonzero kinetic energy of the annihilating electron. Annihilations from valence and conduction electrons, which have low momentum, produce gamma rays with little shift from the peak at 511 keV, while core electrons, which have higher momentum, will shift the gamma ray energies away from 511 keV into the tails of the annihilation peak. Two line shape parameters extracted from the annihilation spectra reflect these two classes of electrons: the S parameter, which is the ratio of the counts centered at the peak maximum to the whole peak, and the W parameter, which is the ratio of the lower and higher energy tails of the peak to the whole peak. The S parameter reflects the number of annihilations from valence and conduction electrons, which is the most probable annihilation case for positrons in an open volume defect. The S and W parameters are often normalized to the S and W signal in the Si substrate, which highlights deviations from high quality, "defect-free" silicon. Mention of S and W parameters in this chapter will refer to the normalized quantity.

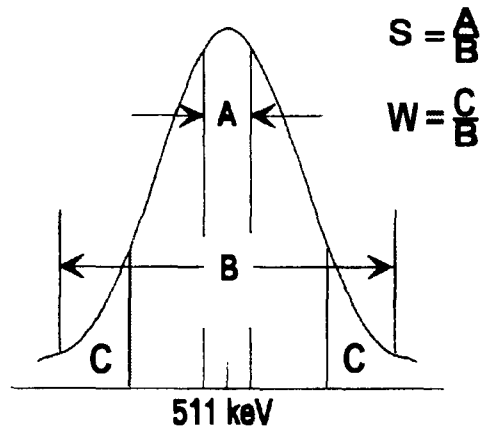

Figure 5.9. Parametrization of the 511 keV annihilation peak into S, the percent counts at the center of the peak, and W, the percent counts in the tails.

Using two synchronized detectors [40-42], the signal to noise ratio is improved by a factor of 100 to 1000. The high momentum signals can then be analyzed, and element specific momentum distributions resolved. Taking the ratio of counts versus momentum data of samples with different composition reveals characteristic peaks, since core electrons of different elements have distinct momenta. The location of these peaks can be predicted by theory calculations, though amplitude can vary by a factor of two [43,44].

A depth scan of the samples can be made by incrementing the energy of the positron beam in what is called a Doppler broadening experiment. This type of experiment will also be referred to as an energy scan. This is a standard method for analyzing samples, and the fitting program VEPFIT [45] is used to extract the S and positron diffusion length of different layers in the sample. S helps identify what type of defect it is, which the positron diffusion length is related to the

defect population. Material with more defects will have a shorter diffusion length than material with very few defects (see Figure 5.10). Unfortunately, the fits to the data are not unique. A number of pairs of S and positron diffusion lengths can fit the data, so it is important to independently determine the values of the parameters involved in the fit.

The diffusion length can be determined independently (of fitting the S versus energy data) from the positronium fraction, or R, versus energy data. Positronium exists only outside of the solid, and is detected only if a positron escapes the target from the surface. This quantity depends on the material that the positron must diffuse through, and the surface conditions. Scanned over energy, or similarly, increasing mean implant depth, the curvature of the data yields the diffusion length, as long as surface conditions do not change during a measurement. The diffusion length extracted only applies to the top layer.

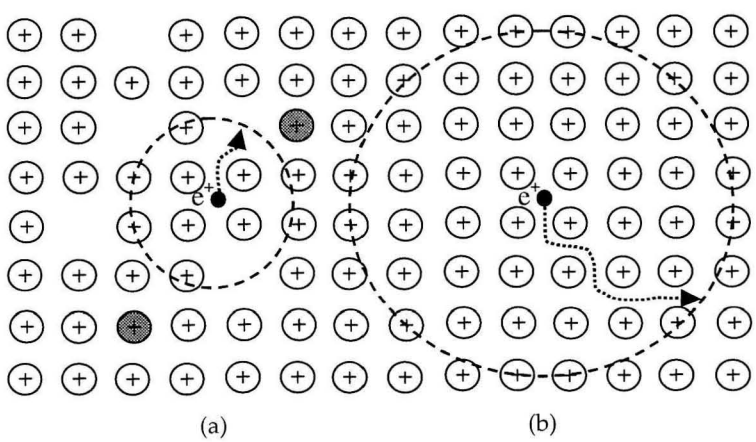

Figure 5.10. Schematic of atoms in a crystal lattice, with (a) high concentration of vacancies and low diffusion length and (b) a defect-free area with long diffusion length.

The diffusion length determined from the positronium fraction can then be inputted into VEPFIT to determine the S value of the layer, which reflects the type of defect that is dominating the positron signal. Alternatively, given a defect with known S value, a diffusion length can be extracted, and with the trapping rate of the defect, the defect concentration, C_d, can be estimated.

S values have been determined for some defects or materials. Divacancies in c-Si are 4.5% above the bulk value [46,47], and larger vacancy complexes in c-Si are 6.5% [46]. The S value for a-Si is ≥ 3% above the bulk silicon value with some cases as high as 6% [48], depending on the number of dangling bonds, vacancies or vacancy clusters n the material. Therefore, a-Si should have a normalized S parameter, S, of 1.03 and higher, divacancies have an S parameter of 1.045, and larger vacancy clusters have an S parameter of 1.065.

A way to visualize the data that highlights the different defects that the positrons are annihilating on is to plot S versus W. A particular defect state will have a characteristic S and W value, and as the different energies scan over the depths and between defect states, the data will trace a line. For example, in defect free Si, the data moves in straight line from the surface state, to the bulk value of S=W=1 (by definition). Any deviation from the line between the surface state and bulk state signifies the influence of another defect.

An alternate method of getting a depth profile of a sample is to progressively etch the surface of the sample, by sputtering [49] or chemical etch [47,50], and

analyze with the positron beam. This will give greater depth resolution of the sample, since deeper features can be accessed by lower energies, which have narrower implant profiles.

5.5 Experiment

5.5.1 Doppler broadening experiment

The samples prepared as described in Section 5.2 were analyzed by running energy scans to get a depth profile. Positron energies were scanned up to approximately 20 keV, which penetrates to a mean depth of 2 μm, and a data point was taken at 57 keV with a mean depth of 11 μm, to obtain the S value of the Si substrate. The data was normalized to the value of S at the high implant energy to obtain S, seen in Figure 5.11. The S versus energy data was fitted with VEPFIT, and the positronium fraction versus energy data and S versus W plots were analyzed.

From the Doppler broadening data (see Figure 5.11), several observations can be made. The decrease in normalized S after the initial anneal implies that some of the defects were annealed out, which correlates with the structural relaxation of ion implanted a-Si observed by other techniques like differential scanning calorimetry [51] and from changes in index of refraction [52].

The S versus W plot of undoped silicon (Figure 5.13) highlights the different defects seen at different depths. In particular, there are ranges of surface defects that are probably oxygen-vacancy complexes, EOR defects that are probably vacancy clusters, and bulk silicon.

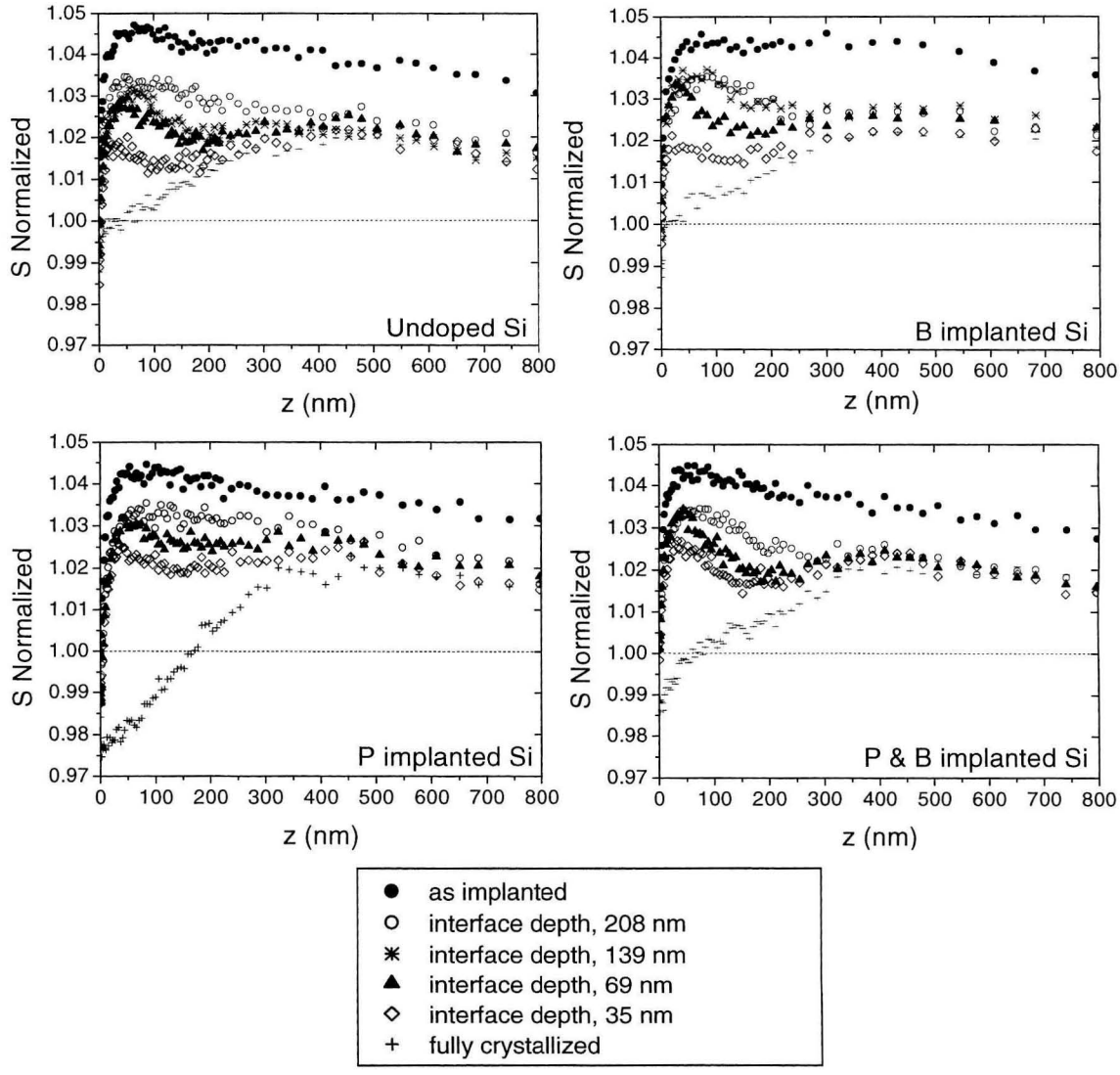

Figure 5.11. Positron annihilation spectroscopy (PAS) data for undoped, P-doped, and P&B-doped silicon samples. The different curves for each sample include an as-implanted sample (interface at 346 nm), annealing steps with the interface at depths given, a fully crystallized sample.

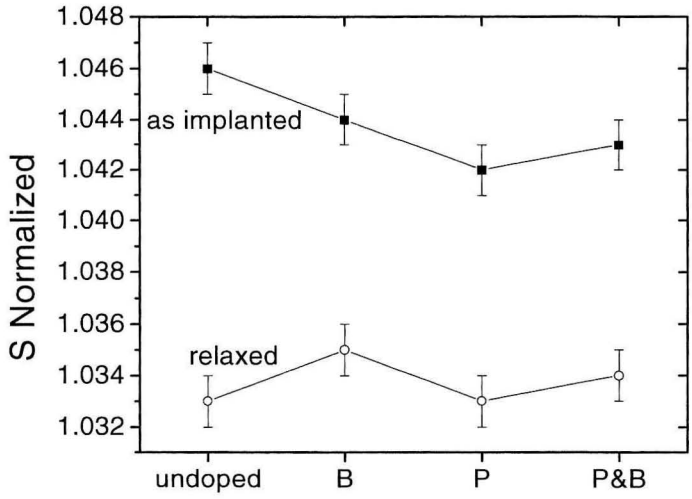

Figure 5.12. Summary of saturation S values for as-implanted and relaxed a-Si (after initial 600 °C anneal) in all doping cases. The S values for the a-Si layers are roughly the same. The as implanted doped samples are probably slightly relaxed, caused by the room temperature dopant implants.

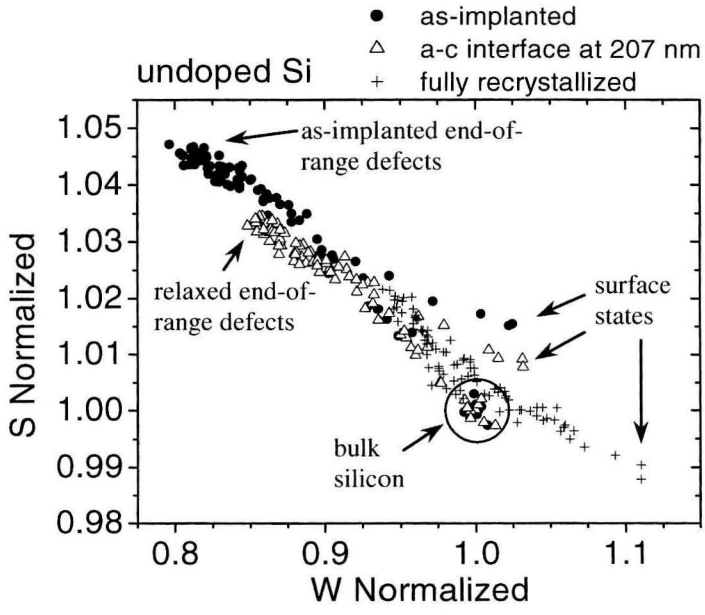

Figure 5.13. S versus W plot for the as-implanted, partially recrystallized, and fully recrystallized undoped silicon samples. The different defect signatures are labeled.

In S versus energy plots, the S value plateaus in thicker a-Si layers, which suggests that positron annihilation is saturated in those regions and the S measured at those energies reflects the S of the layer, rather than some linear combination of the a-Si and epitaxial layers. In Figure 5.12, the S of the as-implanted is compared to the S in the structurally relaxed a-Si. The S of the relaxed a-Si is constant at 1.03 within errors suggesting there is little influence of the dopants on the degree of structural relaxation in the a-Si. The S of the as-implanted doped samples is lower than the as-implanted undoped sample, which is possibly caused by local annealing during the room temperature dopant implants.

As explained previously, the S of a-Si is approximately 1.03, of epitaxial Si, approximately 1.00, and in the EOR region, 1.04-1.06 from divacancies and vacancy clusters. Therefore the energy scan of a four layer system of a-Si/recrystallized Si/EOR/Si substrate would have a peak near the surface, a dip as the positrons probed the epitaxial layer, then a deeper peak from the EOR damage, and then a gradual decrease towards the bulk Si value of one. The slopes of the changes between layers and the absolute value of S reflect the S of the layer and the positron diffusion length of that layer. Longer diffusion lengths result in more mixing of the signal and shallower slopes. There is also an effect on the slope from the implant profile; deeper interfaces will have shallower slopes from the broader implant profile.

In all doping cases, the value of S at the surface dips below one, probably from the recoil implanted oxygen. The EOR region stays constant through all anneals, the slight differences in S are most likely from the changing characteristics of the surface layers. The obvious differences are in the slope between the a-Si peak and the epitaxial Si trough, and the absolute value of the peaks and troughs. This could be from differences in both S and positron diffusion length in the epitaxial layer. The only way to quantify these differences is to fit the data with VEPFIT.

An attempt at fitting the data to a model of positron diffusion through the material (see Appendix G) with VEPFIT resulted in defect concentrations in the range of 10^{16}-10^{18} cm^{-3} for the epitaxial layer, depending on what S value was assumed. Further interpretation of the data could not be made – the confidence interval ranges over an order of magnitude. A trapping rate of 2×10^{15} s^{-1} was used, with values cited in the literature ranging over an order of magnitude [47].

5.5.2 Etch back experiment

In addition to modeling the Doppler broadening data by VEPFIT, the defect concentration can be estimated for a given positron beam energy from the S parameter by the equation, $C_d = \frac{C_b}{k_d \tau_b} \frac{S - S_b}{S_d - S}$, where C_d is the defect concentration, C_b the density of the bulk material, k_d the defect trapping rate, τ_b the bulk lifetime, S_b the bulk S value (= 1 for normalized S values), and S_d the S

value of the defect. This concentration is averaged over the depth probed for the positron energy. To get a defect depth profile, samples can be etched so that deeper layers are probed with lower energy positrons, which have better depth resolution. The samples were progressively etched by oxidizing and etching the oxide repeatedly. Positrons with the following energies were used: 0.25 keV to probe the 2 nm at the surface, 1keV which as a peak depth of 14 nm and a FWHM of 21 nm, and 2 keV which probes to a peak depth of 42 nm with a FWHM of 65 nm.

For each doping case, four samples were studied: as implanted, fully crystallized, and partially crystallized samples with the a-c interface at a depth of 207 nm and 138 nm. Samples were oxidized by an RCA solution (5:1:1 H_2O:H_2O_2:NH_4OH) for 5 minutes at 80 °C, which results in an oxide thickness of ~1 nm [53,54]. The samples were then HF dipped for 1 min to remove the oxide. This cycle was repeated 20 times for each data point.

The depth of the etch steps were determined by fitting energy scans of the fully recrystallized undoped sample at each etch step with VEPFIT, and extracting the depth of the recrystallized layer, assuming that everything else (S, diffusion length, thickness of EOR region) was constant. The fits gave an etch rate of 34 nm per step.

Regardless of the noise in the data, when compared to the Doppler broadening data, the etch-back data yields S values that are expected for the

layers. The S values for the a-Si layer were lower than the S values seen with the energy scans, which is attributed to further structural rearrangement at the surface. S values of 1.01 were seen in the epitaxial layers of undoped, B-doped, and P&B-doped silicon, which is due to residual defects and dislocations. For the P-doped case, S dipped to 0.99, due to the P-V complexes. These values were inputted into VEPFIT.

Defect concentration was calculated assuming that vacancy clusters were the dominant defect. This yielded concentrations with an order of magnitude of 10^{15} cm^{-3}, which are two orders of magnitude less than the defect concentration caluclated from the VEPFIT results. Since the calculation using S assumes only one defect, any additional defects in the layer could have skewed results.

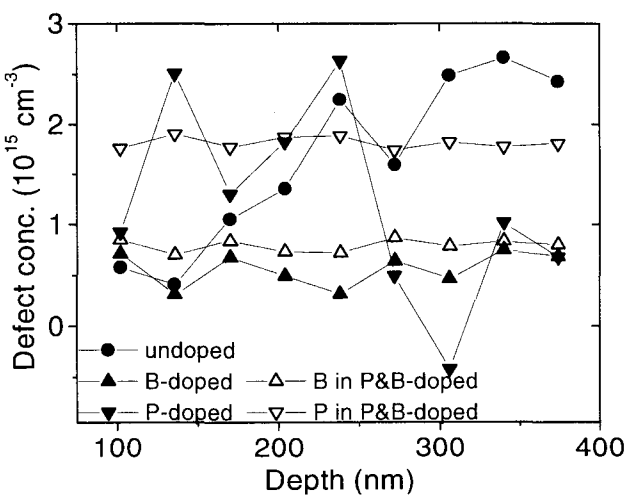

Figure 5.14. Calculated open volume defect concentration depth profile for undoped, P-doped, B-doped, and P&B-doped samples.

5.5.3 Two detector experiment

The two-detector technique reduces the noise low enough so that high momentum core electron contributions to the annihilation peak can be resolved. Since a large percentage of the positrons are trapped at open volume defects, this technique reflects the impurities in close proximity to open volume defects. This technique is not sensitive to the bonds, but only spatial proximity. The two-detector data for the fully recrystallized doped samples were normalized to the fully recrystallized undoped case. In both the P-doped and P&B-doped cases, a peak associated with phosphorus was observed [55]. This suggests that there are many phosphorus atoms next to vacancies, which points to a phosphorus-vacancy (P-V) complex, The peak in the co-doped sample was smaller, even though the phosphorus concentration was the same. Possibly the difference in Fermi level resulted in fewer negatively charged P-V defects. For the B-doped data, there was no strong peak associated with boron.

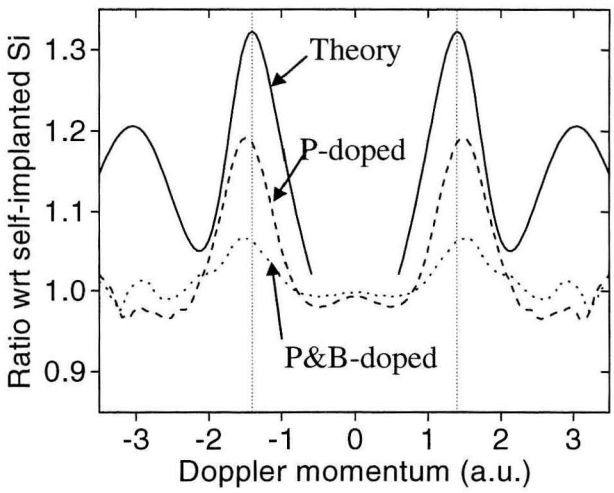

Figure 5.15. Momentum resolved PAS data for P-doped and P&B-doped Si samples, both divided by the undoped Si data. The resulting data exhibits peaks that correlate with theoretical calculations of P/Si, which suggests there are P-V complexes.

5.6 Conclusions

The interface velocity versus depth was calculated, and a slow retardation was observed for all samples, which was attributed to recoil-implanted oxygen, which is seen in the SIMS data, or hydrogen. TEM images showed that there were dislocations extending from the end of range damage. Defect concentrations of 10^{16}-10^{18} cm^{-3} were estimated from the energy scans. Progressive etching of a subset of the samples was achieved, and a defect concentration on order of 10^{15} cm^{-3} was estimated for all samples. The PAS data shows evidence for O-V complexes in all samples, P-V complexes in the P-doped samples, and vacancy clusters in the end of range region.

Chapter 6 Conclusions and Future Work

6.1 Selective nucleation and solid-phase epitaxy

Selective nucleation and solid-phase epitaxy offers a low temperature method to fabricate large grain, polycrystalline silicon on foreign substrates.

Undoped and highly doped amorphous silicon thin films were nucleated with nickel or indium and annealed at 600 °C. In nickel-nucleated samples, the amorphous silicon layer fully crystallized before the onset of random nucleation, achieving grain sizes on order of tens of microns. Within each grain, however, were many low angle, sub-grain boundaries that came from the needle-like crystal growth. Epitaxy on these layers resulted in strained columnar crystals with dislocations.

Indium nucleated crystallization proceeded by conventional solid-phase epitaxy. Undoped silicon had grain sizes of 1-2 μm. With doping, though there was enhancement of the growth rate, the grain size did not increase, since the incubation time correspondingly decreased. The exception was the phosphorus-doped silicon that had a maximum grain size of 10 μm. Though the crystal structure had many twin boundaries, solar cells made by solid-phase crystallization have achieved an efficiency of 8.6% [7]. Unfortunately, a setback

for this technique is the processing time of tens of hours, which is not industrially feasible.

Devices from nickel mediated crystallization with vapor deposited nickel have also been made, and show large leakage currents. In recent work by Meng *et al.*, the crystalline silicon that grew out from the nickel deposited area still had a concentration of 10^{19} cm^{-3}. This concentration is much higher than the nickel content in our films, which were nucleated with limited use of nickel– the surface had only 0.19% nickel coverage. Therefore, our films potentially have good electrical characteristics, and electrical characterization should be done with electron beam induced current to determine diffusion length.

Besides limiting nickel use, the amount of nickel incorporated in the polycrystalline layer can be lowered by effective gettering techniques. One technique that enhances the growth rate and provides a gettering layer is phosphorus doping of the template. Only one concentration of phosphorus doping was investigated, so looking at higher phosphorus concentrations could optimize the process. Higher phosphorus concentrations should getter the nickel more efficiently, and could increase the crystallization rate even further.

The nickel particle distribution can also be improved. The Ni ink should be made by a method that prevents aggregates. This can be achieved by charging the particles, so that they electrostatically repel each other, though accomplishing this may not be trivial.

Further improvement to the template could be made with a high temperature heat treatment to repair the low angle boundaries within the crystals. A pulsed heat treatment could raise the temperature high enough in the silicon layer for large-scale atomic movement, without damage to the substrate.

6.2 Positron annihilation spectroscopy

Positron annihilation spectroscopy (PAS) was used to study vacancies in solid-phase crystallized silicon in four doping cases: undoped, B-doped, P-doped, and P&B-doped. O-V complexes were seen in all samples, P-V complexes in the P- and P&B-doped samples, and vacancy clusters in the end of range region. Progressive etching of a subset of the samples was achieved, and a defect concentration on order of 10^{15} cm^{-3} was estimated for all samples.

The samples made for the positron study were, unfortunately, too complex to be able to see reliable differences between the four doping cases. The interesting signals were obscured by oxygen-vacancy complexes and end-of-range (EOR) implant damage below the amorphous layer. The thin, surface amorphous layer was also easily contaminated with rate reducing impurities, like oxygen and hydrogen. A slow retardation was observed for all samples, with P-doped silicon the only doped sample to show any enhancement. Unfortunately, no conclusions can be made about the mechanism for dopant enhanced SPE.

If this experiment were to be done again, a number of recommendations should be followed:

1. The amorphous layer should be thick, which involves MeV amorphizing implantations. This would take care of two issues: the oxygen at the surface and the EOR damage deep in the layer. A region of the amorphous layer beyond the reach of oxygen, and far enough removed from the EOR would isolate any effects that affect solid-phase epitaxy.
2. The etch-back experiment should be done *in situ* with sputtering, and full energy scans should be taken of the data, rather than the three discrete energies taken in this experiment.

Appendix A Device Physics of Photovoltaics

For an idealized solar cell with no recombination or other losses, the current-voltage characteristics are given by [1],

$$I = I_S(e^{qV/kT} - 1) - I_L$$

where I_S = saturation current, I_L = illumination current, and q = electron charge, which is the I-V curve for a diode, with a current source, I_L (see Figure A.1). The positive current flows in a solar cell from the n-type layer to the p-type layer, which is in the negative direction by convention, so power is extracted when there is positive voltage and negative current, represented by the fourth quadrant in an I-V plot.

The goal of this device is maximum production of power, $P = VI$. The maximum power, $P_{\max} = I_{\max}V_{\max}$, can be graphically determined as the largest area rectangle to fit between the axes and the I-V curve, with the corner point at the curve intersecting $I_{\max}$ and $V_{\max}$. The upper limits of the voltage and current output are the open circuit voltage, V_{OC}, and the short circuit current, I_{SC}. The maximum power is related to V_{OC} and I_{SC} through the fill factor, FF, which is defined as $P_{\max}/V_{OC}I_{SC}$. In this idealized solar cell, I_{SC} is simply the illumination

current I_L. V_{OC} is proportional to the difference between the band gap energy E_g and the energy drop over the depletion region, as seen graphically in Figure A.2. The voltage difference over the depletion region, also known as the built-in potential V_{bi}, is given by [1],

$$V_{bi} = \frac{kT}{q} \ln\left(\frac{n_n p_p}{n_i^2}\right)$$

where n_n = the electron density on the n side,

p_p = the hole density on the p side,

n_i = the intrinsic carrier density.

For non-degenerately doped layers, $n_n \approx N_D$ and $p_p \approx N_A$, and

$$V_{bi} = \frac{kT}{q} \ln\left(\frac{N_D N_A}{n_i^2}\right).$$

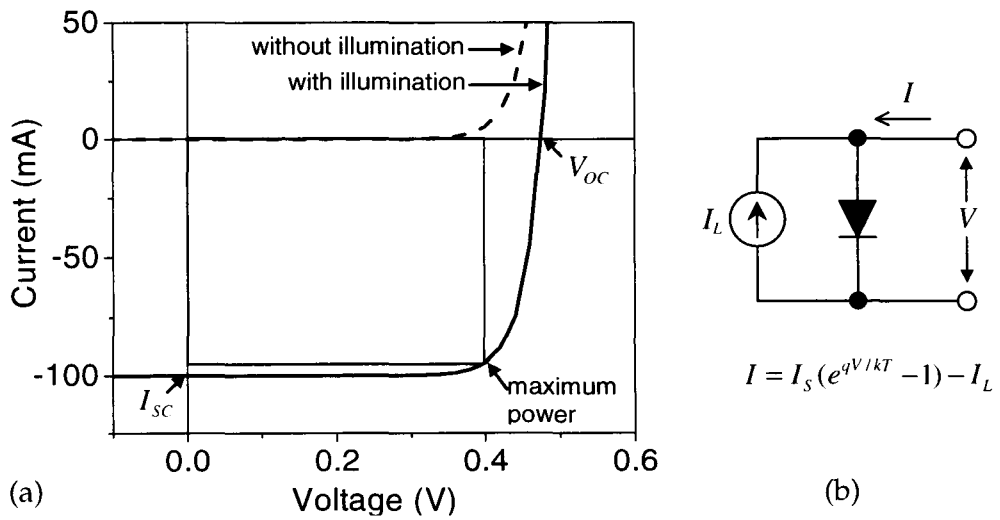

Figure A.1. (a) Current-voltage curve of an ideal solar cell without illumination and under illumination, setting I_S = 1 nA, and I_L = 100 mA. V_{OC} and I_{SC} are the x- and y-axis intercepts, respectively. (b) equivalent circuit of an ideal solar cell.

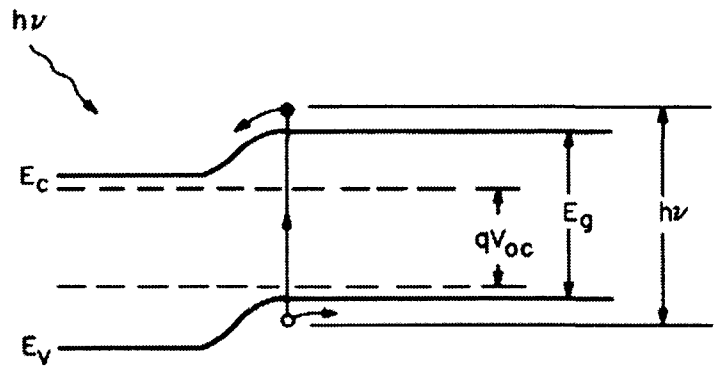

Figure A.2. Energy band diagram of p-n junction solar cell under illumination. qV_{OC} is shown as the energy difference between the impurity energy levels.

A practical solar cell will have losses that result in a reduction in I_{SC} and V_{OC}. Crystallographic defects like impurities and grain boundaries result in increased recombination, and therefore a decrease in the carrier population and current. Reductions in V_{OC} can result from leakage currents from recombination in the depletion region and material and contact resistances, which can be modeled in an equivalent circuit as a shunt resistance and series resistance, respectively. The I-V characteristics [1] are then

$$\ln\left(\frac{I+I_L}{I_S}-\frac{V-IR_s}{I_S R_{sh}}+1\right)=\frac{q}{kT}(V-IR_s)$$

where R_s = series resistance

R_{sh} = shunt resistance.

Appendix B Grain Boundary Filtration by Selective Nucleation and Solid Phase Epitaxy of Ge Through Planar Constrictions

Approaches to formation of large-grained polycrystalline semiconductor films on glass substrates have received ever increasing attention in recent years, driven by the demonstration of low temperature processed polycrystalline silicon thin film transistors for active matrix liquid crystal displays and monolithic integration of driver circuits onto such displays [56]. Further, large grain size is desirable in semiconductor films of Si, GaAs, CdTe, and $CuInSe_2$ for photovoltaic applications [57]. Many techniques have been proposed for fabrication of large grain semiconductor films at low temperature, such as plasma enhanced chemical vapor deposition (CVD) of Si [58], thermal CVD of SiGe [59], solid phase crystallization of Si [60] and Ge [61], and laser crystallization of Si [62,63]. Selective nucleation and solid phase epitaxy (SNSPE) [60,61] is a simple technique since it does not require special processing or equipment, but employs patterned selective nucleation to enable larger Si or Ge

grain sizes than that achievable by conventional unseeded solid phase crystallization.

The SNSPE process exploits the thermodynamic barrier to nucleation whose origin lies in the size dependence of the surface and volume contributions to the crystal free energy. The existence of a nucleation barrier results in a temporal delay in growth of small crystals to macroscopic size. At the onset of crystallization, there will be a finite incubation time during which no crystal nucleation occurs before the onset of steady-state nucleation. If there are heterogeneous selective nucleation sites present, these can lower the thermodynamic barrier to nucleation. In this case, a small, growing crystal will be enlarged by annealing during the incubation time, without competition from random nucleation. The achievable grain size can be estimated as the product of the incubation time and the lateral solid phase epitaxy rate during SNSPE. Ideally, the selective nucleation region would be a single crystal, but this is difficult to achieve in practice. Metal-induced nucleation yields a large number of nanometer-scale crystalline grains in each seed region, and since lateral epitaxy starts at the periphery of each selective nucleation site, in general multiple grains are produced from each nucleation site.

We have demonstrated a grain boundary filtration technique by using planar constrictions in patterned films during SNSPE of Ge. Large-grained polycrystalline Ge may be useful as a template for GaAs heteroepitaxy in optoelectronic and photovoltaic devices [64], and it also serves as a model for

similar techniques applied to Si films. A similar grain boundary filtration technique was demonstrated earlier in thin film solidification [65], and has also been applied to excimer laser crystallization of Si [66]. In the present work, patterns consisted of (i) a small Ge island seed region including a deposited metal selective nucleation site, (ii) a narrow seed selection region, and (iii) a single grain region consisting of a main rectangular island, as illustrated in Figure B.1.

In region (i), lateral SPE of Ge starts at the edge of the selective nucleation site and SPE continues in all directions with a variety of orientations. The growth of almost all grains is terminated at the pattern edge of region (i), but a few grains survive to grow into the seed selection region. Further grain selection occurs in the seed selection region (ii) and only one grain orientation reaches the single grain region (iii). Consequently, the main island has a single crystal seed and the region is crystallized laterally as shown in Figure B.1.

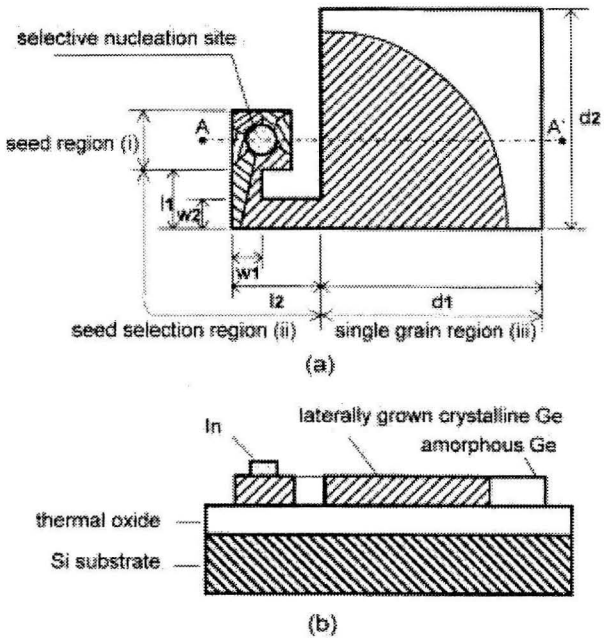

Figure B.1. In (a), plan view schematic of the pattern employed for grain boundary filtration. In (b), cross-sectional view of A–A.

100-nm-thick amorphous Ge films were deposited by ultrahigh vacuum electron beam evaporation onto cleaned, thermally grown 100 nm silicon dioxide films on Si (100) substrates. Phosphorus doping by ion implantation at 50 keV to a dose of 2×10^{15} cm^{-2} yielded a calculated peak phosphorus concentration [67] of 0.7 at. %. Then photolithography and wet chemical etching were used to define mesa islands in the amorphous Ge on SiO_2. The size of the mesa island was slightly smaller than the mask pattern size because of undercutting in the etch process. As shown in Figure B.2, the seed selection region (w1 = w2) is 1.5 μm wide and typically 10 μm long (l1 + l2), and the main island (d1 = d2) was 5–45 μm. A 20-nm-thick In film, used for the selective nucleation regions, was deposited by high vacuum evaporation onto Ge films covered with patterned

photoresist, and lift-off was used to define 2 μm diameter In islands. After these process steps, samples were isothermally annealed at 400 °C for various time intervals. Lateral crystal growth was investigated after each annealing interval by optical microscopy and transmissions electron microscopy (TEM). TEM specimens were prepared by backetch removal of the Si substrate after annealing.

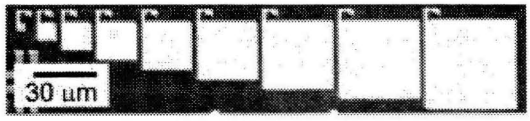

Figure B.2. Optical micrograph of mesa patterns defined in amorphous Ge for grain boundary filtration.

Figure B.3 is a series of plan view TEM images after 400 °C anneals of (1) 663, (b) 976, and (c) 1293 min. Also shown are electron diffraction patterns of (d) the selective nucleation site, (e) seed selection region, (f) seed area for single grain region, (g) center of the single grain region, (h) growth front, and (i) and (j) two corners. The location and area for the electron diffraction patterns are shown as dotted circles in Figure B.3(c). The incident angle of the electron beam used for the diffraction patterns was approximately perpendicular to the sample, but it was not precisely aligned, owing to bending of the thin film specimen after backetching. Figure B.3(a) reveals a large number of small grains in the selective nucleation site and a ring-like electron diffraction pattern corresponding to poly-Ge as shown in Figure B.3(d). Lateral grain growth in all directions with a variety of orientations started near the selective nucleation site and the number

of grains was reduced in the seed selection region as shown in Figure B.3(e), which has no ring pattern. In the seed selection region, the fastest-growing orientation is selected [8,68], and after the growth front passed through the seed selection region, it is able to expand into the single grain main island, as illustrated in Figure B.3(b). The area indicated by the diffraction pattern Figure B.3(f) acts as the seed for the single grain region, and indicates successful single grain seeding of the main island.

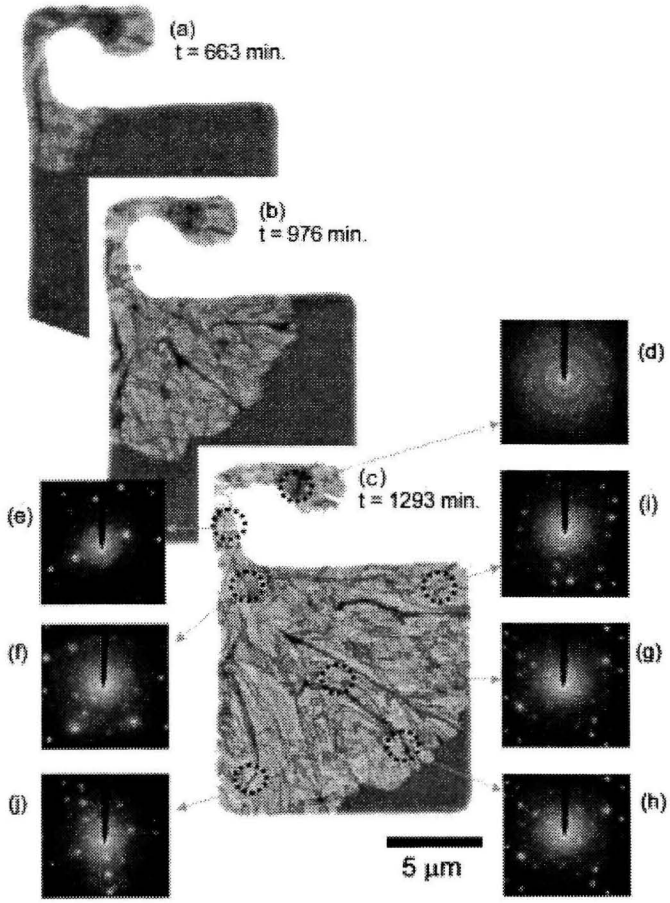

Figure B.3. Plan view transmission electron micrographs and selected area diffracted patterns for partially crystallized films after each 400 °C anneal.

During further annealing at times beyond the incubation time, lateral seeded growth must compete with spontaneous nucleation in the amorphous Ge film. The lateral SPE rate at 400 °C estimated from Figure B.3(a), (b), and (c) is 2.9×10^{-4} μm/s. As shown in Figure B.3(c), spontaneous nucleation was not observed and the main island was fully crystallized via laterally seeded growth. Electron diffraction patterns shown in Figure B.3(f), (g), (h), (i), and (j) also show the main island has polycrystalline components. Two preferred textures of <110> and <112> were observed, as seen in Figure B.4. These results demonstrate that locally controlled large (>100 μm^2) Ge single crystal films can be obtained via SNSPE through planar constrictions.

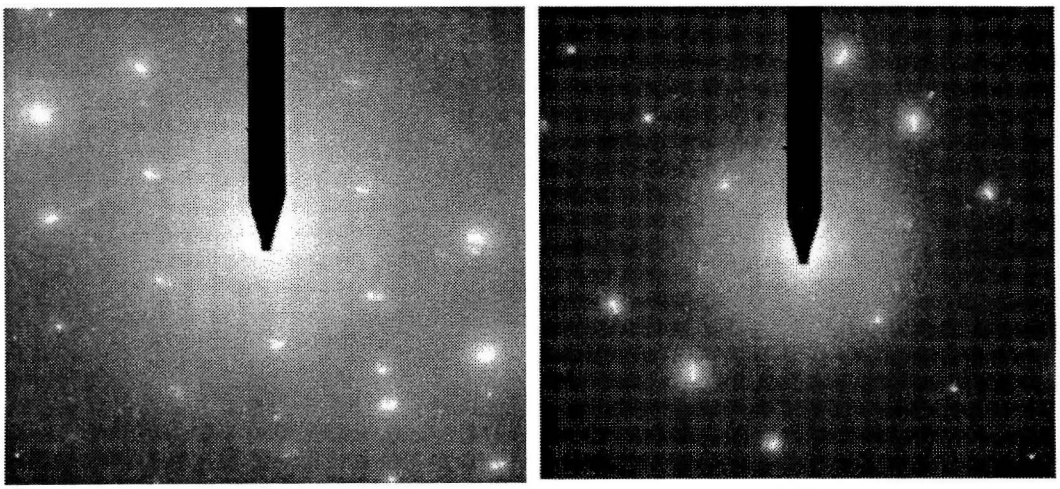

<110> <112>

Figure B.4. Diffraction patterns of the preferred textures, <110> and <112>.

For other patterns with different shapes and larger main islands than those illustrated in Figure B.3, we also observed spontaneous nucleation that nucleated in the bulk competing with SNSPE, as shown in Figure B.5; nucleation has also

been observed at the edge of the Ge patterns, but not preferentially. This suggests that the annealing time of 1293 min. is approximately equal to the incubation time at 400 °C for amorphous Ge films. We note that during these experiments, low anneal temperatures and long anneal times were chosen to optimize the maximum achievable grain size. Based on our previous research on SNSPE [61], we anticipate that the same grain boundary filtration results can be achieved at much shorter times (<60 min) for anneal temperatures in the range of 400–500 °C, although the maximum achievable grain sizes may be slightly smaller.

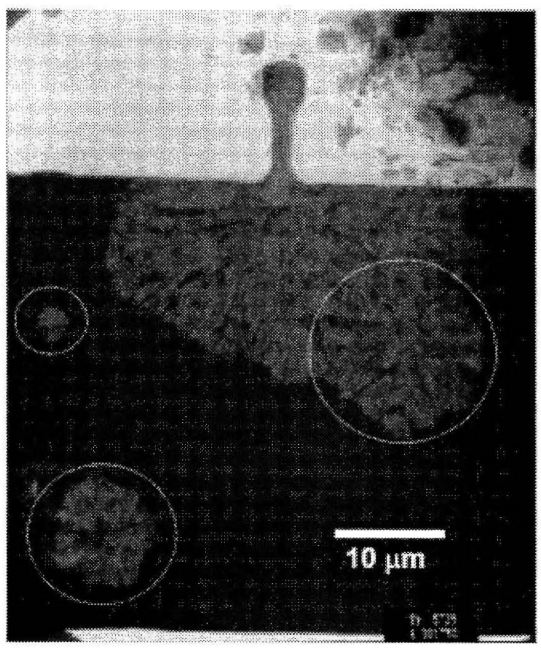

Figure B.5. Example of between spontaneous nucleation (circumscribed by dotted lines) with patterned selective nucleation in a larger Ge island following a 400 °C anneal for 1293 min.

Appendix C Tin-mediated Crystallization of Silicon

An a-Si on Sn layer structure was deposited by vapor deposition in ultrahigh vacuum on a 100 nm thick silicon oxide layer thermally grown on a <100> silicon substrate. Both a-Si and Sn layers were 50 nm thick each. The substrates were cleaned and then vacuum annealed with a pressure of 10^{-7} torr at 200 °C, 220 °C, or 500 °C, for an hour, and then imaged by TEM and atomic force microscopy (AFM).

The samples at all three annealing temperatures had similar morphology: monocrystalline Si particles and Sn particles interspersed in a Si-Sn alloy matrix as seen in Figure C.1. Though it is difficult to discern the individual grains and therefore the grain size in the plan view TEM images, the features appear to scale with annealing temperature, with ~50 nm particles for the 200 °C anneal, ~80 nm particles for the 220 °C anneal, and ~100 nm particles for the 500 °C anneal. Some Sn-rich globules segregated to the surface, which correlate to the large mounds, around 100 nm high, seen in the AFM image, in Figure C.2(a). The surface has an rms roughness of 4 nm. From the cross sectional image in Figure C.2(b), voids can be seen underneath some of the bumps. The Sn probably migrated to the surface, catalyzing the Si

crystallization, leaving voids in some areas. Composition was determined by energy dispersive x-ray analysis.

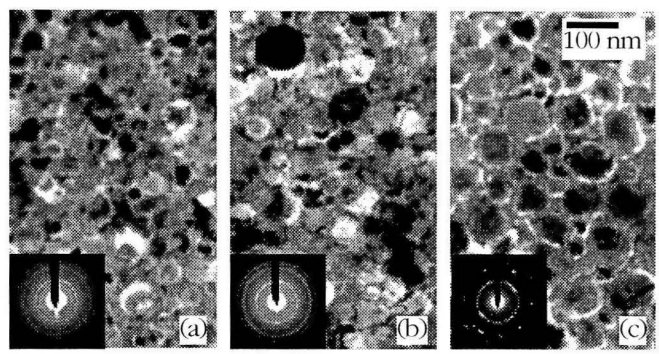

Figure C.1. Bright field, plan view TEM of Si-Sn samples annealed at (a) 200 °C with grain features ~50 nm, (b) 220 °C with grain features ~80 nm, and (c) 500 °C with grain features ~100 nm. Selected area diffraction patterns displaying polycrystalline diffraction rings are shown in the insets.

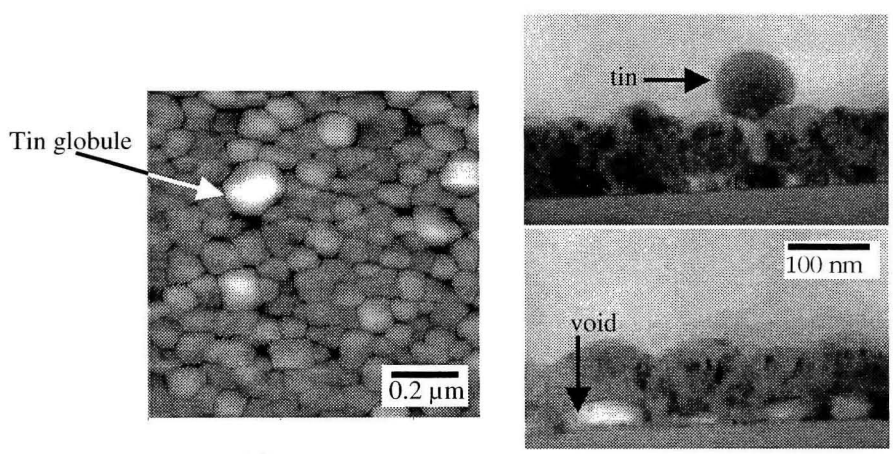

Figure C.2. (a) AFM image of a Si-on-Sn sample after an 1 hour anneal at 220 °C. The surface has an rms roughness of 4 nm. (b) Bright field, cross-sectional TEM images of a Si-on-Sn sample after an 1 hour anneal at 220 °C. Visible in this image are voids present under the crystallized layers, and tin that segregated to the surface.

Appendix D X-ray Fluorescence Microprobe

The x-ray fluorescence microprobe at the Advanced Light Source at Lawrence Berkeley National Laboratory uses radiation produced from 1.9 GeV electrons. The maximum beam current is approximately 400 mA at full power and drops exponentially over 6 hours to approximately 200 mA. The peak wavelengths are in the UV to soft x-rays (10 eV-1keV). The beamline (10.3.1) uses two thin film mirrors (Kirkpatrick-Baez pair) whose curvature can be manipulated to form a 1.0×1.2 μm spot size; the mirrors also filter the beam to allow reflection of 6-15 keV radiation. The flux is 3×10^{10} photons/s at 12.5 keV.

The sample is mounted on a stage with fine motor control which can raster across the sample with 0.01 μm precision. The incident beam impinges on the sample at 45°, and the axis of the detector is placed 45° from the sample, with the detector placed close to the sample to collect as large a solid angle as possible.

The soft x-rays excite core electrons, and the outer shell electrons that fall to that lower energy level produce characteristic emission lines. Each element has characteristic emission lines, and the most intense emission lines are from an electron from the n=2 shell down to n=1, which is the K_α line, and the transition from n=3 to n=1 shell, which is K_β. The number of transitions scales with the

square of atomic number, so more massive elements are easier to detect and have a stronger signal [69].

Appendix E Temperature Control During Sample Preparation for PAS experiments

The samples from Chapter 5 were annealed on a hot stage consisting of a carbon platen set approximately one mm above a carbon heater (see Figure E.1). The platen provided a plate to rest the samples while making the radiative heating from the heater more uniform. The temperature uniformity of the platen was probed with a pyrometer with spot size of 4 mm and outfitted with a filter to block light from the TRR diode laser. The temperature decreased by 0.5 °C when the center of the spot was 4 mm off center. Therefore, the sample size was limited to 5 mm square to ensure the most uniform heating possible. The temperature was regulated by the PID controller in the Accufiber Model 10 pyrometer (P = 0.1, I = 0.2, and D = 0.002), which controlled the voltage output of the Kepco ATE 25-20M power supply that powered the carbon heater. The samples were placed at the center of the platen, and the pyrometer was focused to the side of the sample about 7 mm from the center with a spot size of about 6 mm, so that the sample would not interfere with the input to the pyrometer. Temperature was calibrated using a thermocouple wafer. Final temperature was reached in 5

minutes, and was stable to a degree, as measured by the thermocouple wafer placed at the center of the platen. The anneals were stopped by turning off the power to the carbon heater and letting the sample cool with the heater. The heater cooled to 300 °C in approximately 7 min.

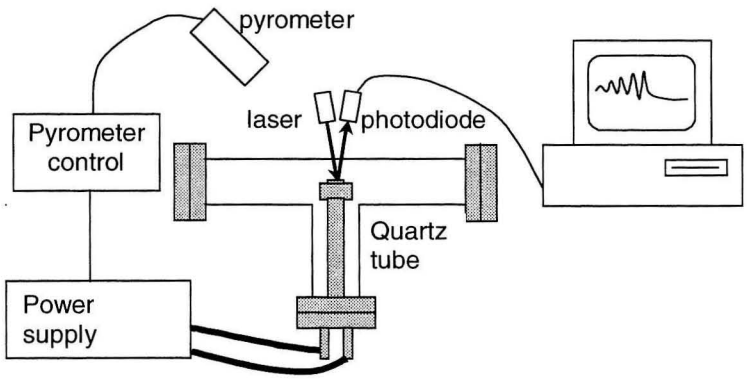

Figure E.1. Schematic of vacuum hot plate used to anneal samples, the time resolved reflectivity setup, temperature control setup, and data acquisition of the reflectivity to a computer.

Appendix F Positron Diffusion a Solid

Once the positrons have slowed down to thermal energies, they can still migrate large distances through diffusion. The diffusion process can be described by a steady state continuity equation,

$$\frac{dn}{dt} = 0 = -\frac{1}{q}\Delta \cdot J + G - U$$

where: n is the positron density,

positron current density $J = q\mu En - qD\nabla n$, with q = positron charge, μ = positron mobility, E = electric field strength, and D = positron diffusion coefficient,

generation rate $G = I(z)$ = the positron stopping rate, and

recombination rate $U = k_d C_d + C_b / \tau_b$, the annihilation rate from defects, where k_d is the defect trapping rate and C_d is defect concentration, and from the bulk, where τ_b is the bulk lifetime and C_b is the density of the bulk material.

Assuming uniformity in the x- and y- directions, the equation becomes,

$$D\frac{d^2 n}{dz^2} - \frac{d}{dz}\left(\mu E(z) n\right) + I(z) - (k_d C_d + C_b / \tau_b) n = 0,$$

which simplifies further with the introduction of an effective trapping rate $\tau_{eff}^{-1} = k_d C_d + C_b / \tau_b$ and effective positron diffusion length $L_{eff} = (D\tau_{eff})^{1/2}$, to

$$\frac{d^2n}{dz^2} - \frac{d}{dz}\left(\frac{\mu E(z)n}{D}\right) + \frac{I(z)}{D} - \frac{n}{L_{eff}^2} = 0.$$

The effective diffusion length can be extracted by fitting this equation to data using the program VEPFIT. By taking the ratio of the "defect-free" bulk diffusion length, L_b, to the effective diffusion length and solving for the defect concentration,

$$C_d = \frac{C_b}{k_d \tau_b}\left(\left(\frac{L_b}{L_{eff}}\right)^2 - 1\right),$$

the defect concentration can be calculated from the effective diffusion length extracted from the data, if the trapping rate of the defect is known. For "defect-free" bulk silicon, the bulk lifetime τ_b = 220 ps, diffusion length L_b ~ 200 nm, and atomic density C_b = 5×10^{22} cm^{-3}. The concentration of divacancies in Si, which have a trapping rate k_d = 2×10^{15} s^{-1}, is plotted in Figure F.1 as a function of positron diffusion length. A divacancy concentration of 10^{20} cm^{-3} can result in a reduction of the diffusion length to ~10 of nm.

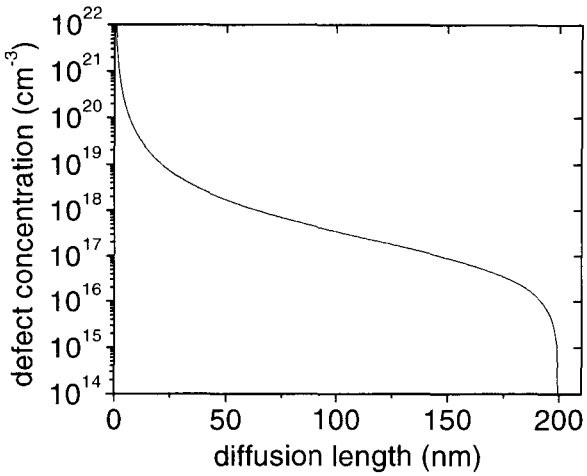

Figure F.1. Divacancy concentration as a function of positron diffusion length.

The positron stopping rate depends on the energy of the incident beam (see Figure F.2). Monte Carlo profiles have been calculated and confirm the implantation profiles used in these experiments. For a homogeneous, semi-infinite target, the profile can be expressed by a Makhovian distribution

$$P(E,z)=\frac{mz^{m-1}}{z_0^m}e^{-(z/z_0)^m}, \text{ where } z_0=\frac{\langle z\rangle}{\Gamma\left(1+\frac{1}{m}\right)},$$

and the mean implantation depth $\langle z\rangle=\frac{A}{\rho}E^n$. The parameters m, n, and A are empirically determined, though for most materials, their values are 2.0, 1.6, and 40, respectively, with depth in units of nm. These values were used for the case of silicon.

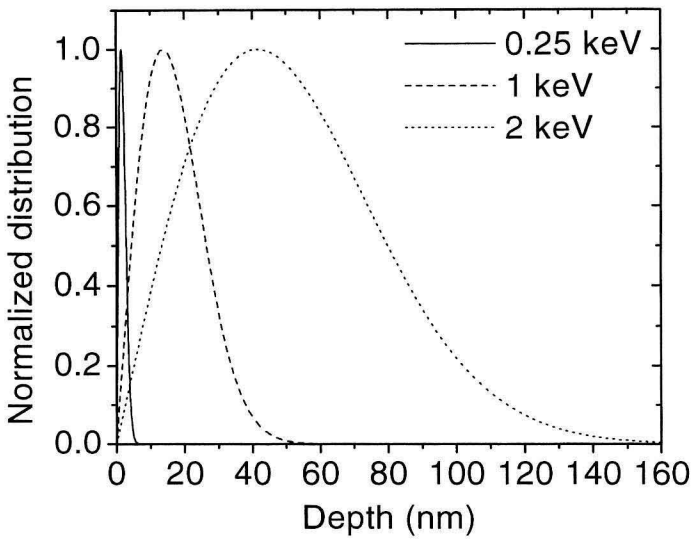

Figure F.2. Positron distribution into Si (ρ=2.33) as a function of beam energy.

Appendix G VEPFIT Analysis of Doppler Broadening Data

	Depth (nm)	S_a	L_a (nm)	C_d (cm^{-3})	S_{epi}	L_{epi} (nm)	C_d (cm^{-3})
Undoped	0				1.006-1.008	107-86	3.0×10^{17}-5.3×10^{17}
	35	1.03	17	1.6×10^{19}	1.006-1.0072	73-66	7.7×10^{17}-9.7×10^{17}
	69	1.033	12	3.3×10^{19}	1.0038-1.0084	99-80	3.7×10^{17}-6.3×10^{17}
	138	1.033	12	3.3×10^{19}	0.9874-1.009	88-34	5.0×10^{17}-4.0×10^{18}
	207	1.033	8	7.4×10^{19}	0.9978-1.006	51-38	1.7×10^{18}-3.2×10^{18}
B-doped	0				1.006-1.012	168-64	5.4×10^{16}-1.0×10^{18}
	35	1.035	23	8.8×10^{18}	1.006-1.012	168-64	5.4×10^{16}-1.0×10^{18}
	69	1.033	15	2.1×10^{19}	1.000-1.006	85-61	5.4×10^{17}-1.2×10^{18}
	138	1.0374	8	7.4×10^{19}	1.000-1.006	103-88	3.3×10^{17}-5.0×10^{17}
	207	1.035	15	2.1×10^{19}	1.000-1.006	64-53	1.0×10^{18}-1.6×10^{18}
P-doped	0				0.965 1.000	93 177	4.3×10^{17} 3.7×10^{16}
	35	1.033	17	1.6×10^{19}	1.000-1.014	142-67	1.2×10^{17}-9.4×10^{17}
	69	1.033	12	3.3×10^{19}	1.000-1.014	177-115	3.7×10^{16}-2.4×10^{17}
	207	1.033	12	3.3×10^{19}	1.000-1.014	177-115	3.7×10^{16}-2.4×10^{17}
P&B-doped	0				1.0052	71	8.2×10^{17}-8.2×10^{17}
	35	1.034	100	3.6×10^{17}	1.000-1.008	109-77	2.8×10^{17}-6.8×10^{17}
	69	1.034	100	3.6×10^{17}	1.0052	71	8.2×10^{17}-8.2×10^{17}
	207	1.0352	10	4.7×10^{19}	0.497-0.5012	44-29	2.3×10^{18}-5.5×10^{18}

Appendix H Positron Annihilation Spectroscopy Data of Etched Samples

Below are the depth profiles of S for etched samples described in Section 5.5.2, probed at 1 keV and compared to the Doppler broadening data.

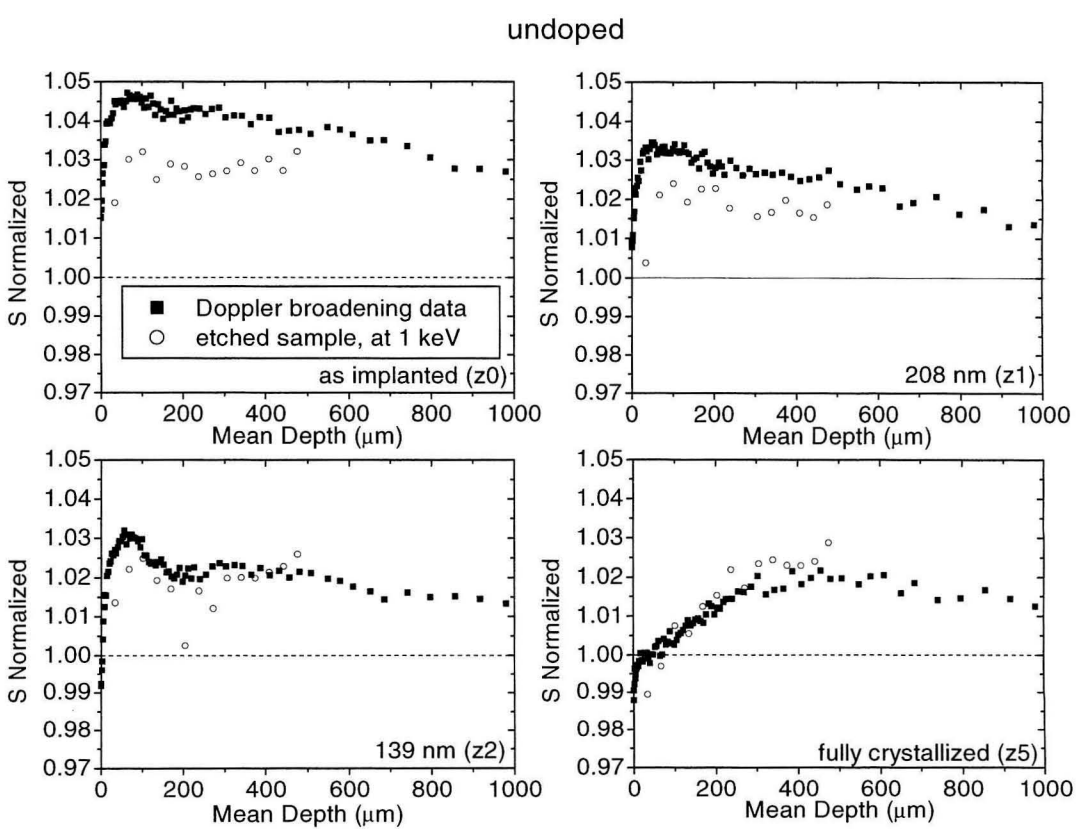

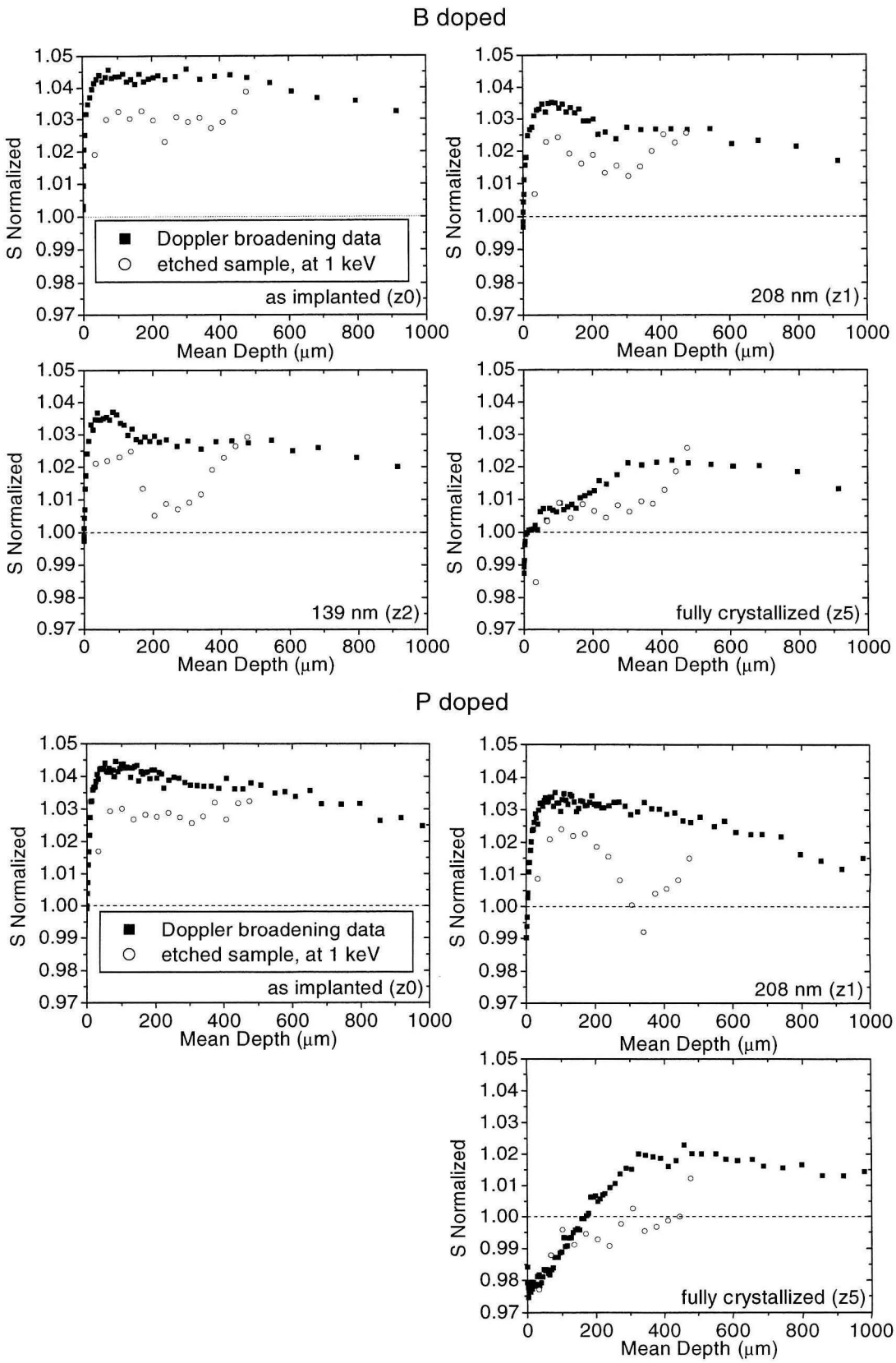
B doped
S Normalized
Mean Depth (μm)
Doppler broadening data
etched sample, at 1 keV
as implanted (z0)
208 nm (z1)
139 nm (z2)
fully crystallized (z5)
P doped
S Normalized
Mean Depth (μm)
Doppler broadening data
etched sample, at 1 keV
as implanted (z0)
208 nm (z1)
fully crystallized (z5)

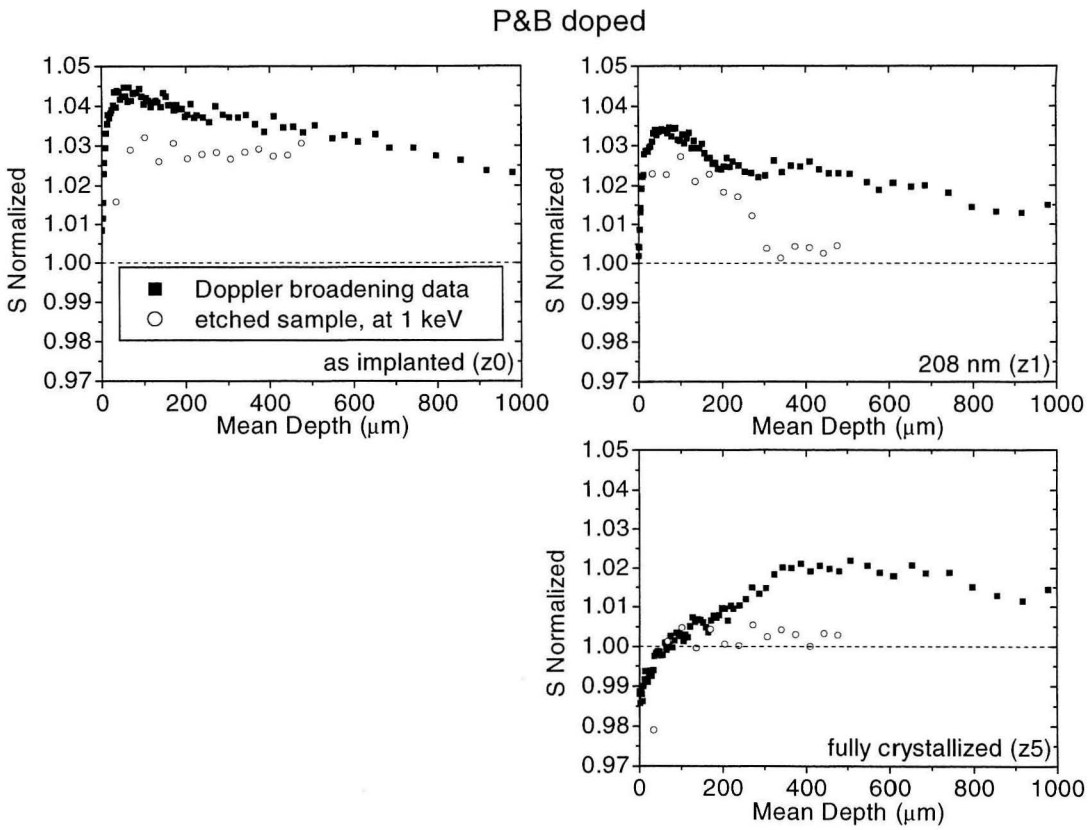
P&B doped
S Normalized
Mean Depth (μm)
Doppler broadening data
etched sample, at 1 keV
as implanted (z0)
208 nm (z1)
fully crystallized (z5)

Appendix I Further Analysis with Positron Annihilation Spectroscopy

I.1 High temperature anneals

Fully recrystallized undoped, B-doped, P-doped, and P&B-doped samples (described in Chapter 5) were annealed further at higher temperatures to investigate defect evolution in the end-of-range (EOR) damaged region. Samples were annealed in a vacuum furnace with a pressure of approximately 7×10^{-7} torr at 800 °C, 900 °C, and 1100 °C for 30 min, after full crystallization of the amorphous layer at 600 °C.

These high temperature anneals should redistribute impurities and remove implantation damage, revealing any remaining stable defects. For all samples, each incremental increase in temperature resulted in a thinner defect layer with a more negative S signal, which could be either oxygen or vacancies progressively segregating to the surface (see Figure I.1(a)). The S in the EOR region was equal to the bulk value, which suggested that the vacancy clusters dissolved.

At each temperature, the differences between the samples in the epitaxial region became obvious (see Figure I.1(b)). After the 800 °C anneal, the undoped and B-doped curves lie on each other, both having a surface dip at an S of 0.976,

attributed to oxygen. The surface value of S of P-doped sample dipped lower to a value of 0.965, which is probably from an additional contribution at P-V complexes. After the 900 °C anneal, the undoped and P-doped curves coincide, with a S value of 0.968 at the surface. This suggested that the P-V complexes dissolved, and the oxygen and/or vacancies migrated to the surface, resulting in a shallower layer with a larger population of oxygen-vacancy complexes. The surface value of S in the B-doped sample was 0.976 at 900 °C, which is the same surface value as in the 800 °C anneal. The boron possibly formed a complex with the oxygen, reducing the mobility of the oxygen, or changing the nature of the impurity-vacancy complex. After the 1100 °C anneal, all samples have a low S value at the surface (0.961 for undoped and B-doped, 0.957 for P-doped). This suggests the dissolution of all complexes and the segregation of oxygen and/or vacancies to the surface in a shallow layer.

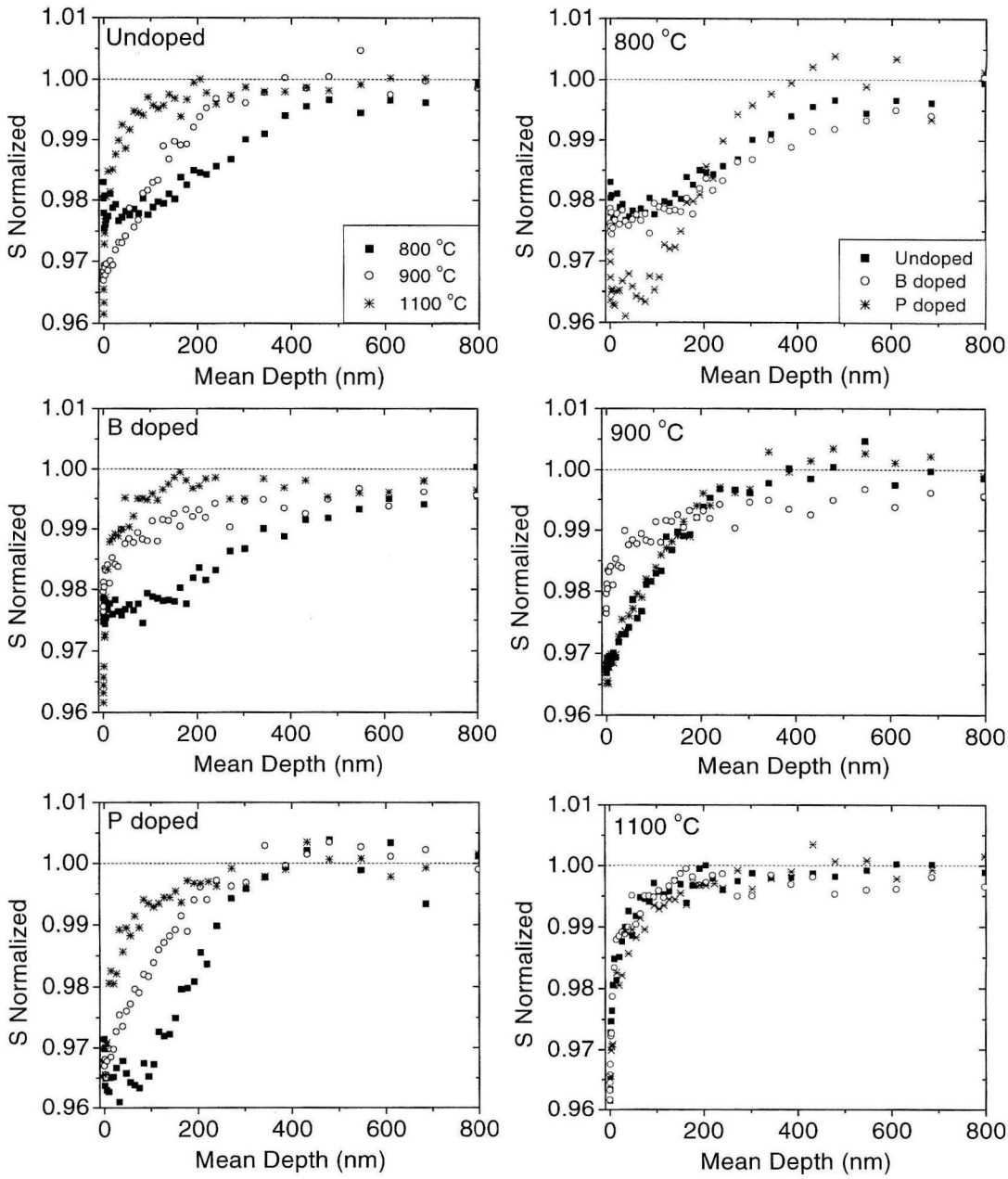

Figure I.1. (a) Doppler broadening data for high temperature anneals of undoped, B-doped, and P-doped silicon at 800 °C (■), 900 °C (○), and 1100 °C (✳). (b) Comparison of the undoped (■), B-doped (○), and P-doped (✳) silicon data at each anneal temperature.

I.2 Effect of 450 °C preanneal

The samples discussed in Chapter 5 had dislocations that originated from the rough as-implanted a-c interface. Dislocations are one dimensional open volume defects that can trap positrons and provide a low energy channel for diffusion, which could complicate the interpretation of the data. A 450 °C preanneal would have smoothed the as-implanted a-c interface and prevented dislocations. An undoped sample fully crystallized at 600 °C with a preanneal was compared to a 600 °C anneal without the preanneal (see Figure I.2(a)). The sample with preanneal does show less of a dip at the surface, but in the S-W plot (see Figure I.2(b)), the two samples basically fall on the same line, suggesting a negligible effect when estimating defect concentrations to an order of magnitude.

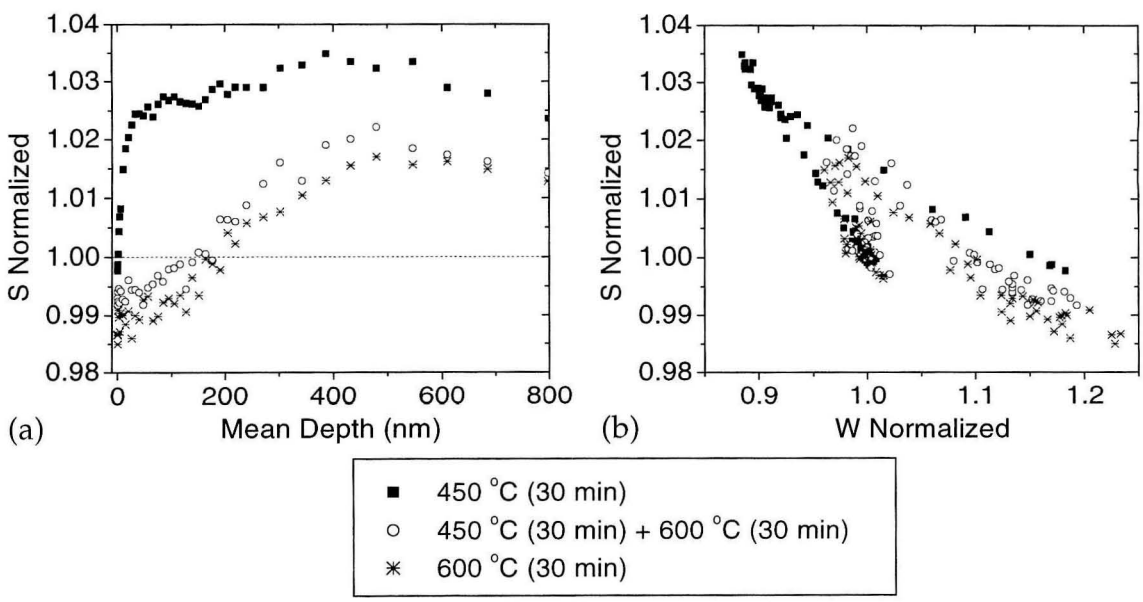

Figure I.2. (a) Doppler broadening data and (b) S-W plot for samples with a 450 °C anneal (■), a preanneal and recrystallization at 600 °C (○), and recrystallization without a preanneal (✳).

Bibliography

1. S. M. Sze, *Physics of Semiconductor Devices* (John Wiley & Sons, New York, 1981).
2. D. L. Staebler and C. R. Wronski, Appl. Phys. Lett. **31,** 292-294 (1977).
3. M. A. Green, K. Emery, K. Bucher, D. L. King, and S. Igari, Prog. Photovol. **7,** 321-326 (1999).
4. J. Zhao, A. Wang, P. Altermatt, and M. A. Green, Appl. Phys. Lett. **66,** 3636-3638 (1995).
5. R. Brendel, R. Bergmann, P. Lolgen, M. Wolf, and J. Werner, Appl. Phys. Lett. **70,** 390-392 (1997).
6. A. B. Sproul, Z. Shi, J. Zhao, A. Wang, Y. H. Tang, F. Yun, T. Young, Y. Huant, S. Edmiston, S. R. Wenham, and M. A. Green, in *Chracterization and Analysis of Multilayer Solar Cells*, 1994.
7. T. Matsuyama, N. Terada, T. Baba, T. Sawada, S. Tsuge, K. Wakisaka, and S. Tsuda, J. Non-Cryst. Solids **200,** 940-944 (1996).
8. G. Olson and J. Roth, Handbook of Crystal Growth **3,** 257-312 (1994).
9. J. A. Roth, G. L. Olson, D. C. Jacobson, and J. M. Poate, Appl. Phys. Lett. **57,** 1340-1342 (1990).
10. G. Olson and J. Roth, Materials Science Reports **3,** 1-78 (1988).

11. L. Csepregi, E. F. Kennedy, J. W. Mayer, and T. W. Sigmon, J. Appl. Phys. **49,** 3906-3911 (1978).

12. J. McCallum, Nuc. Instrum. Methods Phys. Res. B **148,** 350-354 (1999).

13. I. Suni, G. Goltz, M. G. Grimaldi, M. A. Nicolet, and S. S. Lau, Appl. Phys. Lett. **40,** 269-271 (1982).

14. J. S. Williams and R. G. Elliman, Phys. Rev. Lett. **51,** 1069-1072 (1983).

15. G. Lu, E. Nygren, and M. Aziz, J. Appl. Phys. **70,** 5323 (1991).

16. I. Suni, G. Goltz, M. A. Nicolet, and S. S. Lau, Thin Solid Films **93,** 171-178 (1982).

17. D. A. Porter and K. E. Easterling, *Phase transformations in metals and alloys* (Van Nostrand Reinhold (UK), Wokingham, Berkshire, 1981).

18. R. Iverson and R. Reif, J. Appl. Phys. **62,** 1675-1681 (1987).

19. T. J. Konno and R. Sinclair, Mater. Sci. Eng. A **179,** 426-432 (1994).

20. E. Nygren, A. P. Pogany, K. T. Short, J. S. Williams, R. G. Elliman, and J. M. Poate, Appl. Phys. Lett. **52,** 439-441 (1988).

21. Z. H. Jin, G. A. Bhat, M. Yeung, H. S. Kwok, and M. Wong, J. Appl. Phys. **84,** 194-200 (1998).

22. C. Hayzelden and J. L. Batstone, J. Appl. Phys. **73,** 8279-8289 (1993).

23. S. Lee, Y. Jeon, and S. Joo, Appl. Phys. Lett. **66,** 1671-1673 (1995).

24. C. Hayzelden, J. Batstone, and R. Cammarata, Appl. Phys. Lett. **60,** 225-227 (1992).

25. G. Radnoczi, A. Robertsson, H. Hentzell, S. Gong, and M. Hasan, J. Appl. Phys. **69,** 6394-6399 (1991).

26. S. K. Ghandhi, *VLSI Fabrication Principles* (Wiley, New York, 1983).

27. J. M. Poate, S. Coffa, D. C. Jacobson, A. Polman, J. A. Roth, G. L. Olson, S. Roorda, W. Sinke, J. S. Custer, M. O. Thompson, F. Spaepen, and E. Donovan, Nuc. Instrum. Methods Phys. Res. B **55,** 533-543 (1991).

28. R. D. Thompson and K. N. Tu, Appl. Phys. Lett. **41,** 440-442 (1982).

29. S. M. Joshi, U. M. Gosele, and T. Y. Tan, J. Appl. Phys. **77,** 3858-3863 (1995).

30. S. McHugo, H. Hieslmair, and E. Weber, ICDS-18 - Proceedings of the 18th International Conference on Defects in Semiconductors, Pts 1-4 **196-,** 1979-1983 (1995).

31. E. O. Sveinbjornsson, O. Engstrom, and U. Sodervall, J. Appl. Phys. **73,** 7311-7321 (1993).

32. W. Schroter and R. Kuhnapfel, Appl. Phys. Lett. **56,** 2207-2209 (1990).

33. R. C. Cammarata, C. V. Thompson, C. Hayzelden, and K. N. Tu, J. Mater. Res. **5,** 2133-2138 (1990).

34. K. N. Tu and J. W. Mayer, in *Thin Films - Interdiffusion and Reactions*, edited by J. M. Poate, K. N. Tu, and J. W. Mayer (Wiley, New York, 1978), p. 359.

35. *VLSI Technology; Vol.* , edited by S. M. Sze (McGraw-Hill, New York, 1988).

36. E. R. Weber, Appl. Phys. A **30,** 1-22 (1983).

37. S. Coffa, J. M. Poate, D. C. Jacobson, W. Frank, and W. Gustin, Phys. Rev. B **45,** 8355-8358 (1992).

38. C. Szeles and K. Lynn, in *Encyclopedia of Applied Physics; Vol. 14* (VCH Publishers, 1996), p. 607-632.

39. M. Petkov, C. Chen, H. Atwater, S. Rassiga, and K. Lynn, Appl. Phys. Lett. **76,** 1410-1412 (2000).

40. K. G. Lynn, J. R. MacDonald, R. A. Boie, L. C. Feldman, J. D. Gabbe, M. F. Robbins, E. Bonderup, and J. Golovchenko, Phys. Rev. Lett. **38,** 241-244 (1977).

41. J. R. MacDonald, K. G. Lynn, R. A. Boie, and M. F. Robbins, Nuc. Instrum. Methods **153,** 189-194 (1978).

42. P. Asoka-Kumar, M. Alatalo, V. J. Ghosh, A. C. Kruseman, B. Nielsen, and K. G. Lynn, Phys. Rev. Lett. **77,** 2097-2100 (1996).

43. V. Ghosh, M. Alatalo, P. Asoka-Kumar, K. Lynn, and A. Kruseman, Appl. Surf. Sci. **116,** 278 (1997).

44. M. Alatalo, P. Asoka-Kumar, V. Ghosh, B. Nielsen, K. Lynn, A. Kruseman, A. Van Veen, and M. Puska, J. Phys. Chem. Solids **59,** 55 (1998).

45. A. van Veen, H. Schut, J. de Vries, R. A. Hakvoort, and M. R. Ijpma, in *Analysis of positron profiling data by means of "VEPFIT"*, New York, 1990 (American Institute of Physics), p. 171.

46. B. Nielsen, O. W. Holland, T. C. Leung, and K. G. Lynn, J. Appl. Phys. **74,** 1636-1639 (1993).

47. H. Kauppinen, C. Corbel, K. Skog, K. Saarinen, T. Laine, P. Hautojarvi, P. Desgardin, and E. Ntsoenzok, Phys. Rev. B **55,** 9598-9608 (1997).

48. A. van Veen, R. A. Hakvoort, H. Schut, and P. E. Mijnarends, J. Phys. IV (Paris) **5,** 37-47 (1995).

49. R. Krause-Rehberg and F. Börner, in *Workshop on Positron Studies of Semiconductor Defects* (1999).

50. F. Börner, S. Eichler, A. Polity, R. Krause-Rehberg, R. Hammer, and M. Jurisch, J. Appl. Phys. **84,** 2255-2262 (1998).

51. S. Roorda, W. C. Sinke, J. M. Poate, D. C. Jacobson, S. Dierker, B. S. Dennis, D. J. Eaglesham, F. Spaepen, and P. Fuoss, Phys. Rev. B **44,** 3702-3725 (1991).

52. C. N. Waddell, W. G. Spitzer, J. E. Fredrickson, G. K. Hubler, and T. A. Kennedy, J. Appl. Phys. **55,** 4361-4366 (1984).

53. S. Adachi and K. Utani, Jpn. J. Appl. Phys. 2 **32,** L1189-L1191 (1993).

54. T. Suzuki and S. Adachi, Jpn. J. Appl. Phys. 1 **33,** 2689-2691 (1994).

55. M. P. Petkov, M. H. Weber, K. G. Lynn, R. S. Crandall, and V. J. Ghosh, Phys. Rev. Lett. **82,** 3819-3822 (1999).

56. Y. Morimoto, K. Hirano, H. Abe, T. Kuwahara, I. Hasegawa, S. Yuda, N. Sotani, and K. Yoneda, Tech. Dig. Int. Electron Devices Meet., 837 (1995).

57. A. L. Fahrenbuch and R. H. Bube, *Fundamentals of Solar Cells* (Academic, New York, 1983).

58. H. Tanabe, M. Azuma, T. Uematsu, H. Shirai, J. Hanna, and I. Shimizu, Mater. Res. Soc. Symp. Proc. **149,** 17 (1989).

59. K. Shiota, D. Inoue, K. Minami, M. Yamamoto, and J. Hanna, Jpn. J. Appl. Phys., Part 2 **36,** L989 (1997).

60. C. M. Chen and H. A. Atwater, Mater. Res. Soc. Symp. Proc. **485,** 67 (1998).

61. C. Yang and H. Atwater, Appl. Phys. Lett. **68,** 3392-3394 (1996).

62. K. Sera, F. Okumura, H. Uchida, S. Itoh, S. Kaneko, and K. Hotta, IEEE Trans. Electron Devices **ED-36,** 2868 (1989).

63. H. Kuriyama, T. Kuwahara, S. Ishida, T. Nohda, K. Sano, H. Iwata, S. Noguchi, S. Kiyama, S. Tsuda, S. Nakano, M. Osumi, and Y. Kuwano, Jpn. J. Appl. Phys., Part 1 **31,** 4550 (1992).

64. H. A. Atwater, C. M. Yang, and C. M. Chen, in *Future Generation Photovoltaic Technologies: 1st NREL Conference*, edited by R. D. McConnell (AIP, New York, 1997), p. 345.

65. H. A. Atwater, H. I. Smith, and M. W. Geis, Appl. Phys. Lett. **41,** 747 (1982).

66. H. J. Song and J. S. Im, Appl. Phys. Lett. **68,** 3165 (1996).

67. J. F. Ziegler, J. P. Biersack, and U. Littmark, *The Stopping and Range of Ions in Matter* (Pergamon, New York, 1985).

68. J. C. Bourgoin and R. Asomoza, J. Cryst. Growth **69,** 489 (1984).

69. K. Krane, *Modern Physics* (John Wiley & Sons, 1996).